SPATIAL AND TEMPORAL CONTROL OF LIGHT IN ATOMIC VAPOR

Thesis submitted for the degree of

"Doctor of Philosophy"

By

David Shwa

Submitted to the Senate of the Hebrew University of Jerusalem

February 2014

This work was carried out under the supervision of:

Prof. Nadav Katz

Acknowledgments

First and foremost, I would like to thank my advisor Prof. Nadav Katz for his great support in every aspect of my PhD. Nadav's contagious enthusiasm for research and his vast knowledge are all a student can hope for in an advisor. I thank him for letting me break into his office on a daily basis to discuss everything from experimental issues to theoretical and numerical problems and even the most personal affairs. To work in a new lab is not an easy task with many difficulties and mistakes along the way, but due to Nadav's optimistic vision and will to teach and share his wisdom, things always turned out for the best. For that I am grateful.

I wish to thank Avshalom and the machine shop for all the mechanical parts they manufactured and for the many improvements they made to my designs. I also wish to pay many debts to Gaby for helping me with many electronics problems and giving me all the parts I needed.

I would like to thank Dr. Guy Ron for so gladly letting me guide students in his lab and for all the equipment he lent me. I also wish to pay gratitude to Dr. Alex Retzker for his help in many theoretical problems.

I would like to thank all my current and former lab colleagues: Felix,Yoni, Ya'ara, Avraham, Ofer, Raffi, Roy, Anayesu, Elisha, Vitaly, Yevgeny, Tmiron, Naftaly, Simcha and Boaz. Specifically, I wish to thank Yoni. Since most of the time it was only both of us in the lab, I want to thank him for the endless talks, for his professional help in any need and mostly for all the fun we had together. I also wish to thank Raffi for helping me building the optical setup, giving me smart advises and relentlessly listen to me talking.

I especially wish to thank my friends Yoni, Eli, the two Assafs and Elad for helping me with my work and encourage me along the way. I also wish to thank Nadav, Prof. Hagai Eisenberg and all the people who participated and helped to establish and maintain HUJI OSA student chapter.

I'd like to thank my parents and sister for their support and encouragement during my studies.

Finally, I wish to thank my wife Ofra, for her support, encouragement, and understanding - I couldn't have done it without you.

I dedicate this thesis to my wife and beautiful two daughters Daniela and Adva.

List of publications

- "Lifetime and coherence of two-level defects in a Josephson junction", Yoni Shalibo, Ya'ara Rofe, **David Shwa**, Felix Zeides, Matthew Neeley, John M Martinis and Nadav Katz, Phys. Rev. Lett. 105, 177001 (2010)

- "Controllable motion of optical vortex arrays using electromagnetically induced transparency", **David Shwa**, Evgeny Shtranvasser, Yoni Shalibo and Nadav Katz, Opt. Express 20, 24842 (2012)

- "Shaping Laguerre–Gaussian laser modes with binary gratings using a digital micromirror device", Vitaly Lerner, **David Shwa**, Yehonathan Drori, and Nadav Katz, Opt. Lett. 37, 4826-4828 (2012)

- "Rapidly reconfigurable optically induced photonic crystals in hot rubidium vapor", Bethany Little, David Starling, John Howell, Raphael Cohen, **David Shwa** and Nadav Katz, Phys. Rev. A 87, 043815 (2013)

- "Heralded generation of Bell states using atomic ensembles", **David Shwa**, Raphael Cohen, Alex Retzker and Nadav Katz, Phys. Rev. A 88, 063844 (2013)

- "Direct Wigner Tomography of a Superconducting Anharmonic Oscillator", Yoni Shalibo, Roy Resh, Ofer Fogel, **David Shwa**, Radoslaw Bialczak, John M. Martinis, and Nadav Katz, Phys. Rev. Lett. 110, 100404 (2013)

- "Transient coherence of an EIT media under strong phase modulation", **David Shwa** and Nadav Katz, accepted to Phys. Rev. A (2014)

Abstract

The interaction of light with atomic media is an established field of research dating back to early spectroscopic studies that contributed immensely to the development of quantum mechanics. In recent years technological advances such as narrow band lasers and trapped atoms and the emergence of quantum technology raised new interest in this field and led to a vast range of new physical phenomena and applications. One interesting field of research is the coherent interaction of laser fields with a three level atomic media that leads to effects like coherent population trapping (CPT) and electromagnetically induced transparency (EIT). EIT occurs when, due to a strong pump field, a destructive interference between two quantum channels renders the medium transparent to a resonant weak probe. This effect is extremely narrow spectrally, leading to many useful applications such as sensitive magnetometry, light modulation, extremely slow light and quantum storage devices.

This thesis presents new ways to harness hot atomic vapor in order to spatially control light, enhance magnetic sensing and create two photon quantum entanglement. We also use atomic media in order to control and modulate complicated spatial patterns. Specifically we demonstrate the control of the collective motion of an optical vortex array using an EIT media. Scanning the frequency detuning between the pump and probe fields changes the susceptibility of the media, producing a unique effective diffraction of the vortex array for each detuning. A different way we introduce to spatially manipulate light is using the AC Stark shift in order to create all optical photonic crystals. We create an optical grating of a detuned pump beam inside hot rubidium vapor and measure the deflection of the probe beam from it. The modulation frequency of this AC Stark grating is directly related to the detuning implying high frequency modulation is possible with these systems. We demonstrate a new method of probing the coherence of atomic media in general and EIT media specifically by analyzing the transients of a probe beam as a function of detuning while applying the susceptibility with

strong phase modulation. When a magnetic field is applied the transients show multi-Zeeman level interference that enables wideband magnetic sensing with an improved sensitivity over standard EIT schemes. Finally, we propose a scheme that utilizes the collective enhancement of a photonic mode inside an atomic ensemble together with a proper Zeeman manifold to achieve a heralded polarization entangled Bell state. The entanglement is between two photons that are separated in time and can be used as a postselected deterministic source for applications such as quantum repeaters where a subsequent entanglement swapping measurement is employed.

Contents

List of Figures

Chapter 1

Introduction

The interaction of light with atomic media is one of the most prolific research areas in physics with numerous applications. It ranges from hydrogen spectroscopy which led to the emergence of quantum theory, through the invention of the laser and current research of many body systems such as Bose-Einstein condensation in atomic traps. Even the simplest example of light interacting with two or three level atoms holds a diversity of physical phenomena such as linear susceptibility effects, light induced three levels effects, e.g. coherent population trapping (CPT) and electromagnetically induced transparency (EIT), non-linear effects and purely quantum effects.

Resonative interaction between light and atoms offers a unique spectral control over the macroscopic attributes of the medium such as absorption and index of refraction. The joint system can be used for modulation on one hand or for sensing on the other hand. As a modulator the atomic system can be manipulated using optical, electrical or magnetic fields in order to modulate another probe field. When these fields are not induced but need to be measured, the system can act as a sensor. The characteristics of the system are defined by the complex susceptibility of the system and the detuning of the laser field. Recent technological advances in tunable narrow band laser sources and new techniques for producing dense atomic vapors with long coherence times offer new opportunities to take full advantage of these systems.

Modulation The spatial modulation and switching of light is vital to modern technology mainly in optical communication, bio-medical applications and laser and optics industries [21, 189]. The main tool for optical modulation today is solid state crystals,

where electrooptics, acusto-optics and non-linear optics are used in order to modulate and switch light [146]. One downside of solid state systems is that their optical properties are almost constant and hard to tune dynamically. Atomic media, on the other hand, has the advantages of high resolution spectral control and light induced switching [10] making it a compelling alternative for certain applications.

A variety of different methods for creating electromagnetically induced structures in atomic media have been discovered recently. These mechanisms include atomic optical pumping [93, 172], Hole-burning and the Faraday effect [24, 94]. Three level atomic systems and specifically EIT proved to be especially useful in modulating a probe beam using a strong pump. Wave guiding [181], optically induced grating [23, 107, 123], frequency dependent focusing and diffraction [124], diffractionless propagation, Negative diffraction and induced deflection [51, 54] were demonstrated recently showing the great potential of these systems.

Sensing Atomic spectroscopy has been used as a sensing technique for many years, exploiting shifts of energy levels due to electric (Stark) or magnetic (Zeeman) fields. The sensor resolution is directly related to the spectral lineshape. In the case of two level systems it is usually a Lorentzian having a natural linewidth. In atomic vapor this width is on the order of few MHz. When the atoms are warm this linewidth increases to ∼GHz due to Doppler broadening [163] that can be overcome by the use of saturated absorption techniques [35]. Much narrower linewidths can be achieved using three level atoms. EIT, for example, is a coherent process, where a strong coupling field creates a narrow transmission band in the probe spectrum in an otherwise fully absorptive medium [57, 129]. EIT linewidths as narrow as tens of Hz were measured [91].

These narrow linewidths make EIT suitable for high sensitivity spectral measurements. One application can be accurate atomic clocks [175], another promising direction is sensitive magnetic sensing [100, 193]. In recent years, many sensitive atomic magnetometry techniques such as nonlinear magneto-optical rotation [2], spin-exchange relax-

ation free (SERF) - Faraday rotation [7] and CPT [17] were demonstrated. Using buffer gas or paraffin coating the coherence of the ground state can become extremely long (up to ∼1 s) making the sensitivity of these magnetometers competitive with all other known sensitive magnetometric methods, most noteworthy of them superconducting quantum interference device (SQUID) [25].

Although atomic magnetometers can be extremely sensitive when measuring small magnetic fields, one drawback of the narrow linewidths is the limited bandwidth of data that can be processed. In terms of sensing this means that although a very high sensitivity is possible using EIT, it is a problem to probe with this sensitivity a broadband field in a simple way. Possible solutions to this problem is to use a multimode EIT system where each EIT line has still a narrow bandwidth but spreading the signal across many systems allows for a broader signal. Such systems were devised spatially [43] and spectrally [26, 190] for larger data capacity as well as for broadband magnetic sensing [17, 179]. A different approach is to use dynamic EIT where the transient response may have a much broader bandwidth than steady state EIT. Transients were used as a magnetic sensing technique to measure the Earth's magnetic field with $1.5\frac{nT}{\sqrt{Hz}}$ sensitivity [101].

quantum technology EIT narrow transmission linewidth implies also an extreme slow light that can reach almost pedestrian speeds of several m/s [76, 86]. The medium and light in this case can no longer be separated, but are best thought of as a joint entity of the spin wave and electromagnetic wave known as a dark state polariton [58]. The polariton is coherent, meaning it preserves the phase of its state, making it a very useful quantum light to matter transformer. In the extreme limit of the polariton, when it is purely atomic, the light is stopped, and the coherence can be sustained for a very long time. Hot atomic vapor coherence times are usually on the order of 100 μs, but coherence time of almost a minute was measured using cold atom systems [41]. The polariton can be switched back to the light part, thus the system behaves as a

quantum storage device. These devices are key components in the attempt to create viable long distance quantum networks. Photon loss in long fibers is detrimental to the preservation of a quantum state. Unlike classical systems where repeaters can be used to amplify the signal, a quantum state cannot by copied and hence amplified [184]. A solution to this problem was given by the means of quantum repeaters [22] which states that by using entanglement swapping (two-fold teleportation), shorter segments can be linked to a single entangled state across the whole distance. Each segment in this case should hold the quantum entanglement until the full chain is achieved meaning it has to contain a quantum storage device. In 2001 Duan-Lukin-Cirac-Zoller (DLCZ) proposed a practical way of implementing quantum repeaters using an EIT media [40]. This work opened a whole field of research trying to realize the DLCZ protocol [148]. Although the goal of a full quantum repeater channel is yet to be achieved, appreciable steps along this way have been made. Single excitations in alkali vapors were created and stored for more than a ms in cold atoms [194] and for a few μs in hot vapors [15, 174]. The atomic excitation was shown to be entangled with the single photon that was released upon its creation [31, 118], which led to the creation of entanglement between two or more distant atomic ensembles [32, 99].

This thesis contains experimental and theoretical results that contribute to all these three uses for atomic ensembles discussed above.

1.1 Outline

The outline of this thesis is as follows. In the remainder of this chapter I will present the relevant theoretical background. First, the interaction of two level atomic media with laser light will be described followed by a brief introduction to EIT theory. The last part of this introduction presents the role of three level atoms in the quest towards quantum repeaters and quantum communication. Chapter 2 is devoted to the exposition of the experimental methods that were applied throughout the research. Part of this chapter

also specifies benchmark EIT results that were achieved using our setup. Chapter 3 presents the main results and achievements of this thesis. The results chapter is divided into four sections. The first two sections deal with spatial control of light using atomic vapor. Section 3.1 presents the control of vortex array by the use of EIT media [160] and section 3.2 describes a way to create all optical photonic crystals through AC Stark manipulation [109]. Section 3.3 introduce a new method of probing the coherence of atomic media in general and EIT media specifically by analyzing the transients of a probe beam under strong phase modulations. Section 3.4 shows a way to create an entangled pair of photons in a heralded way using atomic vapor [159]. Chapter 4 gives some concluding remarks and future prospects.

1.2 Interaction of two level atom media with light

1.2.1 The Rabi problem

The electronic energy spectrum of atomic systems can be very complicated, but in many cases it can be reduced to an effective two level system. This happen when the interaction with an external field is weak and nearly resonant with two levels in the atom. The Hamiltonian of such a system is

$$H = \begin{pmatrix} 0 & V^* \\ V & \hbar\omega_{12} \end{pmatrix}, \tag{1.2.1}$$

where $\hbar\omega_{12}$ is the energy difference between the two levels and $V = -\overrightarrow{\mu}\cdot\overrightarrow{E}$ is the dipole interaction term with the electric field of the light. $\overrightarrow{\mu} = \langle 1|\,\vec{r}\,|2\rangle$ is the transition dipole moment, with $\vec{r}$ being the position operator, and $\overrightarrow{E}$ is the electric field which can be written as $E = E_0 cos\omega t = \frac{E_0}{2}(e^{i\omega t} + e^{-i\omega t})$ in the case of a monochromatic light.

In order to solve the master equation it is preferable to work in the rotating frame of the driving field, meaning that $|2\rangle \rightarrow e^{-i\omega t}|2\rangle$. Now the new Hamiltonian becomes:

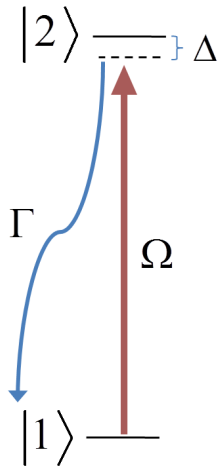

Figure 1.2.1: Two levels interaction with light.

$$H = \begin{pmatrix} 0 & V^* e^{-i\omega t} \\ V e^{i\omega t} & \hbar(\omega_{12} - \omega) \end{pmatrix}. \tag{1.2.2}$$

The off diagonal elements contain two kind of terms, one with no exponential in it and one with $e^{\pm 2i\omega t}$. The later is a fast rotating term with twice the optical frequency. In most cases we are interested with a much slower dynamics on the scale of the Rabi frequency, defined as $\Omega = \frac{\mu E_0}{\hbar}$. In this case the fast rotating terms averages out with very little effect on the atomic population and coherence, thus we can neglect these terms in what is called the rotating wave approximation (RWA) and the Hamiltonian becomes:

$$H = \hbar \begin{pmatrix} 0 & \frac{1}{2}\Omega^* \\ \frac{1}{2}\Omega & \Delta \end{pmatrix}. \tag{1.2.3}$$

Here $\Delta = \omega_{12} - \omega$ is the detuning of the laser from resonance.

Solving the Schrodinger equation, $i\hbar |\Psi\rangle = H |\Psi\rangle$ it is possible to find the population

of the two states. When the population is initially in the ground state, the probability of occupying level $|2\rangle$ is [155]:

$$P_2(t) = \frac{\Omega^2}{2\widetilde{\Omega}^2}[1 - \cos(\widetilde{\Omega}t)], \tag{1.2.4}$$

where $\widetilde{\Omega} \equiv \sqrt{\Omega^2 + \Delta^2}$ is the generalized Rabi frequency. Equation 1.2.4 reveals that the population is exchanged between the two levels at a frequency $\widetilde{\Omega}$. Moreover in the case of resonance there is a total transfer of the population to level $|2\rangle$, while off resonance the maximal population is smaller. In the far detuned case, $\Delta \gg \Omega$, the population of level $|2\rangle$ scales as $1/\Delta^2$, hence there is no substantial excitation.

1.2.2 Optical Bloch equations

In real systems the transition between the two levels is subjected also to decay and decoherence mechanisms. In order to incorporate the decay we will use the density matrix formalism as this is a natural way for treating lossy systems. The general equation for the density matrix evolution in time is the master equation :

$$\frac{\partial \rho}{\partial t} = \frac{i}{\hbar}[H, \rho] + \mathcal{L}\rho \tag{1.2.5}$$

where ρ is the density matrix

$$\rho = \begin{pmatrix} \rho_{11} & \rho_{12} \\ \rho_{21} & \rho_{22} \end{pmatrix} \tag{1.2.6}$$

and $\mathcal{L}$ represents the Liouvillian superoperator of the system due to decay and decoherence processes. In the case of spontaneous decay $\mathcal{L}\rho = -\frac{\Gamma}{2}(\sigma_+\sigma_-\rho - 2\sigma_-\rho\sigma_+ + \rho\sigma_+\sigma_-)$, where $\sigma_+ = |2\rangle\langle 1|$, $\sigma_- = |1\rangle\langle 2|$ and the decay rate is given by $\Gamma = \frac{\omega_{12}^3 |\vec{\mu}|^2}{3\pi\varepsilon_0\hbar c^3}$ [163]. Now it is possible to write the master equation for each density matrix element which are called the optical Bloch equations:

$$\frac{\partial \rho_{11}}{\partial t} = -i\frac{\Omega}{2}(\rho_{12}-\rho_{21}) + \Gamma\rho_{22} \tag{1.2.7a}$$

$$\frac{\partial \rho_{22}}{\partial t} = i\frac{\Omega}{2}(\rho_{12}-\rho_{21}) - \Gamma\rho_{22} \tag{1.2.7b}$$

$$\frac{\partial \rho_{12}}{\partial t} = -(\frac{\Gamma}{2}+i\Delta)\rho_{12} - i\frac{\Omega}{2}(\rho_{22}-\rho_{11}) \tag{1.2.7c}$$

and the last term can be found from $\rho_{12} = \rho_{21}^*$. The steady state solution to the population is:

$$\rho_{22} = \frac{\Omega^2/\Gamma^2}{1+(\frac{2\Delta}{\Gamma})^2 + 2\frac{\Omega^2}{\Gamma^2}}. \tag{1.2.8}$$

We can write this in the form of intensity as the Rabi frequency goes like the electric field. Recalling that $I = \frac{\epsilon_0 c}{2}E_0^2$ we can write $\frac{I}{I_{sat}} = \frac{2\Omega^2}{\Gamma^2}$ with $I_{sat} = \frac{c\epsilon_0\Gamma^2\hbar^2}{4\mu^2}$ being the saturation intensity. Now it is possible to write the population of the upper level on resonance as:

$$\rho_{22} = \frac{1}{2}\frac{I/I_{sat}}{1+I/I_{sat}}. \tag{1.2.9}$$

Equation 1.2.8 as a function of detuning is a Lorentzian (see Fig. 1.2.2). It has two extremes, when the intensity is small ($\Omega \ll \Gamma$) the width of the Lorentzian is Γ and the population of the excited state is $(\Omega/\Gamma)^2$, while if the intensity is high ($\Omega \gg \Gamma$) the width of the Lorentzian is $\sqrt{2}\Omega$ and the population of the excited state is $1/2$. The broadening of the transition due to the high intensity is termed power broadening.

1.2.3 Susceptibility

We saw that an electromagnetic field passing through a two level system media causes a change in the atomic population, but the opposite is also true. Namely, a polarized atomic media can change the amplitude and phase of the light that passes through it. This is a direct effect of the Maxwell wave equation inside the media:

$$\nabla^2 E + \frac{1}{c^2}\frac{\partial^2 E}{\partial t^2} = \frac{1}{\epsilon_0 c^2}\frac{\partial^2 P}{\partial t^2}, \tag{1.2.10}$$

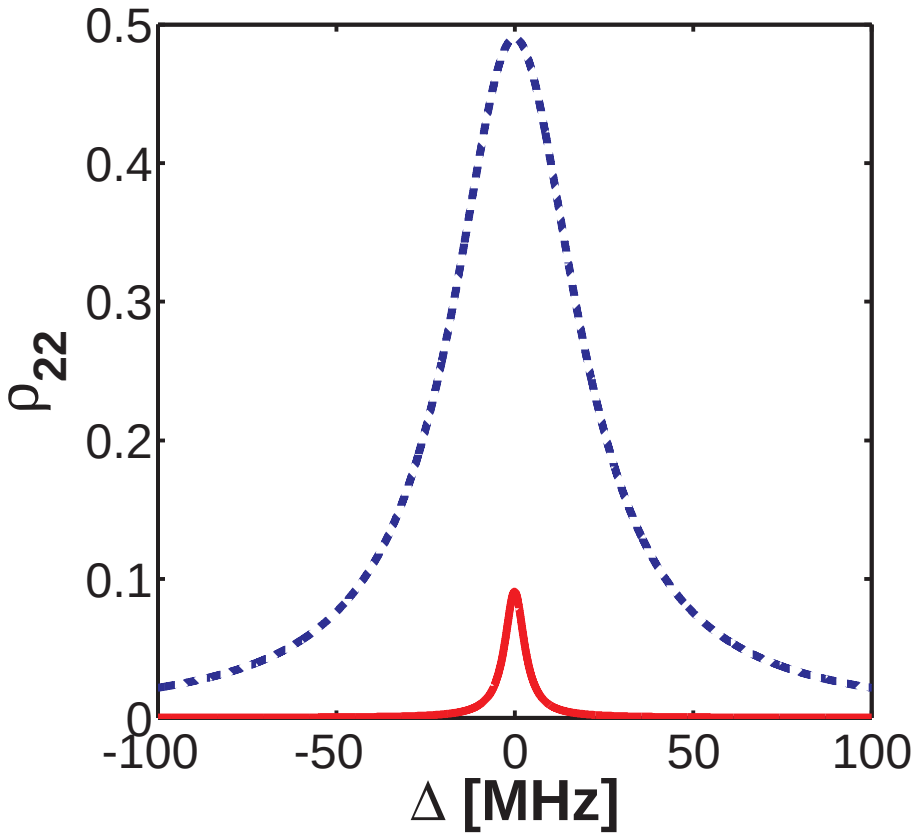

Figure 1.2.2: Steady state population of the excited state according to Eq. 1.2.8. Blue dashed curve - $\Gamma = 6$ MHz, $\Omega = 30$ MHz. Red curve - $\Gamma = 6$ MHz, $\Omega = 2$ MHz.

with $P = N\rho_{12}\mu_{12}$ the macroscopic polarization which is just the density of the atomic dipole moments (N being the density of the atoms). This equation together with Eq. 1.2.7a-1.2.7c form a closed self contained set that solves the atomic and light states altogether. The polarization of the media can be expanded as a power series of the electric field. For weak electric field only the linear term is relevant, thus it is possible to write $\overrightarrow{P} = \epsilon_0 \chi \overrightarrow{E}$, where χ is the susceptibility of the medium. Solving the Maxwell-Bloch equations under steady state conditions with a perturbative probe field results in the following susceptibility [163]

$$\chi = i\frac{N\mu^2}{\epsilon_0 \hbar}\frac{1}{\Gamma/2 - i\Delta}. \tag{1.2.11}$$

The susceptibility is a complex Lorentzian with a FWHM width of Γ. If there is an additional decoherence such that $\gamma = \frac{\Gamma}{2} + \gamma_c$, where γ_c can be decoherence due to collisions or external noise, then the Lorentzian in Eq. 1.2.11 has a FWHM width of 2γ. The real and imaginary part of the susceptibility are depicted in Fig. 1.3.2(a). In order to understand better the meaning of the susceptibility let us remember that the propagation of a plane electromagnetic wave in the matter is

$$E(z,t) = \mathrm{Re}\Big[Ee^{i(\omega t - kz)}\Big], \tag{1.2.12}$$

where $k = (1+\chi)^{1/2} k_0$ and $k_0 = \frac{\omega}{c}$ is the wave number of the light in free space. k can be expanded in a Taylor series and for a weakly absorbing media such as a gas of two level atoms $k = \left(1 + \frac{1}{2}\chi\right) k_0$ [146]. The electric field can be written as

$$E(z,t) = \mathrm{Re}\Big[Ee^{i(\omega t - k_0(1+\frac{1}{2}Re(\chi))z) - \frac{1}{2}k_0 Im(\chi)z}\Big]. \tag{1.2.13}$$

Thus the absorption of the medium is dependent on the imaginary part of the susceptibility - $\alpha = \mathrm{Im}(\chi)k_0$ and the index of refraction is related to the real part of the susceptibility - $n = 1 + \frac{1}{2}\mathrm{Re}(\chi)$.

1.2.4 Dressed states

The Hamiltonian derived in Eq. 1.2.3 can be diagonalized with eigenvalues

$$\varepsilon_{\pm} = \frac{1}{2}\Delta \pm \frac{1}{2}\tilde{\Omega} \tag{1.2.14}$$

and a new set of eigenstates called dressed states [155]:

$$\begin{aligned} |+\rangle &= \sin\theta\,|1\rangle + \cos\theta\,|2\rangle \\ |-\rangle &= \cos\theta\,|1\rangle - \sin\theta\,|2\rangle \end{aligned} \tag{1.2.15}$$

where θ is the mixing angle defined as $\tan 2\theta = \frac{\Omega}{\Delta}$. Level $|2\rangle$ is a function of the

detuning meaning that when the detuning is zero the two bare level cross. Due to the coupling, the two bare levels mix near the resonance, consequently shifting the energies. The crossing in this case is avoided as shown in Fig. 1.2.3.

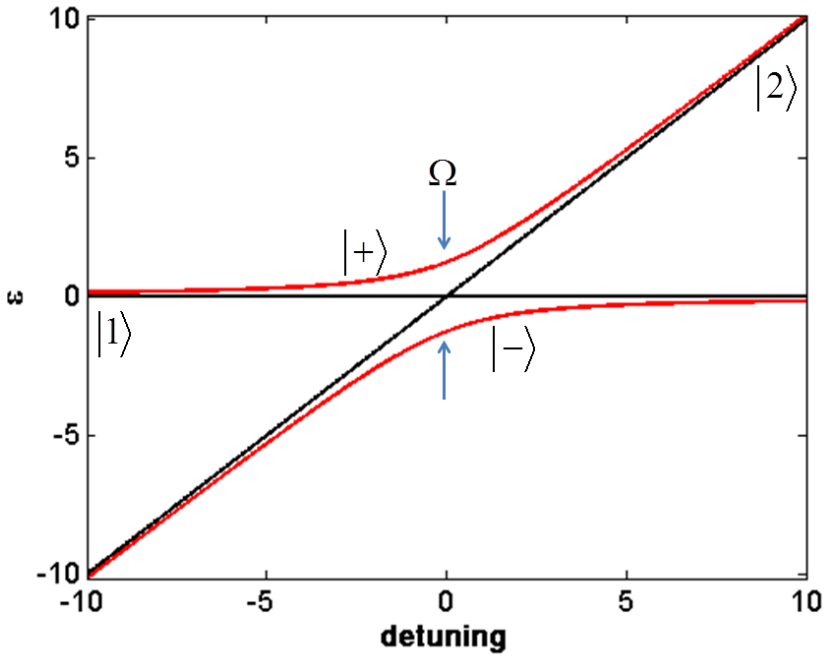

Figure 1.2.3: Avoided level crossing

The shift created is called the AC Stark shift. The shift in energy is $\pm\frac{\hbar}{2}\sqrt{\Delta^2+\Omega^2}$. We can look at the shift behavior in two extremes: (a) $\Delta \ll \Omega$ - the shift is $\Delta\omega_{Stark} \approx \hbar\Omega$. (b) $\Delta \gg \Omega$ - the shift is $\Delta\omega_{Stark} \approx \frac{\hbar\Omega^2}{4\Delta}$. Hence, the shift for large detunings behave linearly with the intensity of the laser while for small detunings it is linear with the square root of the intensity.

1.3 EIT basics

We now turn to deal with a more complicated atomic structure that arises from a quantum system of three energy levels. This additional level produces many new phenomena that are very different from those in two level atoms. The main part of this section will be devoted to EIT theory, the results and the challenges associated with it, but for completeness we first describe the more general case of coherent population trapping (CPT) [70].

1.3.1 The Atomic framework

EIT can be observed in multilevel systems but it is most pronounced in a three levels system. The basic EIT system is comprised from a quantum system of three energy levels $|1\rangle, |2\rangle, |3\rangle$ with energies $\hbar\omega_1$, $\hbar\omega_2$ and $\hbar\omega_3$ respectively, that interact through the atomic dipole with two coherent fields. The interaction term can be written, exactly as we described in Sec. 1.2, as $V_\alpha = -\overrightarrow{\mu_{ij}}\cdot\overrightarrow{E_\alpha}$, where $\overrightarrow{\mu_{ij}}$ is the transition dipole moment between levels $|i\rangle$ and $|j\rangle$ and $\overrightarrow{E_\alpha}$ is the electric field of one of the two laser fields. We will denote the fields $\alpha = p, c$ standing for probe field and coupling field. These two fields are nearly resonant with transitions $|1\rangle \rightarrow |3\rangle$ and $|2\rangle \rightarrow |3\rangle$ respectively, while the third transition is always a forbidden dipole moment transition due to selection rules [74, 155]. The three possible formations of these systems are called lambda (Λ), Vee (V) and ladder. In this work I will deal only with a lambda system (Fig. 1.3.1), although the characteristics of the other two are similar. This system is the basis also for various coherent phenomena such as CPT which will be discussed next.

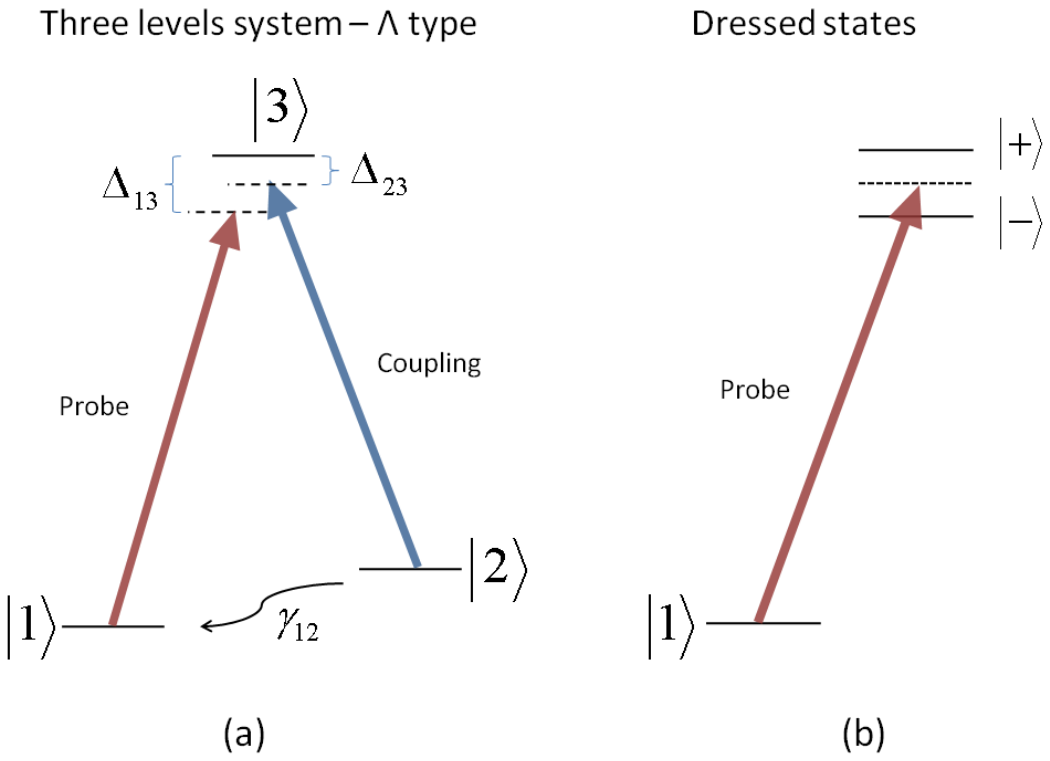

Figure 1.3.1: EIT system. (a) basic EIT lambda (Λ) system. (b) dressed states picture. Δ_{13} and Δ_{23} are the one photon detunings of the probe and the coupling fields respectively. γ_{12} is the decoherence rate of the lower levels.

1.3.2 Coherent population trapping

Similar to the two level case, we can write the system Hamiltonian using the rotating wave approximation (RWA)

$$H_{int} = \frac{\hbar}{2}\begin{pmatrix} 0 & 0 & \Omega_p^* \\ 0 & 2\delta & \Omega_c^* \\ \Omega_p & \Omega_c & 2\Delta_{13} \end{pmatrix}, \tag{1.3.1}$$

where $\delta = \Delta_{13} - \Delta_{23}$ is termed the two photon detuning and Δ_{13}, Δ_{23} are the standard one photon detunings as defined in Fig. 1.3.1 [57]. We wish now to try decouple part of the system from the two fields. It is obvious that the bare ground levels are coupled to the light so a different basis is needed. We can change the basis

to the following orthonormal one $\{|3\rangle, |B\rangle, |D\rangle\}$ where [8]

$$\begin{aligned} |B\rangle &= \tfrac{1}{\sqrt{\Omega_p^2+\Omega_c^2}}\left(\Omega_p|1\rangle + \Omega_c|2\rangle\right) \\ |D\rangle &= \tfrac{1}{\sqrt{\Omega_p^2+\Omega_c^2}}\left(\Omega_c|1\rangle - \Omega_p|2\rangle\right) \end{aligned} \tag{1.3.2}$$

The transition matrix elements of the new basis are

$$\langle 3|H|B\rangle = \frac{\hbar}{2}\sqrt{\Omega_p^2+\Omega_c^2} \tag{1.3.3a}$$

$$\langle 3|H|D\rangle = 0 \tag{1.3.3b}$$

$$\langle D|H|B\rangle = \hbar\delta\frac{\Omega_p\Omega_c}{\Omega_p^2+\Omega_c^2} \tag{1.3.3c}$$

Eq. 1.3.3b shows that there is no dipole transition between state $|D\rangle$ and the excited level $|3\rangle$, hence this state is decoupled from the excited state. Moreover, exactly on two photon resonance it is totally decoupled from state $|B\rangle$ also. State $|D\rangle$ is termed the *dark state* since an atom at that state will not absorb the laser light anymore. It is also called the trapped state because the population at this state cannot exit via H_{int}. Once the laser fields are on, the population will eventually pump to the dark state due to spontaneous emission [163]. The process of creating a medium with fully trapped population is called *coherent population trapping.* Another related concept is the one of coherent population transfer, where the population is transferred from level $|1\rangle$ to level $|2\rangle$ without going through the excited level. This is done by a process called STIRAP (stimulated rapid adiabatic passage) [155], which is a pulsed process that starts with a strong coupling pulse ($\Omega_c \gg \Omega_p$) hence state $|D\rangle = |1\rangle$ and state $|B\rangle = |2\rangle$. Now the coupling field is turned off gradually while the probe field is turned on in such a way that in the end $\Omega_p \gg \Omega_c$ and $|D\rangle = |2\rangle$. The population was transferred while the system is always in the dark state. The process of STIRAP is counter-intuitive in the sense that in order for it to occur the coupling field should be turned on before the probe field, although the population is residing initially at level $|1\rangle$ which is not interacting with the coupling field directly.

The dark state, being formed as a superposition of ground states, has a much longer lifetime than the excited state, thus creating a very narrow spectral feature. This effect drew a lot of attention during the years to CPT with applications in metrology and atomic clocks [175].

1.3.3 EIT theory

Unlike CPT and STIRAP where the redistribution of the atomic population is the main focus, EIT is a process where the population is residing in level $|1\rangle$ throughout the interaction. Technically the difference between the two phenomena is due to the fact that in CPT both fields have comparable intensities while in EIT systems the coupling field is much stronger than the probe field. The strong interacting coupling field affect the probe field via the atomic system leading to many interesting dynamical and spectroscopical effects [116].

Quantum interference

The main feature of EIT, the narrow transparency window can be easily explained using the formalism of CPT. EIT is the case where $\Omega_c \gg \Omega_p$, thus just as we mentioned regarding STIRAP, the dark state is equal to level $|1\rangle$, meaning that the probe field is not interacting with it and is not absorbed. When the two photon detuning is not zero there is a coupling between the dark state and the bright state, which interacts with the probe field, and hence the light is absorbed. A different approach that gives intuition to EIT is to treat it as an interference process. When a two level system is subjected to strong external field a splitting of the levels occur due to the AC Stark effect. This splitting can be probed by a different transition from one of the two original levels to a third one, the observed probe spectrum is called Autler-Townes splitting [14]. The size of the splitting is the AC stark shift $\Omega_{eff} = \sqrt{\Omega_c^2 + \Delta_c^2}$. If the third level is probed with a resonant weak probe field, $\Omega_c \gg \Omega_p$, the system is turned into an EIT one. The major difference is that the probe sees now two new nearly resonant states that

are called dressed states (see Fig. 1.3.1(b)). Using the weak probe assumption and diagonalizing the $|2\rangle, |3\rangle$ subspace in matrix 1.3.1, we arrive at the two new dressed states, which in the case of the coupling field resonance ($\Delta_{23} = 0$) are given by :

$$|+\rangle = \frac{1}{\sqrt{2}}(|2\rangle + |3\rangle) \tag{1.3.4a}$$

$$|-\rangle = \frac{1}{\sqrt{2}}(|2\rangle - |3\rangle) \tag{1.3.4b}$$

The transition amplitude for the probe will be $A_{1\to3} = \langle 1|\mu|+\rangle + \langle 1|\mu|-\rangle = 0$, Hence at resonance there is no absorption of the probe - EIT. It is possible to look at this result also from the quantum perspective of interference between sum of all pathways. In this picture, Because of the strong coupling, the amplitude of the two quantum pathways for the probe transition, $1 \to 3$ and $1 \to 3 \to 2 \to 3$, are comparable and interfere destructively [116].

EIT susceptibility

In real EIT systems the transition between the two lower levels is not zero and the system is governed by several decay and decoherence mechanisms that will be described later in details in Sec. 1.3.6. For the proper description of real EIT systems we will use the density matrix formalism, as this is a natural way for treating lossy systems. Using the EIT interaction Hamiltonian (1.3.1) with the master Eq. 1.2.5 we arrive at

the following set of equations for the different density matrix terms [53, 57]

$$\dot{\rho}_{11} = -2\mathrm{Im}\Omega_{\mathrm{p}}^{*}\rho_{31} + \Gamma_{31}\rho_{33} \tag{1.3.5a}$$

$$\dot{\rho}_{22} = -2\mathrm{Im}\Omega_{\mathrm{c}}^{*}\rho_{32} + \Gamma_{32}\rho_{33} \tag{1.3.5b}$$

$$\dot{\rho}_{33} = 2\mathrm{Im}(\Omega_{\mathrm{p}}^{*}\rho_{31} + \Omega_{\mathrm{c}}^{*}\rho_{32}) - (\Gamma_{31} + \Gamma_{32})\rho_{33} \tag{1.3.5c}$$

$$\dot{\rho}_{21} = -i\delta\rho_{21} + i\Omega_{c}^{*}\rho_{31} - i\Omega_{1}\rho_{32} - \gamma_{21}\rho_{21} \tag{1.3.5d}$$

$$\dot{\rho}_{31} = -i\Delta_{13}\rho_{31} - i\Omega_{p}(\rho_{33} - \rho_{11}) + i\Omega_{c}\rho_{21} - \Gamma_{C}\rho_{31} \tag{1.3.5e}$$

$$\dot{\rho}_{32} = -i\Delta_{23}\rho_{32} - i\Omega_{c}(\rho_{33} - \rho_{22}) + i\Omega_{p}\rho_{21} - \Gamma_{C}\rho_{32} \tag{1.3.5f}$$

The other matrix elements can be found using $\rho_{ij} = \rho_{ji}^{*}$. Γ_{31} and Γ_{32} are population decay constants from the excited level to the ground levels, γ_{21} is the decoherence rate of the two ground states[1] and $\Gamma_{c} = {}^{\Gamma_{31}+\Gamma_{32}+\gamma_{21}}/_{2}$. The steady state populations due to the strong coupling field are approximately $\rho_{11} \approx 1$ and $\rho_{22} = \rho_{33} \approx 0$.

Now we can calculate χ - the linear susceptibility of the system by using the steady state solutions to these equations. χ is proportional to ρ_{31}, as the polarization of the system is $P = N\mu_{31}\rho_{31}$ with N being the density of the atoms. In the case of EIT we derive the following equation for the linear susceptibility [57] :

$$\chi(\omega_{p}) = i\frac{N\mu_{31}^{2}}{\epsilon_{0}\hbar}\frac{1}{\left((\Gamma - i\Delta_{13}) + \frac{(\Omega_{c})^{2}}{\gamma_{21} - i\delta}\right)}. \tag{1.3.6}$$

The important features of EIT susceptibility, namely a very sharp transparency window and a very steep positive slope for the index of refraction, can be seen in fig. 1.3.2. These unique features that are very different from the normal two levels susceptibility, give EIT media its attractiveness. The FWHM of the EIT susceptibility

[1] We did not add any population decay rate between the two ground states. Due to the forbidden dipole moment transition between these two levels the population decay will be totally dominated by dephasing effects.

peak resulting from Eq. 1.3.6 is

$$FWHM_{EIT} = 2\left(\gamma_{12} + \frac{|\Omega_c|^2}{\Gamma}\right). \tag{1.3.7}$$

Since the ground state decoherence rate can be very small, EIT peaks can be more than 5 orders of magnitude narrower than the natural linewidth ($\sim 6MHz$ for Rb).

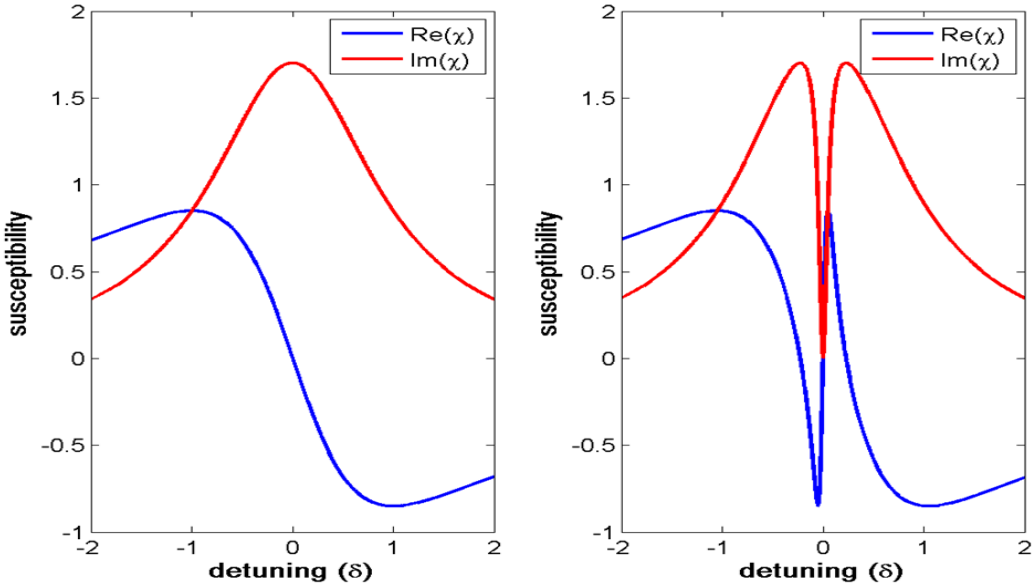

Figure 1.3.2: EIT susceptibility. Left image shows the calculated susceptibility for the probe frequency without coupling field. right image shows the susceptibility when adding the coupling field, i.e., EIT system. blue - Real part of the susceptibility. Red - Imaginary part of the susceptibility.

1.3.4 Slow light

The sharp slope of Re(χ) around the two photon resonance creates a situation where the derivative of the index of refraction can be enormous with respect to a normal

medium. The group velocity of light inside the media is

$$V_g = \frac{\partial \omega}{\partial k} = \frac{c}{n(\omega) + \omega(\frac{dn}{d\omega})}, \tag{1.3.8}$$

thus, in EIT media where $\frac{dn}{d\omega}$ can be very large, the group velocity of the light at resonance can be very low. The index of refraction is $n(\omega) = 1 + \frac{1}{2}\mathrm{Re}(\chi) \approx 1$, thus we can calculate the derivative and find the effective group index of refraction on resonance to be

$$n_{eff} = \omega \frac{\partial n}{\partial \chi}\frac{\partial \chi}{\partial \omega}\bigg|_{\delta=0} = \frac{\omega N \mu_{31}^2}{2\epsilon_0 \hbar \Omega_c^2}. \tag{1.3.9}$$

For small enough coupling field and dense media this group index of refraction can be very high. Pulses traveling in an EIT medium with group velocities as low as $17\,{}^{m}/_{sec}$ have been measured [76]. One more important issue regarding slow light is the fact that as the frequency remains the same, the pulse is actually reduced spatially by the same factor as the velocity is slowed. A $1\,\mu s$ pulse, for example, will be $300\,m$ long in vacuum but can be as short as tens of microns inside the EIT medium. As $\mathrm{Re}(\chi)$ and $\mathrm{Im}(\chi)$ are related through the Kramers-Kronig relations, very narrow transparency window will lead to extremely low velocities, but this relation also leads to an important limitation of light slowing - the delay-bandwidth product. In order to create an efficient slowing of a pulse its bandwidth must be contained inside the EIT bandwidth. Otherwise there will be parts of the pulse that will not be slowed down. The time delay for an EIT media with a length L will be $t_d = {}^{n_{eff}L}/_{c}$. We can define the transmission window width of EIT using this delay time (assuming zero ground state decoherence) [58]

$$\Delta\omega_T = \frac{\Omega_c^2}{\Gamma}\frac{1}{\sqrt{\alpha L}} = \sqrt{\alpha L}\frac{1}{t_d}, \tag{1.3.10}$$

where α is the absorption coefficient of the medium without the coupling field and αL is just the optical density (OD) of the medium. This means that the delay-bandwidth product, $\Delta\omega_T \times t_d = \sqrt{\alpha L}$, is given by the OD [170,173]. Using the Fourier relation we

can write the shortest pulse that can be efficiently slowed to be $\Delta t_p = {}^1/_{\Delta\omega_T}$, thus the ratio between the pulse length and the slowing time is

$$\frac{t_d}{\Delta t_p} \leq \sqrt{\alpha L}. \tag{1.3.11}$$

This relation shows that in order to have a substantial delay of the pulse the media should be optically thick.

1.3.5 storage

Storage of light has been one of the main goals for EIT usage [139]. The scheme is as follows: First the probe pulse passes through the media while the coupling is on. Once all the pulse is accommodated inside the cell, turning off the coupling will cause the probe pulse to be absorbed fully in the media as the absorption at resonance is very high. If the coupling is then turned on after some time, the original probe pulse reappears. In an ideal EIT the probe pulse is fully recovered, but as there are decoherence processes the storage time is finite. The explanation for storage of light in EIT can be given in the context of spin wave polaritons [59]. In the presence of a coupling field, the atomic spin wave function and the probe light are no longer separate systems but are in a superposition termed *dark state polariton*. Mathematically the polariton can be written as follows:

$$\Psi(z,t) \quad = \quad \cos\theta E_p(z,t) - \sin\theta\sqrt{N}\rho_{21}e^{i\Delta kz}, \tag{1.3.12}$$

where θ, the mixing angle, is defined by $\tan^2\theta = n_{eff}$ and $\Delta k = k_c - k_p$ is the wavevector mismatch between the coupling and probe fields in the case of copropagating beams. The polariton obeys a simple wave equation dynamics with a group velocity $v_g = c\cos\theta$. When the coupling is on, the polariton is moving in the medium with the slow light group velocity, but as soon as the coupling is shut off the polariton is reduced solely to an atomic spin wave having zero group velocity. This effect is reversible,

and thus when the coupling is turned on again, light reemerges [5, 139]. Proofs of the principle for light storage were demonstrated in warm Rubidium vapor with buffer gas and paraffin coated walls, where storage times of up to $\sim 1\,ms$ were achieved [129]. More recently storage of pictures were demonstrated in warm Rb cells [158, 180]. Using cold atoms even longer storage times of up to a minute where achieved [41, 150]. Another medium that was shown to have great potential for storage is rare-earth ion doped solid materials, where recently an EIT storage of over a minute was observed [79]. EIT is not the only way long storage times can be achieved. Some other methods include photon echoes techniques such as Controlled Reversible Inhomogeneous Broadening (CRIB) and Gradient Echo Memory (GEM) [171] and Atomic Frequency Comb (AFC) [3].

1.3.6 Decoherence

The fundamental limitation of the EIT process lies in the decoherence between the two lower levels. As can be seen in Eq. 1.3.7 the smallest width that can be achieved is $2\gamma_{12}$. As the group velocity and the storage time is related to this width, it is apparent that decreasing decoherence can improve the practical usefulness of the EIT media. Apart from the basic atomic limit of nonzero transition matrix element between the two lower levels due to higher electric moments, there are several mechanisms that cause broadening of the width. Fortunately, there are also mechanisms that cause narrowing. In the following I shall give a brief description of the broadening processes followed by the narrowing processes.

Broadening processes

- Collisions - a basic relaxation mechanism of atomic coherence is strong collisions with other atoms and with the walls. Typically at EIT working temperatures for rubidium ($30°C$-$80°C$) the vapor pressure is $P \sim 10^{-5} - 10^{-7}$ Torr and the thermal velocity is $v_{th} \sim 250^{m}/_{s}$, hence atomic collisions rate is ∼10-1000 Hz and the relaxation due to collisions with the walls (for standard diameter of 2.5 cm)

is ∼10 kHz. This effect can be lowered substantially using buffer gas and paraffin coating that preserve the coherence of the atoms due to elastic collisions [130].

- Magnetic field broadening - Due to the Zeeman shift, variable magnetic field can cause line broadening $\Delta\omega_B = \frac{g_F \mu_B \Delta B \Delta m_F}{\hbar}$, where g_F is Lande factor, μ_B is the Bohr magneton, ΔB is the change in magnetic field and Δm_F is the difference between the two hyperfine Zeeman sub-levels . This broadening can be minimized by minimizing stray magnetic field, using $\mu-$metal shielding for example. In our case a 3-layers $\mu-$metal shielding offers a 4 orders reduction in the magnetic field. For the two ground states of ^{87}Rb $\frac{g_F \mu_B}{\hbar} = 0.7$ MHz/G, hence a typical noise of ∼10 μG will cause a broadening of $\Delta\omega_B =\sim 10$ Hz.

- Laser line width - For two level atoms the laser width will cause additional broadening. In a lambda system, when the width of the laser should be less than the natural line width, this broadening can be canceled using phase locked lasers or using the same laser for both coupling and probe fields.

- Transit time - For finite size beams, atoms that move perpendicular to the beam will experience EIT conditions for finite time behaving as a pulse in time, thus causing spectral broadening. The EIT profile will be cusp like with a width of $FWHM = \frac{2v_{th}}{d}$, where v_{th} is the thermal speed of the atoms and d is the 1/e beam diameter [168]. A 1 cm beam diameter for example will have broadening of 50 kHz. This is the main mechanism that determines the EIT width with non buffer gas media. Adding a buffer gas results in a diffusive movement of the atoms reducing the transit time by up to three orders of magnitude (using buffer gas with pressure of ∼10 Torr).

- Raman Doppler broadening - When the two beams do not have the same wavenumber the detunings become velocity dependent. This occurs naturally when hyperfine transitions are used. The effect on the EIT linewidth is similar to optical Doppler broadening only with the Raman wavelength [56]. The broadening can

be described as a transit time broadening, hence for rubidium with a 6.8 GHz splitting the broadening will be at room temperature ∼10 kHz. Specifically, when the beams are not parallel a Doppler broadening with very strong angular dependence is observed [28]. Typically, for rubidium with buffer gas the peak starts to broaden at $0.2\,mrad$ and completely disappears above background noise at about $1\,mrad$ [157]. In the next section a narrowing process that eliminates this broadening will be discussed.

- Power broadening - This broadening is not related to the fundamental decoherence rate but rather to the width of the EIT as a function of the coupling field power. The basic result given in Eq. 1.3.7 is $FWHM = \frac{\Omega_c^2}{\Gamma}$. This is true as long as no movement of the atoms is taking place. For warm vapor we can write a more generalized form of the width $FWHM = \frac{\Omega_c^2}{W_{eff}}$ where W_{eff} can be a function of the Rabi frequency. There are two regimes as a function of the coupling power. At low coupling power such that $\left(\frac{\Omega_c}{W_d}\right)^2 \ll \frac{2\gamma_{12}}{\Gamma}$, where W_d is the Doppler width, only part of the atoms which have a velocity class that is close to resonance will participate in the EIT. In this case W_{eff} will be a linear function of the coupling Rabi frequency and the width will be $FWHM = \Omega_c\sqrt{\frac{\gamma_{12}}{\Gamma}}$. When the coupling field is strong enough that $\left(\frac{\Omega_c}{W_d}\right)^2 \gg \frac{2\gamma_{12}}{\Gamma}$ there is an efficient pumping to all velocity classes causing all atoms to participate in the EIT. The width in this case will become $FWHM = \frac{\Omega_c^2}{W_d}$ [84, 191]. This means that for high intensities the power broadening will be reduced. Adding a buffer gas to the cell can create this effect of reduced broadening even for low coupling intensities. This is caused by the fact that the atoms explore all the Doppler velocity classes during the transit time due to velocity changing collisions with the buffer gas. This will cause the width of the EIT to be broadened as follows $FWHM = \frac{\Omega_c^2}{W_d+\Gamma_p}$, where Γ_p is the pressure broadening [66]. The power broadening of rubidium vapor with buffer gas was measured in our setup resulting in W_{eff} ∼500 MHz (see 2.5.2 for more details), This result fits the theory as the Doppler broadening is also W_d ∼500 MHz.

Narrowing processes

- Dicke - Raman Doppler broadening can be canceled if the atoms experience frequent velocity changing collisions with a buffer gas [48]. The idea behind this narrowing is that if the coherent preserving collision rate is much faster than a substantial phase change, the wave that is emitted before and after the collision can add up coherently and produce large amplitude at the up-shifted frequency [36,186]. The Doppler regime or ballistic regime will occur when the mean free path of the atoms (Λ) is much longer than the Raman wavelength (λ_R). In the opposite case, $\Lambda \ll \lambda_R$, the dynamics is diffusive and it is called the Dicke regime. The EIT linewidth in this case will be narrower by a factor of $\sim \frac{2\pi\lambda_R}{\Lambda}$ [56].

- Ramsey - When buffer gas or wall coating are introduced to the EIT cell, transit time broadening may be diminished. The long coherence time of the atoms enables a situation where the atoms may travel in and out of the beam several time. Ramsey fringes will appear due to the interference between the two different phases of the lower levels. When the atom goes in and out of the beam multiple times, these fringes will average out canceling the transit time broadening, for extremely long spectroscopic integration times [187].

1.4 Quantum communication using atomic vapor

The coherent nature of collective spin excitation in EIT media makes it an exciting candidate for a quantum interface between light and matter [72]. In 2001 Julsgaard et al. demonstrated entanglement between two atomic ensembles using non local Bell measurement [85]. Since then many experiments and protocols revealed quantum effects for macroscopic EIT media [152] as well as for quantum light that is stored or emitted from the medium. In this section I will first present briefly what is entanglement, how it can be measured and how it can be useful in order to transfer quantum data by way of teleportation. In the following subsection I will describe the DLCZ protocol for quantum repeaters and its experimental realizations.

1.4.1 Entanglement

The building block of quantum information and computation is the quantum bit, or qubit. The qubit, very much like in classical computation, can have one of two states $|0\rangle$ or $|1\rangle$, but contrary to its classical counterpart the qubit can be also in a superposition

$$|\psi\rangle = \alpha\,|0\rangle + \beta\,|1\rangle\,. \tag{1.4.1}$$

α and β are complex probability amplitudes that satisfy the normalization $|\alpha|^2 + |\beta|^2 = 1$. Measurement of the qubit can yield only states $|0\rangle$ or $|1\rangle$ with probabilities $|\alpha|^2$ or $|\beta|^2$, hence the measurement of $|\psi\rangle$ directly is not possible.

A system of two qubits is spanned by four states $|00\rangle$, $|10\rangle$, $|01\rangle$ and $|11\rangle$, thus a general two-qubit state can be written as a superposition of these states

$$|\psi\rangle = \alpha_{00}\,|00\rangle + \alpha_{10}\,|10\rangle + \alpha_{01}\,|01\rangle + \alpha_{11}\,|11\rangle\,.$$

Generally, the two-qubit state is an entangled state. Entanglement is a unique property of quantum multisystems that lies in the heart of quantum theory, where the state of

one system is not independent of the others [135]. The nature of entanglement can be seen in the most pronounced way when observing the maximally entangled Bell states

$$\begin{aligned} |\phi^{\pm}\rangle &= \tfrac{1}{\sqrt{2}}(|00\rangle \pm |11\rangle) \\ |\psi^{\pm}\rangle &= \tfrac{1}{\sqrt{2}}(|10\rangle \pm |01\rangle). \end{aligned} \tag{1.4.2}$$

If the system is in one of the Bell states then upon measuring one qubit, the second qubit is dependent upon the first measurement outcome. For example, if the state is $|\phi^{\pm}\rangle$ then the first qubit can be either $|0\rangle$ or $|1\rangle$, but upon measuring $|0\rangle$, the second qubit has to be also $|0\rangle$. Entanglement manifests the inseparability of the two-qubit state as these states cannot be described as a product of single qubits. An important property of entanglement is its non-locality, meaning that the results stated above is valid even if the two qubits are separated. This manifestation of the quantum theory was challenged by Einstein, Podolsky, and Rosen (EPR). They claimed quantum theory lacks an element of reality, and offered an experiment that can prove that the apparent quantum correlations are in fact due to hidden variables [44]. In 1964 John Bell devised a set of inequalities regarding the statistical measurements of the EPR experiment that can differentiate between quantum theory and other hidden variables theory [18]. Since then many experimental systems were constructed in order to check these inequalities and all of them confirmed quantum theory as those inequalities were violated [12, 13, 128].

An important consequence of the non-locality of entanglement is its usage as a teleportation mechanism [19]. The idea is an immediate transfer of an unknown quantum state from one system to another system that can be far apart via two-particle entanglement. Due to the no-cloning theorem [184] which states that a separable quantum state cannot be copied, teleportation becomes the only way to convey quantum information over great distances. We shall now explain the teleportation protocol which requires three qubits. We wish to teleport an unknown state $|\psi_{in}\rangle_1 = \alpha\,|0\rangle_1 + \beta\,|1\rangle_1$, with the index 1 denoting the first qubit, from place A to place B. In B an entangled state of

qubits 2,3 is prepared, without loss of generality, in the Bell state $|\phi^+\rangle_{2,3}$ and qubit 2 is sent to A. The combined state of the three qubits is $|\psi\rangle_{1,2,3} = |\psi\rangle_1 |\phi^+\rangle_{2,3}$. We can write this state in the Bell basis of the combined 1,2 qubits

$$\begin{aligned} |\psi\rangle_{1,2,3} \;=\; & \frac{1}{2}[|\phi^+\rangle_{1,2}(\alpha|0\rangle_3 + \beta|1\rangle_3) \\ & |\phi^-\rangle_{1,2}(\alpha|0\rangle_3 - \beta|1\rangle_3) \\ & |\psi^+\rangle_{1,2}(\beta|0\rangle_3 + \alpha|1\rangle_3) \\ & |\psi^-\rangle_{1,2}(-\beta|0\rangle_3 + \alpha|1\rangle_3)]. \end{aligned} \tag{1.4.3}$$

Now a measurement in the Bell basis can be done in A resulting in a teleportation of state $|\psi_{in}\rangle$ from qubit 1 to qubit 3 (it is important to mention that Bell state measurement is not an easy task and it was proven that a never failing Bell measurement is impossible to employ using only linear elements [112]). If A measures $|\phi^+\rangle$ then the teleported state is exactly $|\psi_{in}\rangle_3$, otherwise it can be produced by some known transformation that is dependent upon A's measurement. In order to produce the requested state, A should send B using a classical channel the result of its measurement. It is important to notice that after the measurement, qubit 1 no longer holds the original state, thus the state was not cloned, but teleported.

An interesting extension of quantum teleportation occurs when dealing with multi-qubit states. If we take two entangled states of two qubits we can swap the entanglement between the two states to create two new entangled states. This procedure is called entanglement swapping [201]. To demonstrate it, we shall take two Bell states $|\psi^-\rangle_{1,2}$ and $|\psi^-\rangle_{3,4}$. Now we can write the four qubit state in the Bell basis of qubits {1,4} and {2,3}

$$|\psi\rangle_{1,2,3,4} = \frac{1}{4}[|\psi^+\rangle_{1,4}|\psi^+\rangle_{2,3} - |\psi^-\rangle_{1,4}|\psi^-\rangle_{2,3} - |\phi^+\rangle_{1,4}|\phi^+\rangle_{2,3} + |\phi^-\rangle_{1,4}|\phi^-\rangle_{2,3}\,. \tag{1.4.4}$$

Hence, upon measuring qubits {2,3} in the Bell basis the other two qubits become en-

tangled with exactly the same state that was measured. Entanglement swapping offers a way of entangling qubits that never interacted with each other, thus demonstrating the non-local nature of quantum mechanics [120]. Entanglement swapping has an important role in quantum communication networks as will be described next.

1.4.2 Quantum repeaters and the DLCZ protocol

Long distance quantum communication is an important necessity for large scale quantum computation as well as for quantum cryptography [20, 128]. Quantum data can be transferred over long distances using optical fibers. Alas even the best fibers up to date have losses, preventing an effective data transfer for more than ∼100 km. Classical communication networks can overcome this problem by using amplifiers along the way. This means of action cannot be used with quantum networks due to the no-cloning theorem [184]. Fortunately, a method based on entanglement swapping that bypasses the cloning problem emerged and referred to as the quantum repeater [22]. The idea is to divide a long distance L to n shorter sections, each of them having an acceptable loss. Using an EPR pair and entanglement swapping an entanglement between two adjacent sections can be achieved. Now it is possible to continue the entanglement swapping until entanglement between both ends is created (see Fig. 1.4.1).

In order for this ideal program to work the loss should be negligible. In practice this is not the case, meaning that the entanglement swapping has a significant chance of failing, consequently ruining the full chain entanglement. A way to overcome this problem is to use quantum memories at the nodes of each section that will hold each successful entanglement until all the chain will be formed [148].

The seminal work of Duan, Lukin, Cirac and Zoller (DLCZ) in 2001 [40] offers a concrete way of implementing quantum repeaters using atomic ensembles. The basic idea behind DLCZ theory is to create entangled pair of photons inside EIT media. The first photon is a Stokes photon emitted during a spontaneous Raman process due to the application of a far detuned laser termed write beam. The Stokes photon is entangled

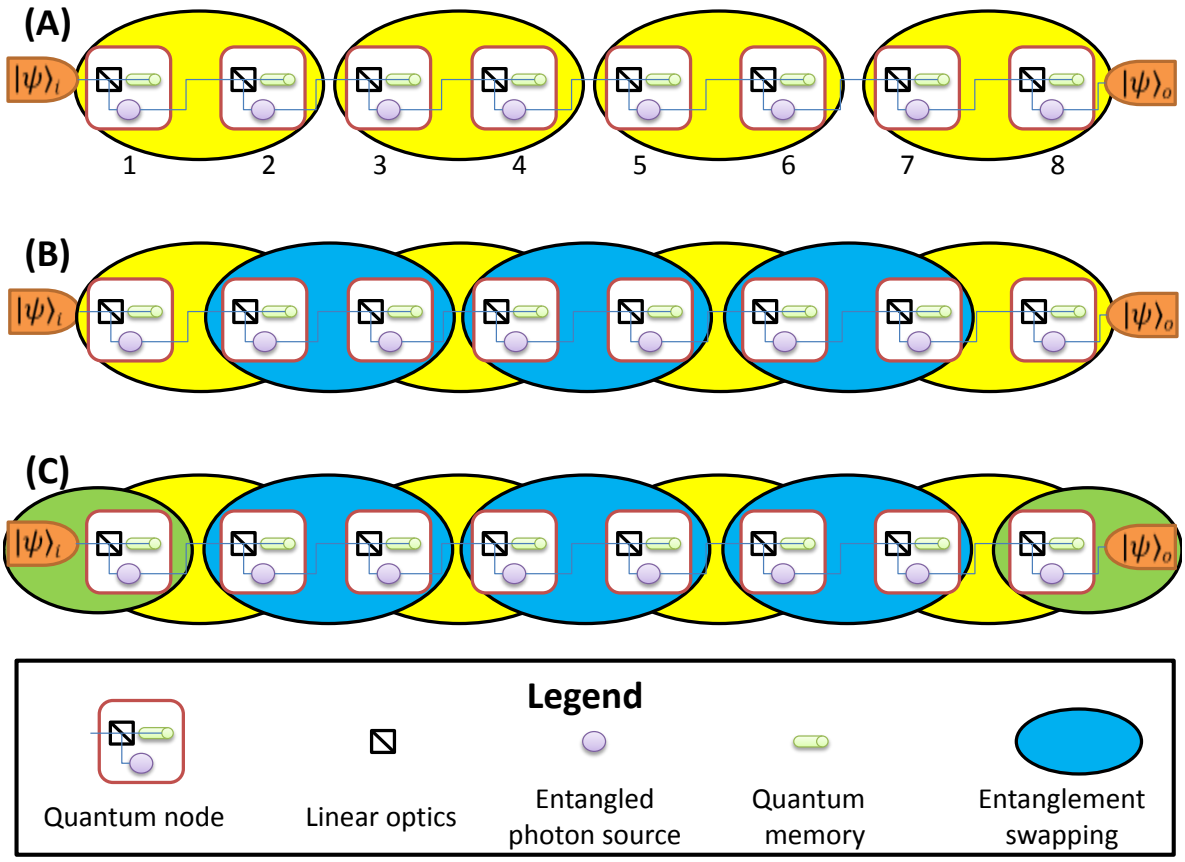

Figure 1.4.1: Quantum repeater network scheme. (A) two adjacent nodes (1-2, 3-4 etc.) are entangled. (B) The entangled sections are growing using entanglement swapping. In this case entanglement swapping of 2-3 creates an entanglement between 1-4 etc.. (C) When all the chain is linked an entanglement between the state to be transferred $|\psi_i\rangle$ and the first node in the chain is created causing a teleportation of the state to the output port.

with all the atoms in the media as there is an equal probability for interaction with every atom. The spin wave function can be written as

$$\frac{1}{\sqrt{N_A}}\sum_{k=1}^{N_A} e^{i(\mathbf{k}_w-\mathbf{k}_S)\mathbf{x}_k}\,|1\rangle_1\,|1\rangle_2\cdots|2\rangle_k\cdots|1\rangle_{N_A}\,, \tag{1.4.5}$$

where N_A is the number of atoms, $\mathbf{k}_w$ is the wavenumber of the write beam, $\mathbf{k}_S$ is the wavenumber of the emitted Stokes photon and $\mathbf{x}_k$ is the place of the specific atom. As the Raman process is spontaneous the Stokes photon can be emitted to any possible mode, thus the specific mode for the quantum process is defined by detection using a

photodetector with an imaging system defining the mode [39].

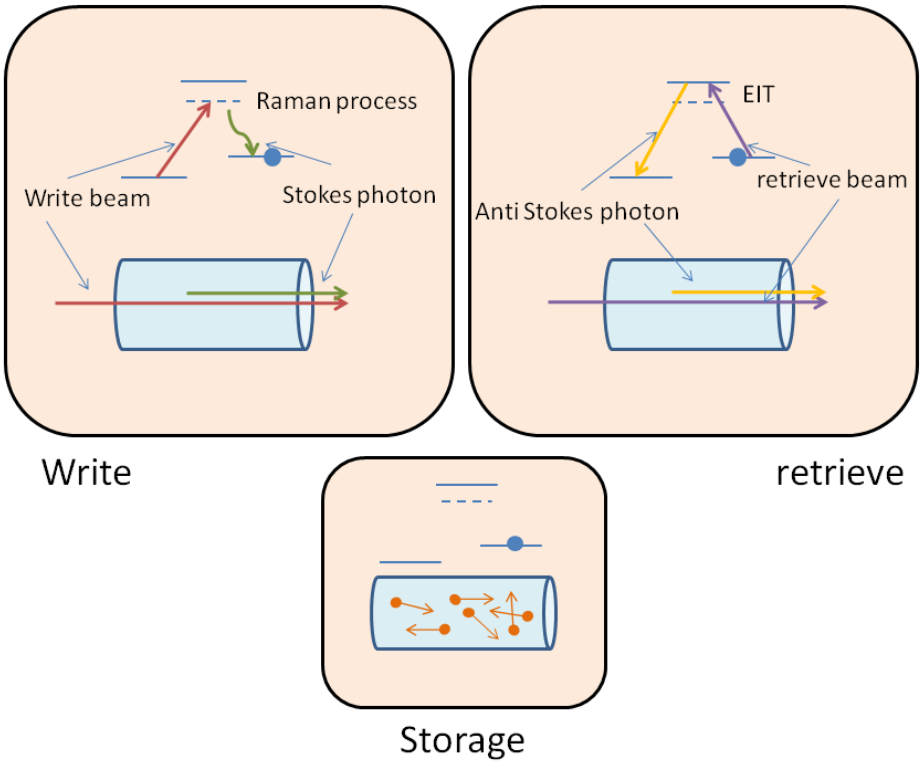

Figure 1.4.2: Heralded storage of a single photon using DLCZ protocol. Schematic picture of the write, storage and retrieve steps of the quantum storage. Two cells can now be entangled by interfering the respective two stokes photons on a beam splitter. This protocol can be repeated many times thus creating viable quantum network.

A detection of the Stokes photon heralds the storage process that follows. As the atomic ground level coherence is long lived it is possible to read out the excited wave-function after a long storage time. Retrieval is done using EIT, meaning a perfect two photon resonance of the lambda system. Applying a nearly resonant read beam induces single photon Anti Stokes (AS) emission. The amplitude of the total process is just

$$\sum_{k=1}^{N_A} e^{i(\mathbf{k}_w-\mathbf{k}_S)\mathbf{x}_k} e^{i(\mathbf{k}_r-\mathbf{k}_{AS})\mathbf{x'}_k}, \tag{1.4.6}$$

where $\mathbf{k}_r$ is the wavenumber of the read out beam, $\mathbf{k}_{AS}$ is the wavenumber of the emitted AS photon and $\mathbf{x'}_k$ is the place of the specific atom in the time of read out. For

a perfect phase matching condition there is a constructive interference, hence a high probability to collect the AS photon in the specific angle related to $\mathbf{k}_{AS}$ (Figure 1.4.2 gives graphic description of the quantum storage process). The next step in the DLCZ protocol is to entangle two or more remote atomic ensembles by combining the single photons emitted on beam splitters, thus enabling long range quantum communication with high fidelity [148].

Quantum effects with few photons were shown recently in many experiments. The most successful experiments were made in ultra cold trapped ensembles such as atom-photon entanglement [31,118], heralded entanglement between distant ensembles [32,99] and entanglement storage of more than 1 ms [194]. Although a more difficult task due to atomic motion, non classical correlations of single photon emission were also shown in hot rubidium vapor [15, 45].

Chapter 2

Materials and Methods

2.1 Lasers

The basic elements in all quantum optics experiments are coherent light sources. In order for an EIT experiment to succeed the coherence time of the laser should be long compared to the excited state lifetime. As such, extremely narrow bandwidth lasers are used in such experiments. We used two kind of lasers, one is External Cavity Diode Laser (ECDL) and the second is Distributed Feedback laser (DFB).

2.1.1 External Cavity Diode Laser

The ECDL is composed of a standard laser diode, a collimation lens and an external grating. The idea is to create an external cavity using the grating such that the first diffraction order returns to the diode. This new cavity is much longer (a few cm) than the original one ($\sim 100\mu m$) thus having a smaller free spectral range. The spectral linewidth of the external cavity mode, $\Delta\nu_{ext}$, is narrower than the laser diode linewidth, $\Delta\nu_{int}$ according to [200]

$$\frac{\Delta\nu_{ext}}{\Delta\nu_{int}} = \frac{1}{\left(1 + {}^{\tau_{ext}}/_{\tau_{int}}\right)^2}, \tag{2.1.1}$$

where τ_{ext}, τ_{int} are the round trip time of the external and internal cavities. This ratio is on the order of $\sim 10^4$, thus for a standard laser diode where the modes bandwidth are $100\,MHz$, the achieved bandwidth of the ECDL can be less than $100\,kHz$. We use in our setup a home built ECDL in a Littrow configuration (Fig. 2.1.1). The laser diode and the lens reside in a special collimation tube (Thorlabs) and the grating is glued to

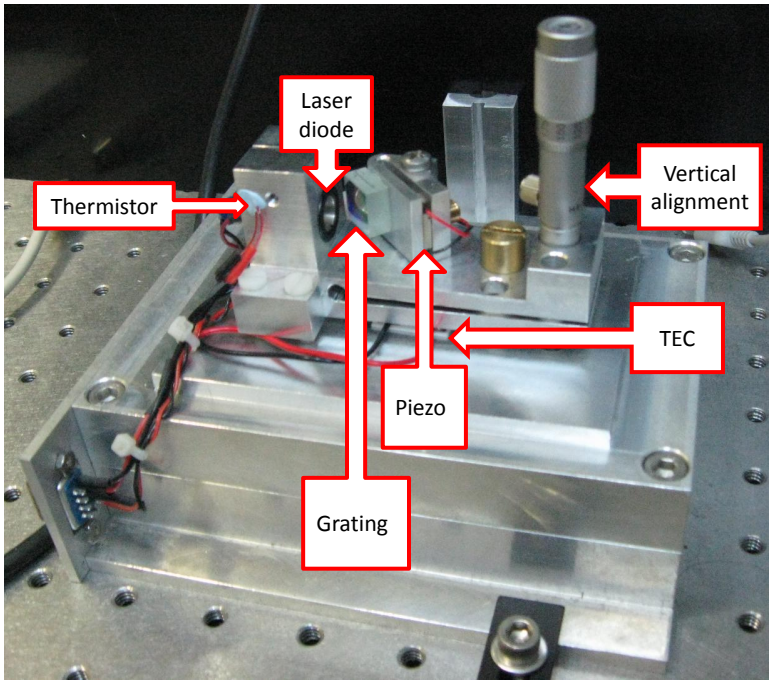

Figure 2.1.1: Our home built ECDL.

a holder that can be rotated coarsely. A more refined scan of the grating is done using a piezoelectric plate. The vertical alignment that control the quality of the external cavity is carried using a micrometer. The whole stage of the ECDL is connected to the ground via Thermo-Electric Cooler (TEC) that allows for temperature stabilization with the temperature being monitored using a thermistor. Using this device we achieve a $\sim 5\,GHz$ mode-hop free scan. Applying a feed forward current loop on the diode can result a much wider mode hop free range [143]. We also use a commercial ECDL with a tapered amplifier (Toptica, TA-100, 780 nm). This laser has a feed forward and can be tuned mode hop free for more than $20\,GHz$.

2.1.2 Distributed Feedback laser

A DFB laser is a more complicated laser diode design where the diode active region is made up of a periodic grating. This causes an effective filtering inside the diode, thus

creating a very narrow bandwidth of a few MHz. We use a commercial DFB laser (Toptical DL-DFB 795 nm). Although the DFB has a broader linewidth than ECDL it is still less than the spontaneous decay ($6\,MHz$ in Rubidium) hence it is suitable for EIT experiments. Moreover, the DFB offers two advantages, one is a very large mode hop free range (hundreds of GHz) and the second is its favorable passive stability over the ECDL.

2.2 Arbitrary phase and amplitude pattern control

One of the main demands for the following research is the ability to create and modulate the spatial shape of the beam. For this control of the phase and amplitude of the beam pattern we use two spatial light modualtors (SLM), a commercial phase SLM as well as a home built amplitude SLM that was devised from a Digital Mirror Display (DMD) projector. In this section I will describe these two devices, but I will begin first by describing Laguerre-Gaussian (LG) beams that are the main building blocks of the patterns used in this research.

2.2.1 Laguerre-Gaussian beams

Laguerre-Gaussian beams are one of several complete sets of paraxial waves, where the spatial part of the electric field can be written as $E(\vec{r}) = A(\vec{r})e^{ikz}$. These solutions are plane waves modulated by a complex slow varying envelope $A(\vec{r})$ that must satisfy the paraxial Helmholtz equation $\nabla_{\perp}^2 A - 2ik\frac{\partial A}{\partial z} = 0$. The Laguerre-Gaussian solution is given by

$$\begin{aligned} A(r,\phi,z) &= \frac{C}{w(z)}\left(\frac{\sqrt{2}r}{w(z)}\right)^{|l|}\exp\left(-\frac{r^2}{w(z)^2}\right)L_p^{|l|}\left(\frac{2r^2}{w(z)^2}\right)\times \\ &\quad \exp\left\{i\left(k\frac{r^2}{2R(z)} - (2p+|l|+1)\zeta(z) + l\phi\right)\right\}, \end{aligned} \tag{2.2.1}$$

where $w(z) = w_0\sqrt{1+\frac{z^2}{z_r^2}}$ is the beam width with w_0 the beam waist and $z_r = \frac{\pi w_0^2}{\lambda}$ the Rayleigh range, $R(z) = \frac{z^2+z_r^2}{z}$ is the radius of curvature of the beam, $\zeta(z) = \arctan(\frac{z}{z_r})$ is the Gouy phase, l is azimuthal index, p is radial index and $L_p^{|l|}$ is the Laguerre polynomial of the specific indices [134]. The main interest in this solution, that differs from the ordinary Gaussian beam, is the appearance of an azimuthal phase $e^{il\phi}$. The wave fronts of the LG beam have a spiral shape, meaning that this azimuthal phase has the role of orbital angular momentum around the $r = 0$ point [6]. This is a quantized angular momentum where the quantization number is l. An important observation

about the LG solution is that at $r = 0$ the amplitude of the electric field is exactly zero as the phase at the center is not defined. Fig.2.2.1 shows the amplitude and phase of LG beams with different l and p indices. Generally speaking, every beam that has the characteristic of zero amplitude singular point due to azimuthal 2π phase shift is called optical vortex. Usually, and in most of the following work, it is hard to produce the exact amplitude of an LG beam, but creating the phase is much easier, thus the singular beams we produce using phase SLM will be termed vortices.

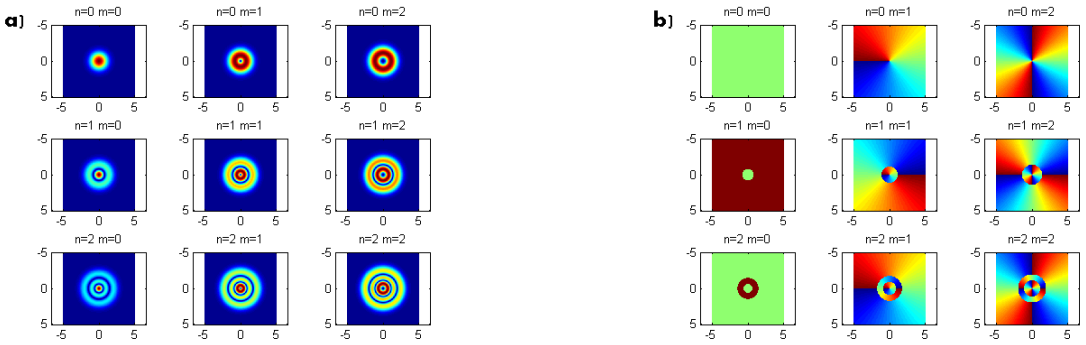

Figure 2.2.1: Some examples for (a) amplitude and (b) phase of LG beam with different azimuthal (m) and radial (n) indices.

2.2.2 phase SLM

The main SLM we use for the experiments is a phase only spatial light modulator based upon twisted nematics liquid crystals (Boulder Nonlinear Systems). This is a reflective SLM meaning it behaves like regular mirror when it is off. The SLM has 512×512 pixels with 8 bit phase resolution that allows almost continuous phase change from 0 to 2π. In Fig. 2.2.3 we present our ability to create arbitrary phase vortex beams and vortex beams matrices. In order to reveal the phase of the beam we interfere the created vortex beam and the original beam using a Michelson interferometer (Fig. 2.2.2). To

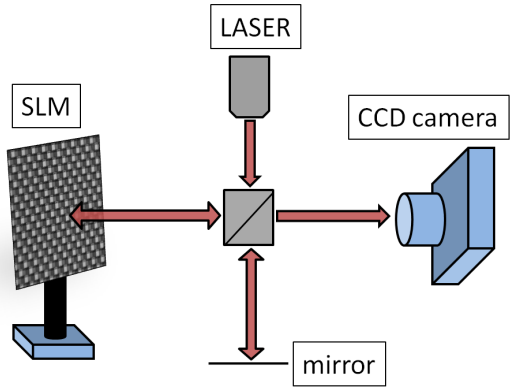

Figure 2.2.2: Michelson interferometer for measuring beam phase.

explain the resulting pattern we take for simplicity a plain wave reference field instead of a Gaussian beam. If the angle between the beams is α, the plain wave field will be given by

$$E_p = E_0 e^{i(k_x x + k_z z)} = E_0 e^{i(\frac{2\pi}{\lambda} r\cos\phi\sin\alpha + k_z z)} \tag{2.2.2}$$

Taking the LG beam at its waist ($z = 0$, $R(z = 0) = 1$) and assuming equal amplitudes, the interference is just

$$\mid E_p + E_{LG} \mid^2 = 2E_0^2(1 + \cos(\Phi_l))$$

where the phase front is

$$\Phi_l(\rho, \varphi) \quad = \quad l\phi - \frac{2\pi}{\lambda} r\cos\phi\sin\alpha. \tag{2.2.3}$$

The generated pattern has interference fringes with a fork-like pattern at the vortex [188].

2.2.3 Pico projector SLM

DLP Pico projector V2 is a development kit DMD projector manufactured by Texas Instruments. DMD technology is based on a grid of micrometer mirrors that can vibrate due to applied voltage. We modified this low cost projector to become a binary

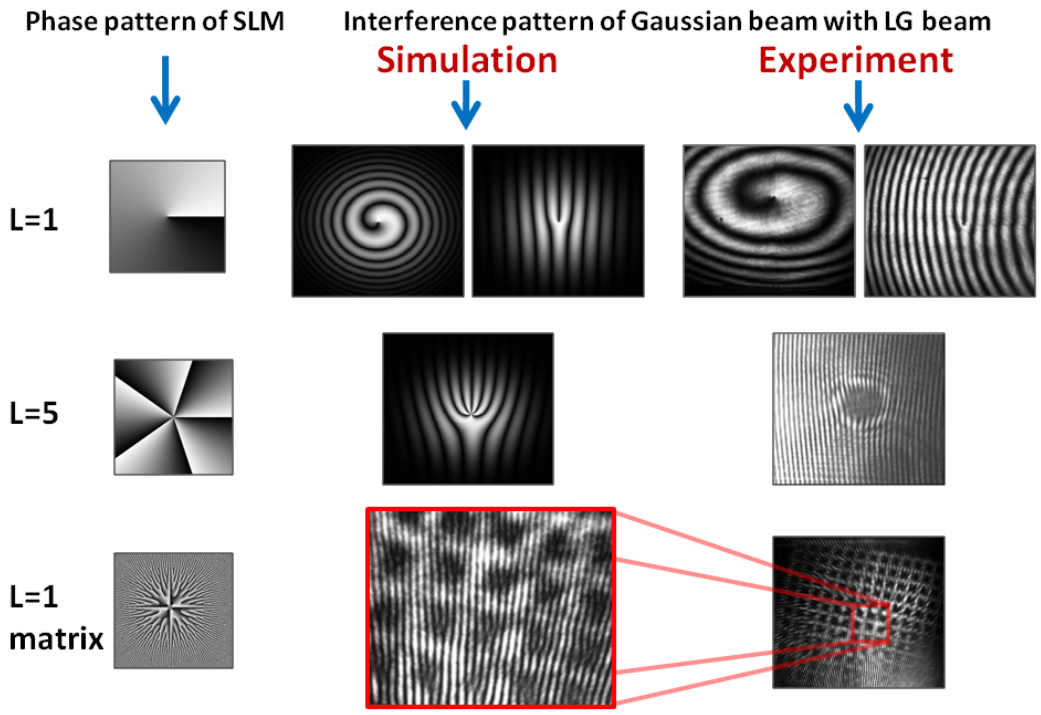

Figure 2.2.3: Optical vortices in free space using a phase SLM. The left column shows the phase pattern imprinted on the SLM. The two other columns present simulation and experimental results for an interference between the optical vortex created using the SLM and pure Gaussian beam. In the case of vortex array it is possible to see free space rotation of the image as explained in section 3.1.2.

amplitude spatial light modulator by removing the LEDs and optical projecting elements [77]. Figure 2.2.4 shows a picture of the pico projector SLM. Using this SLM we were able to achieve an amplitude and phase modulation, thus creating true LG beams [102].

The DMD we use consists of 480x320 micromirrors, each 7.6x7.6 microns in size. Each mirror corresponds to a certain pixel and it is held in either of two angular positions: $+12^o$ (On, or "white" state) and -12^o (Off, or "black") state. The DMD serves as a programmable spatial filter since the light reflected from and diffracted by the mirrors corresponding to the black pixels is filtered out. The maximal efficiency of a gray amplitude hologram is known to be $\frac{1}{16} = 6.25\%$, while for binary amplitude it can reach

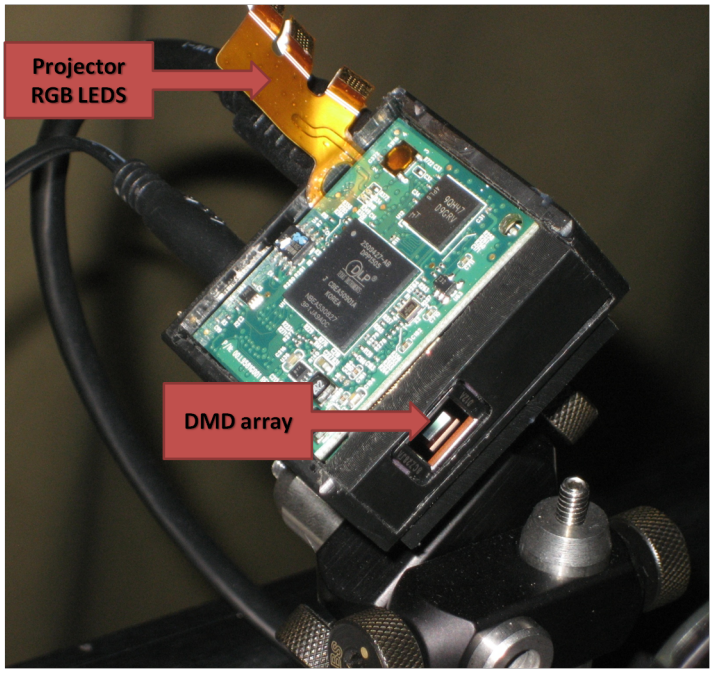

Figure 2.2.4: Our DMD SLM.

$\frac{1}{\pi^2} \sim 10.1\%$ [110]. The DMD array itself behaves actually as a grating, meaning that the pattern effectively consists of two gratings: the micromirrors' substrate grating-like structure and the information grating. When all pixels are on, at a particular angle, we concentrate more than 88% [42] of the diffracted light into a single order. We measure an additional loss of about 40% of the total power of the incident beam mostly due to the fill factor. After applying the information grating between 1% and 5% of the incident beam intensity is concentrated in an output beam.

The way to use the DMD, which is an amplitude modulator, as a phase modulator is by holography. The idea is to print on the DMD a picture of the interference pattern of a Gaussian beam and a vortex beam [9, 142]. The resulting pattern is a fork-like as demonstrated in Fig. 2.2.5(c). Applying this fork-like pattern onto the DMD will result two optical vortices with orbital angular momentum $\pm l$.

The fork-like patterns are used to create vortices with no direct control of the amplitude. We add the amplitude by taking the real part of Eq. 2.2.1 (see for example, Fig. 2.2.5(b)). We then multiply the fork-like pattern by the amplitude distribution

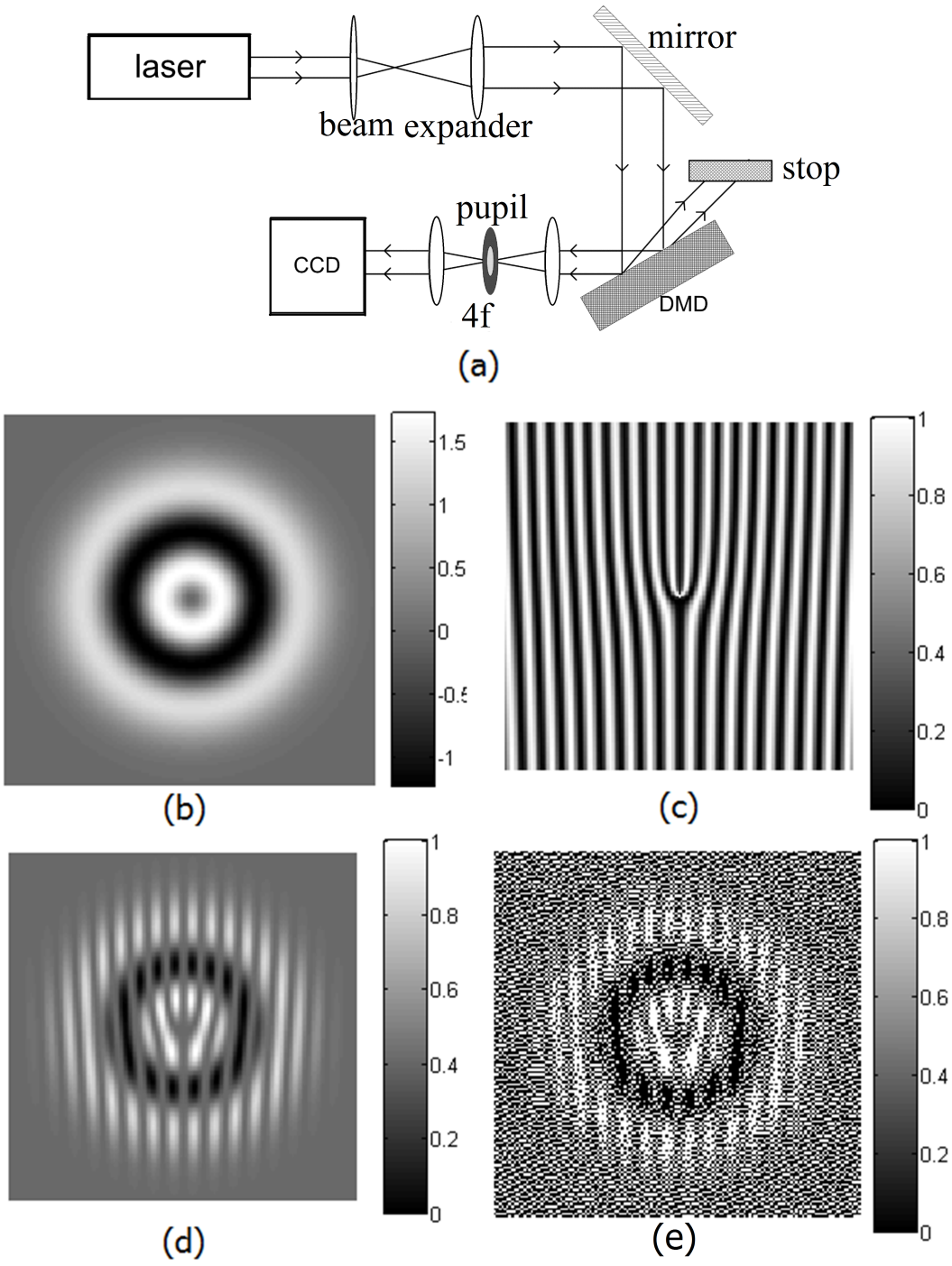

Figure 2.2.5: (a) The optical setup. (b)-(e) Shaping amplitude and phase of LG_2^2 mode (all patterns are 240x240 pixels, corresponding to 1.8x1.8 mm): (b) ideal amplitude; (c) fork-like hologram for $l = 2$; (d) normalized multiplication of (b) by (c); (e) dithered pattern loaded on the DMD. The background corresponds to half filling to allow for negative amplitude of alternate rings in the LG pattern.

and receive a pattern such as Fig. 2.2.5(d). This pattern is gray scaled due to the amplitude pattern. In order to create this kind of pattern using a binary DMD we use dithering. Figure 2.2.5(e) presents the final pattern that is applied to the DMD.

Previous works [119] have shown that the purity of the LG modes was significantly affected by the ratio of the normalization radius of the hologram and the input Gaussian beam. Even at the optimal value of this ratio, the purity of the LG modes with $p > 1$ was low when the amplitude-only hologram was applied to a Gaussian beam [9]. We optimize the purity of the output beams by changing the applied pattern:

$$\left| u_p^{l\,corr}\left(r,\phi,z=0\right)\right| = \left(\frac{\sqrt{2}r}{w}\right)^l L_p^l\left(\frac{2r^2}{w^2}\right)\exp\left(-p_0\cdot\frac{r^2}{w^2}\right)\ , \tag{2.2.4}$$

where $p_0 = \frac{w^2}{w_{env}^2} = 1 - \frac{w^2}{w_i^2}$ is a correction parameter, w_i is the width of the incident Gaussian beam,w_{env} is the corrected width of the Gaussian envelope of the pattern and w is the desired width of the shaped LG mode. The correction parameter can be calculated from measurements and substituted back to Eq. 2.2.4, but it should be fine-tuned empirically.

In order to obtain a desired pattern at the imaging plane, the first order beam is transferred and other diffraction beams are filtered out by the pupil (Fig. 2.2.5(a)). In our experiments 40 cm away from the DMD the beams are well separated. However, in order to reproduce the near field, we use the imaging system. Figure 2.2.6(a) shows the far field intensities of several generated LG beams. A more quantitative analysis can be deduced from Fig. 2.2.6(b) where cross sections of these intensity patterns are presented along with ideal LG beams intensity profiles. The experimental results fit almost perfectly the ideal intensity profiles and the on:off ratio (intensity at the origin divided by maximal intensity) varies between 1:100 and 1:1000.

Figure 2.2.7 show the measured far field interference between the LG beam and an off axis Gaussian beam. This interference exhibiting a fork-like shape confirming the helical phase front of the created LG beam.

It is important to mention that although similar results were measured using liquid

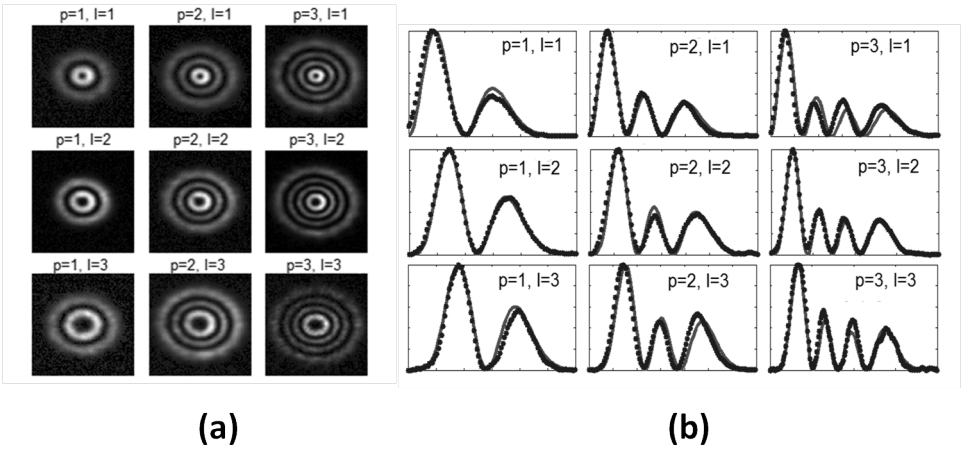

Figure 2.2.6: (a) Intensities in far field. Radius of the outer ring of LG_3^3 beam is 700μm. (b) Radial profiles of intensity obtained from cross sections of (a) (dotted) vs. ideal LG intensity profiles (solid).

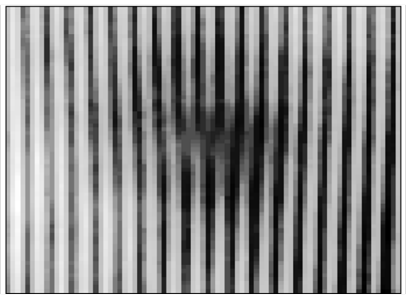

Figure 2.2.7: Interference of an LG_0^1 beam with an off-axis Gaussian beam in far field. Physical height: 100μm.

crystal SLM [119], DMD technology is far superior to liquid crystal in the area of fast modulation, reaching rates of tens of kHz comparing to only about 100 Hz. We work at video rate since our goal was a proof-of-concept, but other control platforms, with higher bandwidth are available.

2.3 Temporal shaping and control

Another important part of an EIT setup in general and specifically in this research is the temporal control and shaping of the pulses and subsequently also the spectral shaping. Here I will introduce the optical tools which allows for this control. The first two sections will explain the modulators used in the research. The last section will deal with the RF and microwave control.

2.3.1 Electro-optic modulator

Electro-optic modulators (EOM) are ubiquitous devices for amplitude and phase modulations. The physical idea behind it is the Pockels effect, describing a change in the refractive index linearly proportional to the electric field. This effect can be found in crystals that lack inversion symmetry [146]. Mathematically, the index of refraction can be written as

$$n(E) \approx n_0 - \frac{1}{2} r n_0^3 E, \tag{2.3.1}$$

where E is the applied electric field and r is the Pockels coefficient which has a typical values of $10^{-12} - 10^{-10}$ m/V. An EOM where the voltage is applied parallel to the direction of light is called longitudinal EOM and when the voltage is applied perpendicular to the direction of light propagation the modulator is called transverse EOM. We use in our setup only transverse EOMs. The differentiation between amplitude and phase EOM can be done on the basis of light polarization with respect to the principal axis of the crystal. In phase EOM the polarization of light is parallel to the principal axis, hence applying an electric field contributes only to additional phase. An amplitude EOM requires polarization that mixes the principal axes, thus creating a controlled birefringence. In order to avoid uncontrolled overall noise (mostly due to temperature variations) using amplitude EOM usually two crystals with the principal axes at right angles one to the other are combined.

We use free space phase modulators. Light going through a crystal of length l

undergoes a phase shift $\varphi = 2\pi n(E)l/\lambda$. Using Eq. 2.3.1 we get

$$\varphi = \frac{2\pi n_0 l}{\lambda} - \frac{\pi r n_0^3 E l}{\lambda}. \tag{2.3.2}$$

For a rectangular crystal with a distance d between the facets, the electric field is $E = V/d$ with V being the applied voltage. The phase in this case can be written as [146]

$$\varphi = \varphi_0 - \pi \frac{V}{V_\pi}, \tag{2.3.3}$$

where $\varphi_0 = {}^{2\pi n_0 l}/_{\lambda}$ and $V_\pi = {}^{d\lambda}/_{l r n^3}$ is the voltage causing a half wave phase shift.

Low frequency devices require only a crystal and two plates with a voltage source - this EOM has a broadband response. For higher frequencies (above 100 MHz) the voltage needed for substantial phase shift ($V_\pi \sim 100 - 200$ Volt) requires large and expensive drivers, thus a resonant EOM can be used. The idea behind the resonant EOM is to couple the microwave field efficiently using a cavity, thus lowering the external drive immensely for a certain V_π. We can treat the system as a RLC lumped element circuit with the crystal being the capacitor, having also a parasitic resistance and an effective inductance is added through the cavity. The resonance of the cavity ${}^{1}/_{\sqrt{LC}} = \omega_0$ should be the required frequency. The bandwidth at which modulation can be used, $\Delta\omega$, is dependent upon the Q- factor of the system, $Q = {}^{\omega_0}/_{\Delta\omega}$. The acquired phase shift due to resonant EOM is [189]

$$\Delta\varphi = \frac{\pi r n^3}{\lambda}\sqrt{\frac{2PQl}{\epsilon\omega_0 b d}} \tag{2.3.4}$$

where P is the microwave power, Q is the quality factor of the cavity, ω is the resonance frequency, b is the width of the crystal and ϵ is the dielectric constant of the crystal at frequency ω_0.

In this research three EOM modules were used. Two commercial EOMs, a broadband low frequency EOM (Thorlabs) and a 6.8 GHz resonant EOM (NewFocus). The

third EOM is a home-build one. This is a resonant EOM with a broadband tuning range based on a tunable split-ring resonator devised by Shiozaki et al [154]. Our EOM, which is schematically presented in Fig. 2.3.1, is based on a rectangular microwave cavity that is made of two plates and two spacers. The crystal inside splits this cavity to an effective two split-ring cavities. Each cavity size can vary with a spacer movement. The resonance frequency of a split-ring resonator can be calculated as a lumped LC resonator where the capacitance is $C_{eff} = \epsilon bl/d$ and the inductance is $L = \mu_0 hd/l$ with h being the length of the ring resonator [87, 154]. The resonance frequency of the total device can be calculated approximately by combining the inductance of the two resonators, $\frac{1}{L_{eff}} = \frac{1}{L_1} + \frac{1}{L_2} = \frac{l}{\mu_0 d}\left(\frac{1}{h_1} + \frac{1}{h_2}\right)$, thus

$$f_0 = \frac{1}{2\pi\sqrt{LC}} = \frac{c}{2\pi\sqrt{\epsilon_r b h_1 h_2 / h_1 + h_2}} \tag{2.3.5}$$

where $\epsilon_r = \epsilon/\epsilon_0$ is the relative permittivity. It is apparent that when $h_1 \gg h_2$ the resonance frequency is $f_0 \approx \frac{c}{2\pi\sqrt{\epsilon_r b h_2}}$, hence the smallest h_2 will determine the highest resonance frequency. On the other hand, when $h_1 = h_2 = h$ the frequency will be $f_0 = \frac{c}{2\pi\sqrt{\epsilon_r b h/2}}$.

We used in our setup a $LiTaO_3$ crystal with size (in mm) $l \times b \times d = 40 \times 3 \times 3$. The index of refraction of the crystal is $n = 2.2$ and $\epsilon_r = 43$. In order to couple the microwave to the cavity via SMA a small antenna parallel to the optical axis is used. The length of the antenna and its distance from the crystal and the metal walls will determine the coupling strength. We managed to create a cavity with critical coupling having a Q factor of $30 - 70$ depending on the frequency as can be seen in Fig. 2.3.2.

The basic application of high frequency phase modulation is creating sidebands. Assuming a sinusoidal modulation $V = V_M \sin \omega_M t$ the field that will emerge out of the EOM according to Eq. 2.3.3, while dropping the constant phase part, is [189]

$$E_{out} = Aexp\left(i\omega t - i\pi \frac{V_M}{V_\pi} \sin \omega_M t\right) = Aexp\left(i\omega t - iM \sin \omega_M t\right), \tag{2.3.6}$$

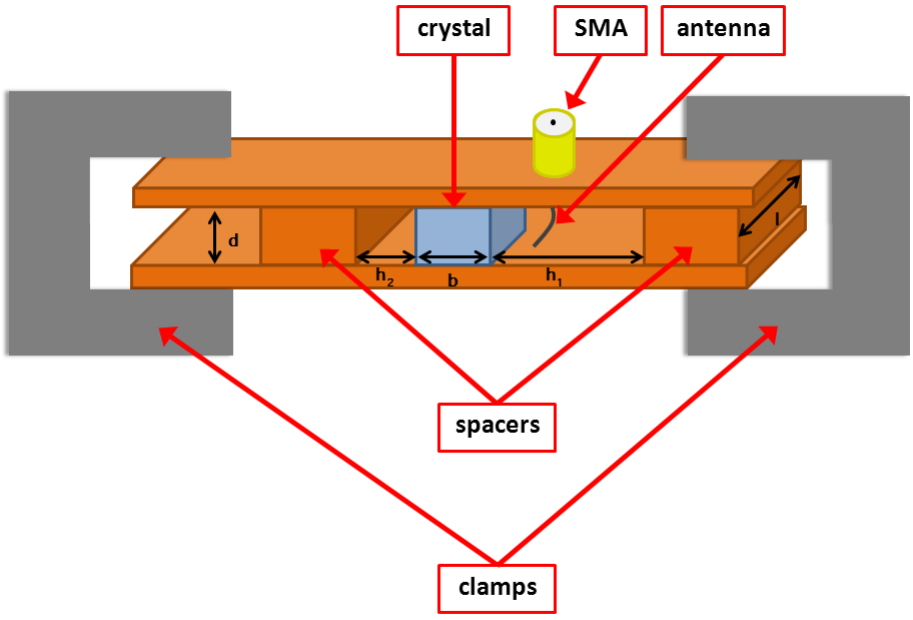

Figure 2.3.1: EOM sketch.

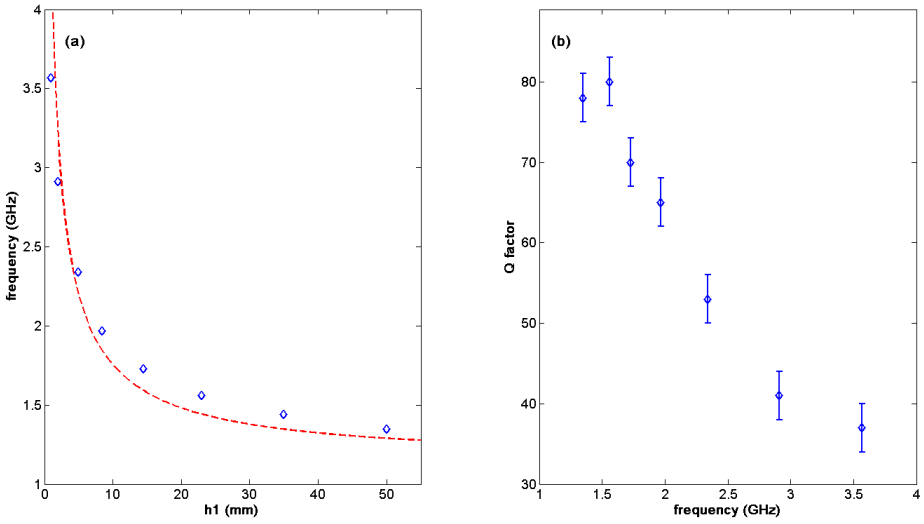

Figure 2.3.2: Electrical measurements of our resonant EOM. (a) Measured and calculated resonance frequency of the EOM as a function of ring resonator length. (b) Measured Q-factor as a function of the resonance frequency.

where $M = \pi \frac{V_M}{V_\pi}$ is called the modulation index. The phase modulation part can also be written as a series of Bessel functions

$$E_{out} = A \sum_{n=-\infty}^{\infty} J_n(M) e^{i(\omega - \omega_M)t}. \tag{2.3.7}$$

Mathematically, the maximum achievable intensity of the first sideband occurs at $M = 1.84$ where $[J_1(1.84)]^2 \approx 34\%$. In order to measure the modulation index we built a standard amplitude modulation setup where the EOM lies between two cross polarizers. A quarter wave plate is also added in order to work in the 50% transmission point where the modulation is maximal [146]. The transmission in this case is $T = \frac{1}{2}(1 - \cos(\frac{\pi}{2} + M \sin \omega_M t))$. For small modulation index ($M \ll 1$) the transmission is just $T = \frac{1}{2} + \frac{M}{2} \sin \omega_M t$. Fast detector and spectrum analyzer is used in order to measure the modulation power with respect to the DC optical power after the modulation. Figure 2.3.3 shows the modulation efficiency of our EOM. The amplitude modulation efficiency is presented in Fig. 2.3.3(a). The theoretical model takes into account $M = \Delta\varphi$ with a phase change calculated from Eq. 2.3.4. Two different crystals were used, x-cut $LiTaO_3$ and z-cut $LiNbO_3$. Figure 2.3.3(b) shows the phase modulation efficiency for the same crystals. The theoretical model calculates $J_1(\Delta\varphi)$ with the phase change computed from Eq. 2.3.4. The experimental results were measured using a frequency sweep of the laser and an etalon. Both amplitude and phase modulation show good agreement between theory and experimental results.

2.3.2 Acousto-optic modulator

Another kind of modulator that was used in this research is acousto-optic modulator (AOM). The basic idea behind AOM is creating a variable index of refraction inside a crystal using acoustic waves. The acoustic wave creates a change in the density, thus creating a perturbed time-varying inhomogeneous medium [146]. The modulator is composed of a crystal and a piezo transducer that creates a traveling sound wave inside

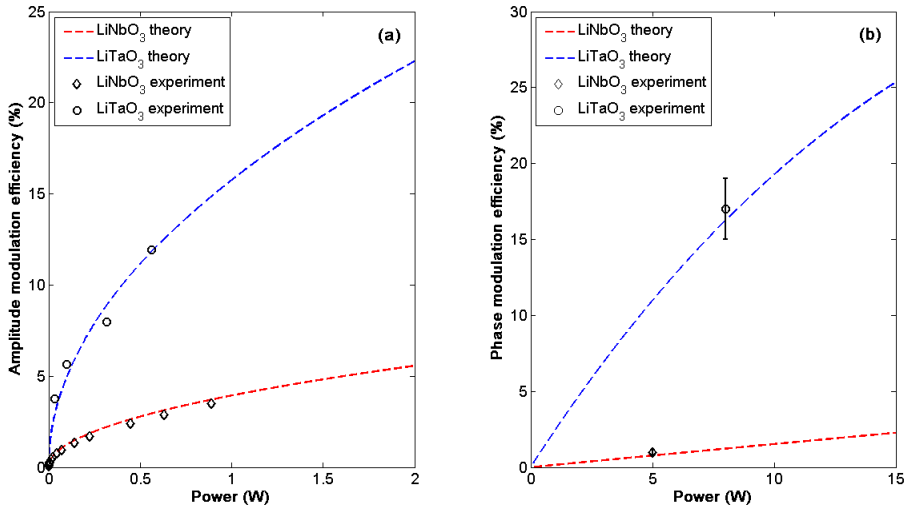

Figure 2.3.3: EOM modulation efficiency for $LiNbO_3$ and $LiTaO_3$. (a) Amplitude modulation efficiency and (b) phase modulation efficiency.

the crystal. During the time the light goes through the crystal the sound wave can be regarded as frozen, thus the medium can be thought of as a thick Bragg grating. The diffracted angle will be

$$\sin\theta = \frac{\lambda}{2\Lambda} \tag{2.3.8}$$

where λ is the laser wavelength and $\Lambda = v_s/f$ is the sound wavelength with v_s the speed of sound in the crystal and f the applied frequency. The diffracted beam has also a temporal phase shift that results a shift of the frequency by f. This can be understood as a Doppler shift of the light due to the moving sound wave.

We use the AOM for two main applications. One is amplitude modulation of the signal. The idea is to use the fact that the diffracted light intensity is linearly proportional to the sound wave intensity [146]. The second application is frequency and phase modulation. It is important to notice that using a different frequency also shifts the diffracted angle. In order to avoid this effect a setup of double pass through the AOM is used in all cases where frequency modulation of frequency scan is applied [37]. The available modulation bandwidth B, where $f = f_0 \pm B$, is inversely proportional to the

size of the beam D

$$B = \frac{v_s}{D} \tag{2.3.9}$$

thus for modulation purposes the size of the beam should be small. Another important temporal issue arises when using the AOM as a fast switch. In this case the Switching RF signal from the piezo is moving with a speed $v_s \sim 3000\, m/s$ towards the optical beam. Usually the beam is situated a few millimeters from the piezo, thus a lag time of few μs should be taken into consideration.

2.3.3 Waveform generation

The modulators described above use RF or microwave sources in order to operate. The resonant EOM used for sideband generation are usually in the microwave regime. We use commercial signal generators (up to 25 dBm) that are amplified up to 35-40 dBm in order to get substantial power in the first sideband. The AOM we use work typically around 80 MHz with 15 MHz bandwidth. In order to modulate the amplitude and phase of the AOMs we use an arbitrary waveform generator (Active Technologies AWG4000). This AWG has a 250M Sample/sec and 2M points memory allowing for creating the 80 MHz needed for the AOM and an arbitrary signal for 8 ms. The control over the AWG as part of the whole control setup is done using a LabView program.

2.4 Atomic media

In this research the main quantum tool is the atomic media. All the research presented in this thesis is done using rubidium atomic vapor, with the exception of Appendix 5.1, where EIT in neon gas is reported. In this section I will briefly present the relevant rubidium spectrum and describe how we lock our lasers to the relevant lines.

2.4.1 Rubidium spectral lines

Rubidium is an alkali metal that is well documented and is widely used in atomic optics and quantum optics research. Figure 2.4.1 shows rubidium D1 $\left(5^2S_{1/2} \rightarrow 5^2P_{1/2}\right)$ and D2 $\left(5^2S_{1/2} \rightarrow 5^2P_{3/2}\right)$ lines and its hyperfine structure for ^{85}Rb and ^{87}Rb isotopes (Natural abundance is 72% and 28% respectively) [164, 165]. The optical frequencies of the D1 and D2 lines are 795 nm and 780 nm respectively. Due to isotope shifts there is an ∼80 MHz difference between the two isotopes frequencies.

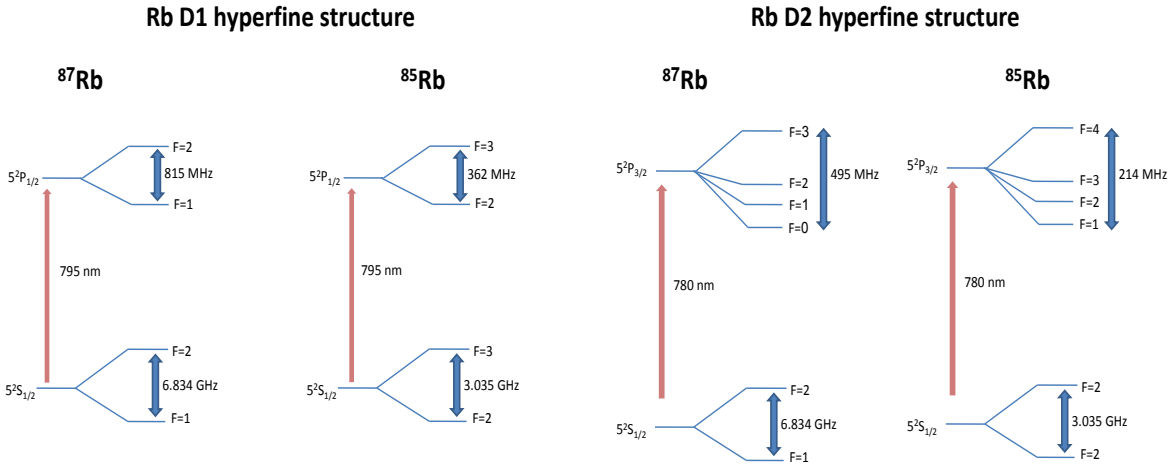

Figure 2.4.1: Rubidium hyperfine levels diagram.

Atomic motion causes every level to be Doppler broadened. This broadening is

typically Gaussian [146]

$$g(\nu) = \frac{1}{\sqrt{2\pi\sigma_D^2}} \exp\left[-\frac{(\nu-\nu_0)^2}{2\sigma_D^2}\right] \tag{2.4.1}$$

with a characteristic width

$$\sigma_D = \frac{1}{\lambda}\sqrt{\frac{k_b T}{M}}, \tag{2.4.2}$$

where M is the mass of the rubidium isotope and T is the temperature. For room temperature the FWHM of the Doppler peak is $\Delta\nu_D = 2.35\sigma_D \sim 500$ MHz. Levels that are closer in frequency than the Doppler width will not be resolved. For vapor cells that contain also buffer gas another effect on the linewidth is pressure broadening. This is a homogenous broadening with a Lorentzian lineshape that is determined by the collisions rate. The combination of a Gaussian Doppler broadening and a Lorentzian pressure broadening is called a Voigt profile. A good approximation of the FWHM of the Voigt profile is given by the following empirical formula [131]

$$\Delta\nu_V^2 = 0.535\Delta\nu_L + \sqrt{0.217\Delta\nu_L^2 + \Delta\nu_D^2} \tag{2.4.3}$$

with $\Delta\nu_V$ the Voight FWHM and $\Delta\nu_L$ the Lorentzian FWHM. Figure 2.4.2 shows the spectrum of rubidium cell with isotopically pure ^{87}Rb and 20 Torr neon buffer gas. The red line is a fit of four shifted Gaussian peaks. The average width is $\Delta\nu_V = 606 \pm 20$ MHz. Using Eq. 2.4.3 with the numbers measured for $\Delta\nu_V$ and calculated for $\Delta\nu_D$ it is possible to calculate the homogenous linewidth to be $\Delta\nu_L = 184 \pm 6$ MHz. The broadening is linear with the pressure [48] hence we measure approximately 9 MHz/Torr, similarly to other reported results [48, 156].

A Doppler free spectrum can be measured using saturation absorption spectroscopy [35]. The basic idea behind this spectroscopy is to use a pump-probe setup where a strong pump is saturating the atomic transition creating a hole in the absorption spectrum for the probe. When the pump and the probe are counter-propagating the

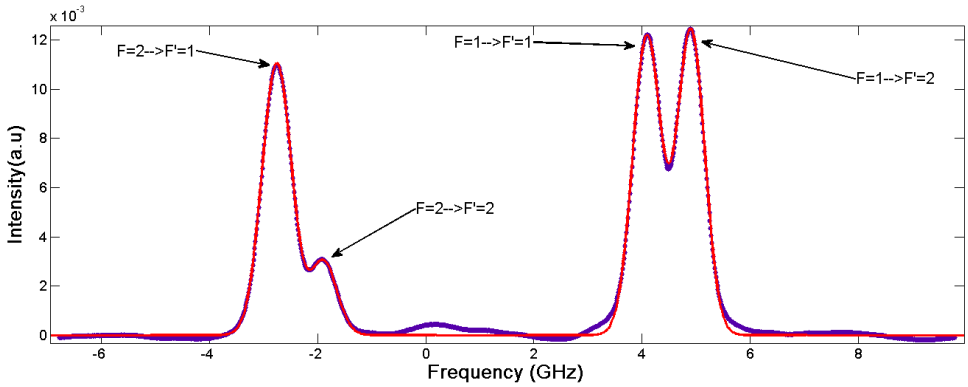

Figure 2.4.2: ^{87}Rb spectrum at room temperature (25°C) with a fit to four shifted Gaussian peaks.

hole burning of the pump and the frequency of the probe are equal only for atoms at rest, thus the saturation effect is Doppler free (the optical setup is depicted in Fig. 2.4.4(a)). If the spacing between two atomic transitions is narrower than the Doppler broadening, a third Doppler free resonance, called crossover, will be visible at the central frequency between the two atomic resonances. The crossover resonance occurs since in this frequency atoms of the same velocity class is resonant with both pump and probe beams each one on a different transition [35]. In Fig. 2.4.3 we show the D1 spectral lines of natural abundance rubidium as measured using a saturation absorption configuration. The green line is the Doppler broadened spectrum while the red line is the Doppler free spectrum where the narrow peaks of the homogenous linewidth can be observed.

2.4.2 Stabilization

One of the basic properties of our experimental setup is the ability to lock the laser to a specified frequency of the rubidium transition lines. The basic idea of laser locking is a PID control over the laser parameters (current, piezo and temperature) in order to stabilize the laser to a certain Doppler free feature. In our setup we stabilize the temperature to be constant using a designated PID locking system. The frequency control is done with the piezo. Using the Doppler free signal we can determine an amplitude

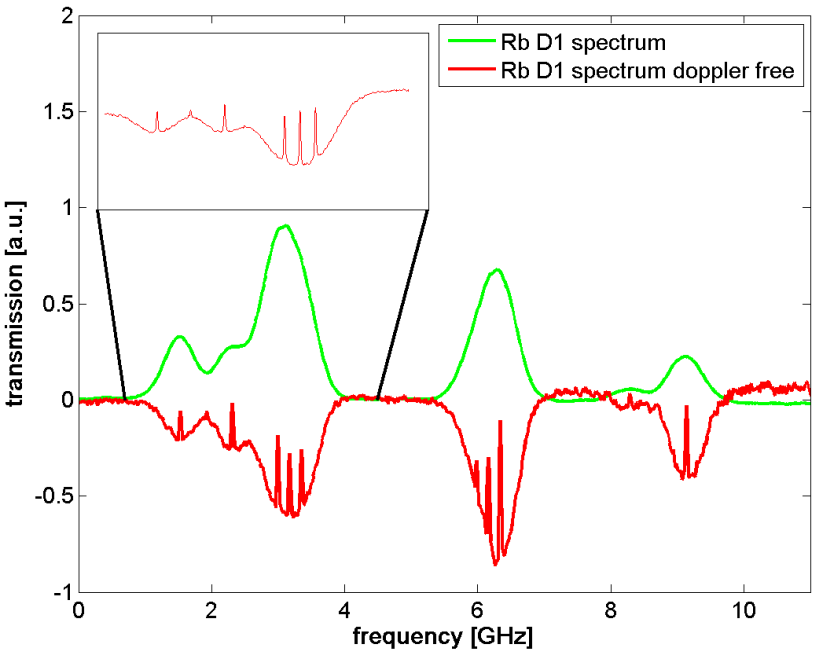

Figure 2.4.3: Rubidium D1 spectral lines. (Green) Doppler broadened spectrum. (Red) Doppler free spectrum. on lines. Inset - a better resolution scan of the F=2→F'=1,2 of ^{87}Rb and F=3→F'=2,3 of ^{85}Rb.

setpoint and lock on the side of the fringe. In order to lock exactly on the top of the fringe we employ a polarization absorption setup [35,137] that allows for dispersive lines without modulating the laser. Figure 2.4.4(b) shows the polarization absorption optical setup. The circular polarization of the pump beam creates different susceptibility for the two linear probe polarizations. Thus when measuring the saturation spectroscopy of both polarizations using a PBS and two detectors and subtracting between them, a dispersive line is achieved. A magnet is used in order to amplify the dispersive signal.

The PID control and the locking mechanism is implemented digitally using an FPGA card (NI-PXI-7833) and LabView software.

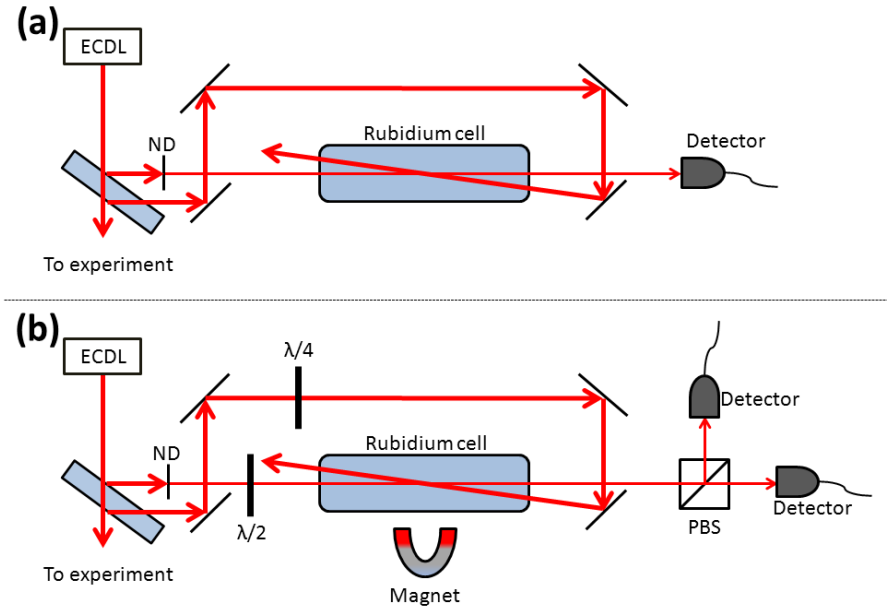

Figure 2.4.4: Doppler free setups. (a) saturation absorption and (b) polarization absorption. ND- variable neutral density filter. PBS - polarization beam splitter.

2.5 EIT setup and results

Here I describe our setup for measuring EIT. This setup is the core of most setups that will be presented in the results section. I also show some benchmark results of our system. It is important to mention that the setup and results described here use the hyperfine levels of the D1 transition of rubidium. In App. 5.1 I will describe EIT results that were taken using Zeeman levels in metastable neon.

2.5.1 Basic EIT setup

The basic tool for this research is an EIT setup. Illustrative representation of the setup is depicted in figure 2.5.1. As an EIT media we use rubidium atoms. We work on the D1 line $\left(5^2S_{1/2} \rightarrow 5^2P_{1/2}\right)$ of ^{87}Rb isotope, so our hyperfine EIT lines are $F = 2 \rightarrow F' = 2$ (Pump) and $F = 1 \rightarrow F' = 2$ (probe).

For the optical transition (795 nm) we use a DFB (DL-DFB, Toptica) having an

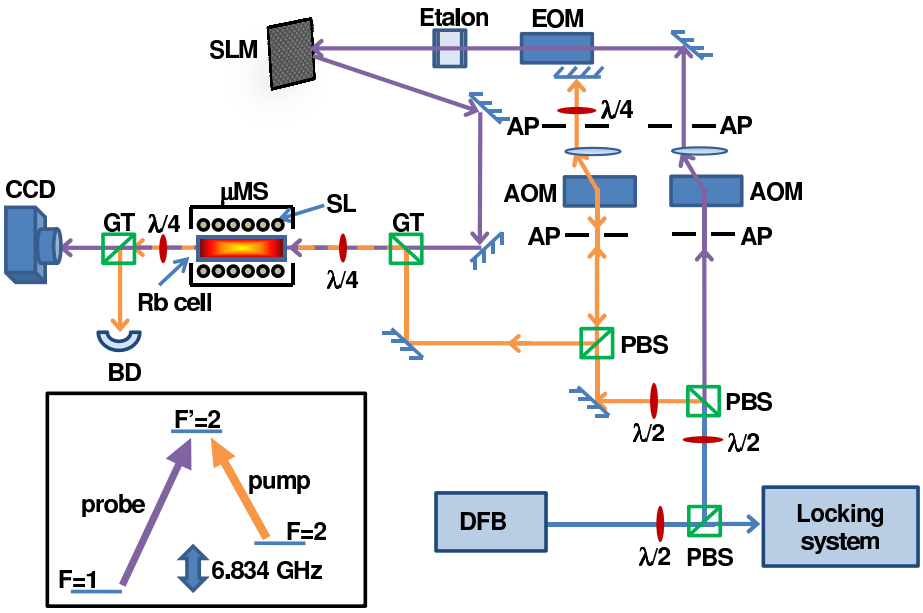

Figure 2.5.1: EIT experimental setup. Orange lines - pump beam, purple lines - probe beam. DFB - distributed feedback laser, PBS - polarizing beam splitter, $\lambda/2, \lambda/4$ - waveplates, AP - aperture, GT - Glan-Taylor polarizer, SL - solenoid, SLM - spatial light modulator, AOM - acousto-optic modulator, EOM - electro-optic modulator, BD - beam dump, μMS-μ-metal shield. The beam is measured using a CCD or amplified photodiode. In the inset - the relevant ^{87}Rb hyperfine level diagram.

output power of 60 mW or ECDL with 120 mW. Our laser is locked to one of the rubidium transitions (typically $F = 2 \rightarrow F^{'} = 2$) using a saturation absorption scheme (COSY, Toptica) or polarization absorption scheme with electronic PID locking mechanism (Digilock, Toptica or home-built LabView software). For our experiments we use standard vacuum cells with dimensions of 7.5 cm long and 2.5 cm in diameter. The cells are filled with rubidium having a temperature dependent vapor pressure spanning from $\sim 10^{-7}$ torr at room temperature to $\sim 10^{-4}$ torr at $100°C$, thus atomic density can be varied by three orders of magnitude [165]. The Rb isotopic fraction is the natural abundance (28% ^{87}Rb and 72% ^{85}Rb) or isotopically pure ^{87}Rb. We have also cells with buffer gas, typically nitrogen or neon with pressures of $3 - 20\, torr$.

In order to create two different coherent laser fields we split the laser power into two lines with different polarizations using polarization beam splitter (PBS). The respective

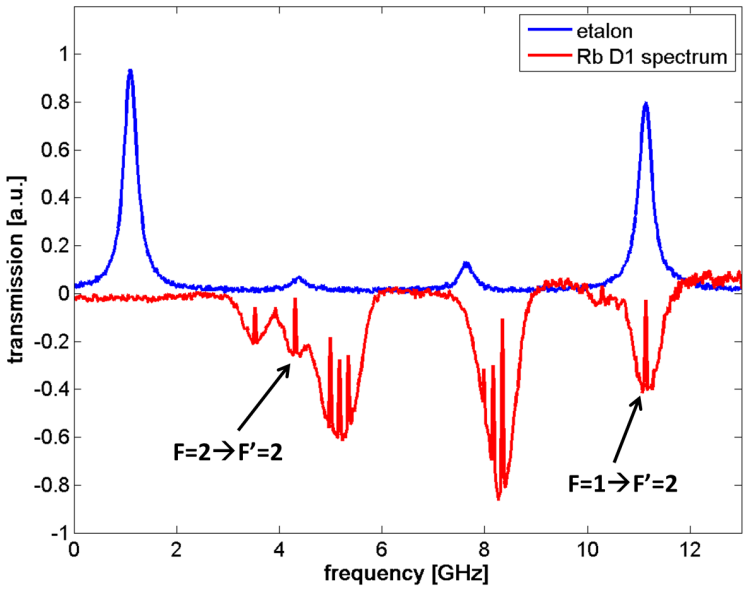

Figure 2.5.2: Etalon transmission spectrum. The etalon transmission is located on the F=1→F'=2 transition (probe), while the laser is locked to the F=2→F'=2 transition (pump). Etalon parameters - FSR - 10 GHz and the finesse is $\sim$ 30. The small peaks shown in the scan are the sidebands of the EOM. This is the way to measure the EOM efficiency.

powers are determined by a $\frac{\lambda}{2}$ waveplate. Each laser line passes through an AOM, the probe in a single pass configuration and the pump in a double pass configuration. The AOM objectives are twofold, one is to change the frequency of the field in order to achieve the desirable detuning and the other is to modulate the amplitude of the beam. For the hyperfine splitting EIT we apply an EOM with a cavity resonant to $\sim$6.8 GHz (New-Focus) matching the ^{87}Rb lower level hyperfine splitting. The EOM is driven by a microwave generator (Anritsu) with power of 15 dBm which is amplified to 34 dBm in order to reach the suitable sideband modulation depth. An etalon is used to pass only the correct 1st order sideband. We use temperature control in order to adjust the etalon peak transmission to match the probe designated spectroscopic line. Thus by locking the laser to the pump line the EOM modulates the probe to pass the correct frequency (The transmission mechanism is depicted in Fig. 2.5.2).

After the probe beam passes the etalon it is cleaned using a spatial filter and then a phase and amplitude spatial modulation is done using an SLM. When this modulation

is not required, the SLM is idle and behaves like a mirror. Moreover, a quadratic phase on the SLM is also possible, turning the SLM into a variable lens. After the modulations are done, the two beams with different linear polarizations are combined using a Glan-Taylor polarizer. The beam angular matching is checked by optimizing the transmission of the combined beam through a single mode polarization maintaining fiber. For some cases a circular polarization is desired, which is created by the addition of a $\frac{\lambda}{4}$ waveplate, thus the beams enter the cell with opposite circular polarizations $\sigma^+$and σ^-. The cell is heated to $40°C - 70°C$ using hot water circulating through the cell copper holder. In order for the cell windows not to be covered with rubidium we also added a cold spot in the tip of the cell by attaching it with a metal wire to the optical table. The cell is surrounded by 3 layers of mu-metal shielding lowering the stray magnetic field a factor of ∼1000. A long metal coil inductor (25 cm) is used to create magnetic fields inside the cell with low variability along the z-axis. After the beam passes the cell another $\frac{\lambda}{4}$ waveplate is used to convert the two beams again to perpendicular linear polarizations. Another Glan-Taylor polarizer passes only the probe beam on to a photodiode in the case of spectroscopic measurements or CCD camera in the case of 2D patterns measurements.

2.5.2 power broadening

We measure the EIT width as a function of the intensity of the pump using a constant probe. Figure 2.5.3(a) shows the broadening of the EIT linewidth with respect to the intensity of the pump. The theoretical width is described in Eq. 1.3.7 and in Sec. 1.3.6. The intensity is a quadratic function of the Rabi frequency of the pump, Ω_c, thus we get a linear fit for the width as a function of the intensity. In Fig. 2.5.3(b) we see this linear shape and by using extrapolation it is straight forward to deduce the decoherence rate which is 3.6 ± 0.2 kHz. This decoherence rate is very similar to other groups results [50, 187]. Taking into consideration the size of the pump and the saturation intensity it is possible to transform the results into $\frac{\Omega_c^2}{W}$ and calculate the

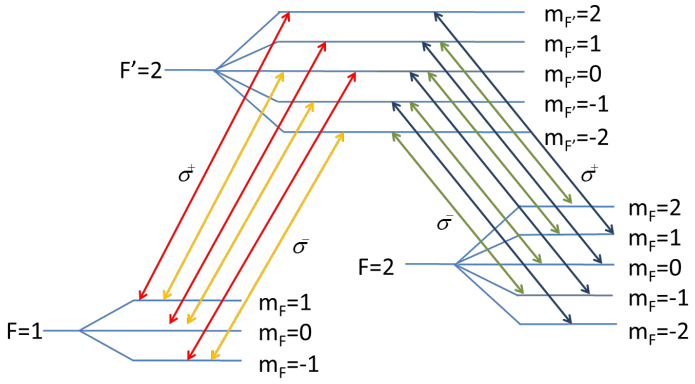

Figure 2.5.4: Zeeman splitting of the D1 line of ^{87}Rb.

slope $1/w$. In our case $W = 480 \pm 50$ MHz which fits the Doppler broadening width as expected (see Sec. 1.3.6).

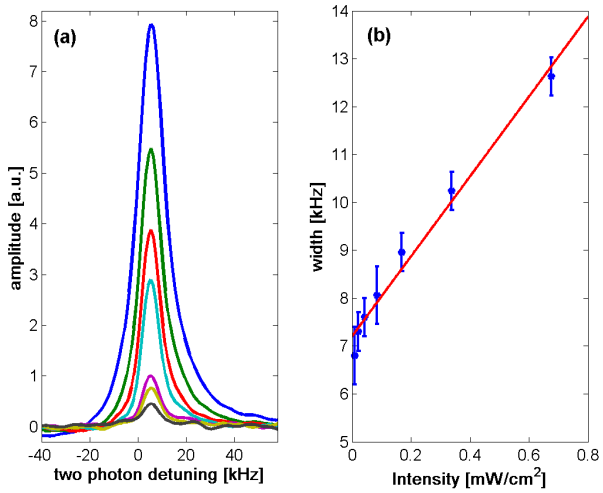

Figure 2.5.3: Power broadening. (a) EIT peak as a function of coupling laser intensity. (b) EIT width according to Lorentzian fit as a function of coupling power.

2.5.3 Magnetic dependence

Adding a magnetic field creates a Zeeman splitting of the hyperfine levels of rubidium (level scheme is depicted in the inset of fig. 2.5.4).

In general for the D1 line, using an arbitrary magnetic field, up to 7 EIT lines

may appear [33]. Due to the vectorial nature of the magnetic interaction, the relative strength of these lines depends on the angle between the beam direction and the magnetic field as well as the polarization of the pump and probe beams [193]. We use a uniform magnetic field in the beam direction using a solenoid, thus the specific configuration we use in our setup is $\mathbf{B} \parallel \mathbf{k}$ with linear polarization. In this case only three lines appear in the spectrum [193, 198] as can be seen experimentally in Fig. 2.5.5. The Zeeman EIT shifts linearly with the strength of the magnetic field with a gradient of 0.7 MHz/G as expected [165].

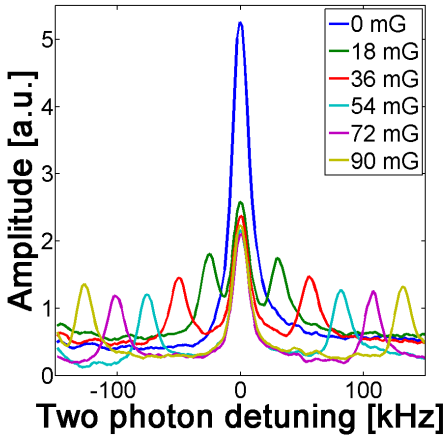

Figure 2.5.5: EIT peak resonance splitting due to external magnetic field. The various colors relate to different Zeeman splitting due to changed magnetic field strength.

It is favorable to be able to generate and control Zeeman EIT, as several works that mapped the coherence time of different EIT setups showed longer coherence time using degenerate Zeeman EIT rather than hyperfine EIT [156]. Although the results presented here are not in a degenerate Zeeman EIT, using the ability to control the Zeeman splitting makes it easy to devise such a system.

2.5.4 Slow light

Probe light pulse was passed through the cell while the pump field works constantly. The probe was detected using a photodiode and a scope and measured with respect to

non EIT resonant light. Taking into account the length of the cell we use (7.5 cm) it is possible to extract the group velocity of light in the matter. Figure 2.5.6 shows the delay of a 10 μs Gaussian pulse in a cell without buffer gas. The delay is 470 ns which corresponds to $V_g = 1.6 \cdot 10^5 {}^m/_{sec}$.

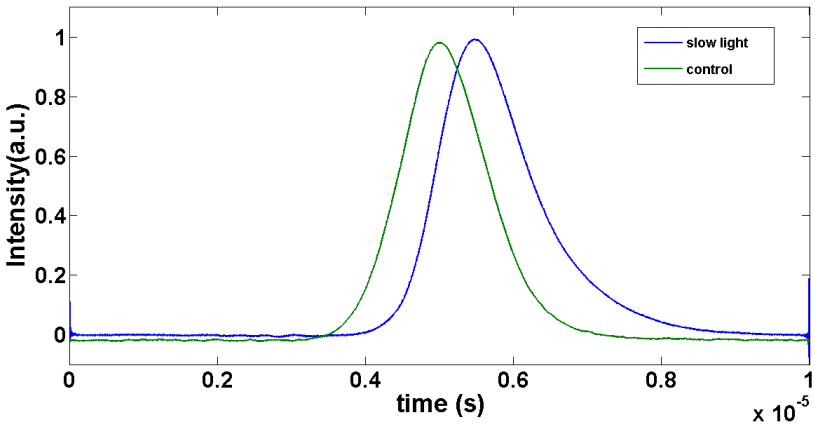

Figure 2.5.6: Slow light without buffer gas. The delay is 470 ns.

Adding a buffer gas allows for much narrower EIT and as a result longer delay times. It is important to notice that in order to produce the best delay time all the pulse spectrum should be contained inside the EIT bandwidth, thus the pulse length in this case is much longer. In our experiment we delayed a 100 μs probe pulse for 15μs which corresponds to $V_g = 5000 {}^m/_{sec}$. This is a fraction of $\frac{1}{60000}$ from the speed of light in vacuum.

2.5.5 Storage

In order to store the probe pulse we turn the pump off while the pulse is still in the cell, wait for a time that is called the storage time, and then turn the pump back on (see Fig. 2.5.7 for the storage protocol).

The remains of the pulse is detected using a photodiode and a scope. Fig. 2.5.8 shows the probe amplitude as a function of time during the storage protocol for different storage times. The inset in Fig. 2.5.8 shows the peak amplitude as a function of the

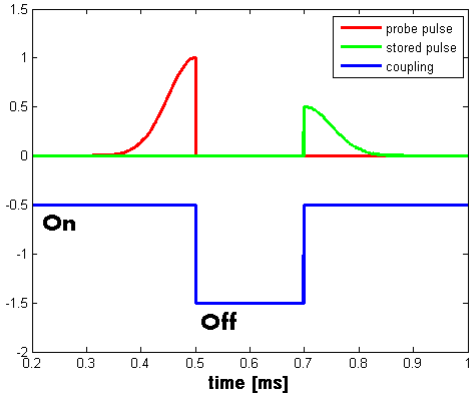

Figure 2.5.7: Storage protocol.

storage time. The life time of the probe pulse using an exponential fit is $81 \pm 5\,\mu s$.

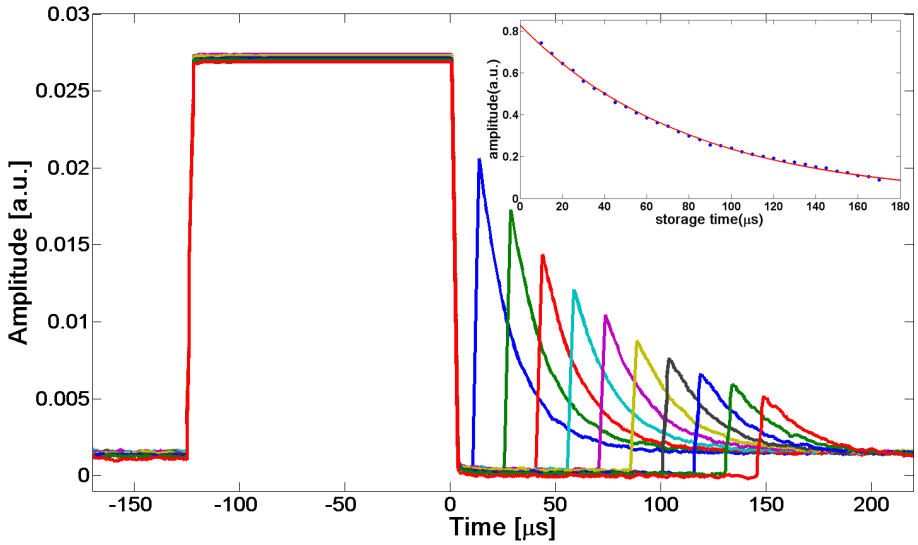

Figure 2.5.8: Probe pulse storage for different storage times. The inset shows the peak amplitude as a function of storage time. The red line represents exponential fit to the data.

Chapter 3

Results

3.1 Control of vortex array using EIT

3.1.1 Introduction

An extremely rich variety of spatially dependent optical phenomena that is derived from the complex susceptibility of EIT media was demonstrated recently, such as waveguiding [181], frequency dependent diffraction, diffractionless propagation, Negative diffraction and induced deflection [51, 54]. Transmission of phase dependent patterns were also achieved and highlighted as an effective way to reduce diffusion effects in storage processes.

This chapter deals with a different phenomenon related to the complex susceptibility, namely, a controllable collective motion of optical vortex arrays. An optical vortex, as described in 2.2.1 is an electromagnetic mode with zero intensity in the center and a cylindrical phase $e^{il\phi}$, where ϕ is defined as an angle variable around the vortex core and l is an integer quantizing the orbital angular momentum (OAM) of the vortex. Optical vortices have a wide range of applications such as optical trapping and tweezing [78], quantum entanglement [60, 115] and contrast enhancement in light microscopy [60]. A single vortex beam was used also as a probe beam in EIT experiments, where the stability of the vortex against diffusion effects, as opposed to a bagel shape flat phase beam, was demonstrated [141]. The transversal collective motion of optical vortex array patterns as they propagate in free-space was studied extensively [30, 82, 126] and was found to depend upon the total OAM of the array (denoted by L, where L=$\sum_i l_i$), the

average distance between the vortices, the vortices core size and the background profile they are embedded in. In general, vortex arrays with L≠0 were shown to rotate as the beam propagate due to the collective OAM of the beam (see Fig. 3.1.2 as an example for such a rotation), while vortex arrays with L=0 do not rotate at all but can contract and annihilate. The movement of each vortex is determined by the phase gradient and the intensity gradient of the beam in the vortex core, thus the movement of each vortex is determined by the phase created due to the other vortices in the array leading to a collective motion [62, 144, 145]. We show here a way to control this collective motion of the vortex array in EIT media using a frequency change, i.e., variation of the two photon detuning.

3.1.2 Vortices above Gaussian background

When more than one vortex is superimposed on a larger Gaussian beam, the angular momentum of the vortices creates an effective force between the vortices that makes them rotate one around each other [82]. This effect is global, meaning that it has to do with the total angular momentum, L, of all the vortices. Vortices with higher total L will rotate faster, on the other hand propagation of matrix of vortices with zero total L will result no rotation at all [62]. The dynamics of optical vortices in a medium can be described by the nonlinear Schrodinger equation (NLSE) [126, 144]:

$$-2ik\frac{\partial u}{\partial z}+\nabla_{\perp}^{2}u+2k^{2}\frac{n_{2}E_{0}^{2}}{n_{0}}|u|^{2}u=0 \tag{3.1.1}$$

where $\nabla_{\perp}^{2}u$ is the transverse Laplacian in cylindrical coordinates, u is the slowly varying envelope of the field, n_2 is the nonlinear refractive index, n_0 is the linear refractive index and E_0 is the amplitude of the field.

Vortices appear also in hydrodynamics, thus a very insightful way of looking at the NLSE is using the hydrodynamic equivalent [144], where this equation is actually the combination of the Bernoulli and continuity equations. By writing $u=f(r,\theta,z)e^{is(r,\theta,z)}$

these equations can be written as

$$-\frac{\partial s}{\partial z}+\mathbf{k}_{\perp}\cdot\mathbf{k}_{\perp}=\frac{\nabla_{\perp}^{\mathbf{2}}\rho^{1/2}}{\rho^{1/2}}-\frac{P}{\rho} \tag{3.1.2}$$

$$\frac{1}{2}\frac{\partial\rho}{\partial z}+\nabla_{\perp}\cdot(\rho\mathbf{k}_{\perp})=0 \tag{3.1.3}$$

where $\mathbf{k}_{\perp}=-\nabla_{\perp}s$, the transverse wave vector acts like the velocity field in fluids in this analogy and the intensity of the beam $\rho=f^2$ acts as the density of the fluid. $P=2\rho^2$ is analogous to the pressure of the fluid so the term $\frac{P}{\rho}$ disappears in a linear media. Concentrating on the case of linear media suitable to free space propagation and EIT using weak fields, two main points can be deduced from this analogy. One is that at all points excluding the singularity, the transverse wave vector is just the sum of derivatives of the phase and amplitude at that place. The second point is that at fluid dynamics the velocity field inside a vortex does not depend on the vortex itself, meaning that the center of the vortex acts as a particle in the local velocity field. As a consequence the vortex center of mass will be affected only by background nonuniform wave vector field or by other vortices wave vector fields. Going back to multiple vortices upon a uniform background, it is now easy to understand the rotation as a hydrodynamic phenomenon. The rotation rate is dependent on the distance between the vortices [145]:

$$\frac{\Delta\theta}{\Delta z}=-\frac{\lambda}{\pi d_V^2}=-\frac{1}{Z_V} \tag{3.1.4}$$

where d_V is the distance between the vortices, hence Z_V is the characteristic distance where the vortices overlap due to diffraction. Because of diffraction Eq. 3.1.4 will not be valid after distance longer than Z_V. The maximal rotation in the linear regime due to diffraction is final and can lead in the far field to $\pm\frac{\pi}{2}$ rotation [1]. An important issue with the rotation of vortices is that only small core point like vortices such as $tanh(r/w_V)$ where $W_V\to 0$ will exhibit rotation like behavior. Large vortices that can

[1]This attribute is connected to the maximal rotation of the Poynting vector of a single LG beam, which is $\frac{\pi}{2}$ in the case of p=0 [133].

be describe linearly as $(\frac{r}{w_r})^{|m|}$ will not circulate but rather move apart one from the other with parallel rectilinear movement. In general, LG beams amplitude behaves as a Laguerre polynomial meaning that no circulation will occur, but in the case of creation of vortices with phase only, the beam starts as a point like vortex and only due to diffraction it will transform eventually to a polynomial vortex.

When adding the nonlinear term much larger rotation angles and effective non diffractive propagation can be achieved [126, 144]. Experiments in waveguides and nonlinear crystals observed this effects [38,145]. In the context of EIT it may be possible to use the nonlinear susceptibility of the medium [57] in order to achieve similar results.

3.1.3 Overcoming diffusion

In the past few years storage of images in warm vapor EIT media for $\sim 10-20\,\mu$s have been demonstrated [158, 180]. The basic problem of storing an image rather than a pure Gaussian beam is the diffusion of the atoms, that apart from inducing decoherence to the stored light, also smears the image. One of the ideas that has been proposed in order to eliminate such diffusion effects is to add also phase to the images. Adding a π phase shift to adjacent features in the image can create destructive interference between two atoms that diffuse from these two features to the same place, eliminating effectively the diffusion outcome [158]. One natural candidate for such diffusion cancellation effect is the LG beam, where the vortex at the center of the beam is actually diffusion immunized as every antipodean points in the beam have a relative π phase shift. Pugach et al. demonstrated that LG beam, opposed to a bagel shape pure phase beam, can stay for long time inside EIT media without the vortex in the center of the beam being filled [141]. Another idea closely related to phase shifts is to store the Fourier transform (FT) of the image and not the image itself [195]. Even a constant phase image can have a variable phase FT thus allowing for destructive interference in the desired places. This method was also demonstrated successfully by Vudyasetu et al. [180]. Recently, promising work showed storage of images in rare earth ion doped

solids for extremely long time of almost 1 minute using rephasing [79].

3.1.4 3D theory for images inside EIT

A theory that accommodates a three dimensional weak probe beam with constant strong coupling field was recently developed by Firstenberg et al. [55, 56]. The basic idea of this theory, that takes into account the various broadening and narrowing mechanisms discussed in 1.3.6, is solving the Maxwell-Bloch equations in the density matrix formalism using Fourier transformation, i.e. in the momentum space. According to the theory if the envelope in the beam direction (z) is sufficiently slowly varying the probe envelope can be calculated as :

$$\widetilde{\Omega}_p(z_2;x,y,t)=\int_{-\infty}^{\infty}\frac{d\omega}{2\pi}e^{-i\omega t}\int_{-\infty}^{\infty}\frac{d^2k}{2\pi}e^{ik_x x+ik_y y}\widetilde{\Omega}_p(z_1;\mathbf{k}_\perp,\omega)e^{ip(k_\perp,\omega)(z_2-z_1)} \tag{3.1.5}$$

Where $\mathbf{k}_\perp$ is the transverse wavevector of the probe profile and the phase acquired is :

$$p(\mathbf{k}_\perp,\omega)=\sqrt{(\frac{\omega}{c})^2-(2\pi\mathbf{k}_\perp)^2}+\chi_{31}(\mathbf{k}_\perp,\omega) \tag{3.1.6}$$

Hence the spatially and spectrally dependent susceptibility can lead to a controllable diffraction of the probe image. For an undepleted plane wave pump beam, the susceptibility of a spatially varying probe in EIT can be written as [55]:

$$\chi_{31}(\mathbf{k}_\perp,\omega)=i\frac{g}{c}K(\omega)n_0\left[1+\tilde{L}(\mathbf{k}_\perp,\omega)\right] \tag{3.1.7}$$

where g is the dipole interaction strength, n_0 is the density of the vapor, $K(\omega)$ is the dimensionless susceptibility in the absence of the pump field and $\tilde{L}$ is the following spatio-temporal spectral function :

$$\tilde{L}(\mathbf{k}_\perp,\omega)=\frac{K(\omega)|\Omega_c|^2}{i(\delta+\omega)-\Gamma_{hom}-D{\mathbf{k}_\perp}^2} \tag{3.1.8}$$

Here Ω_c is the Rabi frequency of the coupling field, δ is the two photon detuning,

$\Gamma_{hom} = \gamma_{12} + K|\Omega_c|^2$ is the decoherence rate and $D = \frac{v_{th}^2}{\gamma}$ is the Dicke-Doppler diffusion coefficient where γ is the relaxation rate due to collisions with the buffer gas and $v_{th} = \sqrt{\frac{k_B T}{m}}$ is the thermal velocity of the atoms. The dynamics of the probe pattern due to this complex susceptibility can be described as a diffusion equation [56]

$$\frac{\partial \Omega_p}{\partial z} = \left[i\chi_0 + \left(\frac{\mathfrak{D}}{v_g} + \frac{ic}{2\omega_0} \right) \nabla_\perp^{\mathbf{2}} + O(\nabla_\perp^{\mathbf{4}}) \right] \Omega_p \tag{3.1.9}$$

with a complex diffusion constant

$$\mathfrak{D} = D \frac{1 - (\frac{\delta}{\gamma})^2}{\left[1 + (\frac{\delta}{\gamma})^2\right]^2} + iD \frac{\frac{2\delta}{\gamma}}{\left[1 + (\frac{\delta}{\gamma})^2\right]^2} \tag{3.1.10}$$

where χ_0 is the EIT susceptibility for an atom at rest and $\frac{1}{v_g} = \frac{\partial \chi_0}{\partial \delta}\Big|_{\delta=0}$ is the slow light velocity. The real part of this complex diffusion corresponds to an actual diffusion of the probe, while the imaginary part is a motional-induced diffraction that can be added to the standard optical diffraction term to create a frequency dependent optical diffraction. Some special cases should be noted: (1) for $\delta = \gamma$ the diffusion part of $\mathfrak{D}$ vanish offering a diffusionless propagation in the media. (2) when $\delta = 0$ the diffraction part of $\mathfrak{D}$ vanish, thus the propagation is standard optical diffraction with diffusion. (3) if $\delta = -\gamma$ and also $v_g = \frac{\omega_0}{c} D$ is obtained then the medium becomes diffusionless and diffractionless. Some examples for the use of this theory such as the elimination and reversal of diffraction were demonstrated [51, 54].

In the context of vortex array, the complex diffusion creates two effects that are frequency controlled. First an enhanced or reduced diffraction. This effect is a way to control the vortex array motion in a different manner than changing the free space diffraction length. The second effect is a controllable diffusion of the pattern which is an effect that cannot be achieved using free space optics.

3.1.5 Experimental setup

Our experimental setup is described in Fig. 2.5.1. As the EIT medium we use the D1 transition of ^{87}Rb, where the Λ configuration is comprised of the hyperfine levels. We use a DFB laser as our source of 795 nm beam. This beam is separated into pump and probe beams using a beam splitter. Both beams pass through an AOM, the probe for amplitude control and the pump for amplitude and frequency control using a double pass configuration. A hyperfine splitting of 6.8 GHz is created using an EOM on the probe beam followed by an etalon used to filter out the unwanted 0 and -1 orders. The EOM is used also to compensate for the frequency mismatch of the probe due to the double pass of the pump. The spatial phase dependence of the beam is created using a liquid crystal SLM (BNS, 512×512 pixels). Finally, both the pump and the probe beams are combined using a Glan-Taylor polarizer and pass through a 7.5 cm quartz cell heated to $\sim 40^oC$. The cell contains isotopically pure ^{87}Rb and 20 Torr Neon as buffer gas. After the cell, the pump and probe beams are separated using another Glan-Taylor polarizer and the probe beam is measured using a CCD camera. For the results described here we use a pump beam with a power of $150\mu W$ and a waist of 2.5 mm.

3.1.6 Results

Figures 3.1.1(a) and 3.1.2(a) present typical results for a vortex array control by changing the two photon detuning using EIT setup. The spatial profile of the probe is a $\sim$0.5 mm waist Gaussian beam with 2×2 vortex array embedded in it. The vortex array in figure 3.1.1(a) comprises two vortices having OAM of +1 and two vortices having OAM of -1, so the total OAM of the pattern is L=0, while in figure 3.1.2(a) all the vorices have OAM of +1, so the total OAM of the pattern is L=4. The phase patterns imprinted on the SLM for these vortex arrays are depicted in Fig. 3.1.3. We chose these two configurations in order to demonstrate the effect of EIT on the two generic possibilities of vortex array, namely, L=0 and L$\neq$0. Figures 3.1.1(b) and 3.1.2(b) show

simulations of optical propagation based on Eq. 3.1.7 of both the situations discussed with good agreement to the experimental results.

Figures 3.1.1(d) and 3.1.2(d) show the dynamics of each vortex center as the two photon detuning is scanned. For L=4 a global rotation accompanied by vortex repulsion is observed (Fig. 3.1.2(c)). The rotation is a signature of the non-zero angular momentum of the array while the repulsion has to do with the movement of the vortices due to the Gaussian envelope of the beam. This repulsion is higher when the rotation is higher thus leading to a more distorted images for higher total L patterns. The circular trajectory of each vortex as described in Fig. 3.1.2(d) is very different from free-space propagation where a linear trajectory was observed [82, 145]. The circular trajectory is due to the combined effects of diffusion and diffraction. The strongest diffusion occurs, according to Eq. 3.1.10, when $\delta = 0$. Indeed this is where the beam radius is largest and also the vortices repulsion is most substantial. L=0 has a different signature with a global contraction (Fig. 3.1.1(c)) and no global rotation. This effect happens since each two adjacent vortices have inverse OAM thus leading to rotation in an opposite direction. Moreover, as the pattern with total OAM of L=0 contracts, the vortices start to join together leading to one large vortex in the middle of the beam. Simulation shows that for strong enough interaction the global contraction for patterns may result in even a total annihilation of the vortices, in agreement with published free-space results of vortex dipoles [29].

As a quantitative measurement of the global rotation that arrays with L$\neq$0 experience, we measure the angle of the connecting line between two vortices with respect to the x-axis. Experimental results for two vortices with L=$\pm$1 are presented in Fig. 3.1.4(a). A total rotation span of more than 0.3 radians is visible (3.1.4(b)). As a comparison Fig. 3.1.4(a) also presents two vortices with L=0 with no rotation at all. The rotation has a dispersive signature, similar to the imaginary part of the complex diffusion, where it is possible to see an extra rotation in one side of the resonance and a contra free-space rotation on the other side. The EIT media in this case enables a

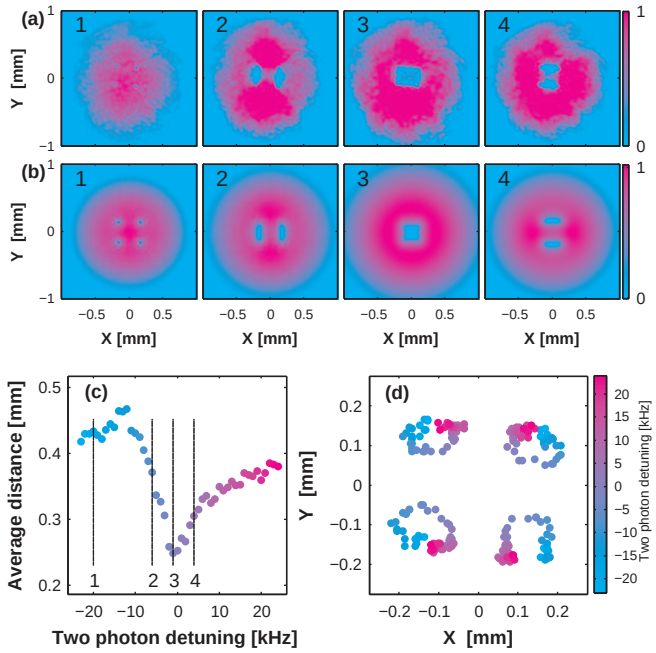

Figure 3.1.1: Experimental results for the collective rotation of four vortices, two l=+1 and two l=-1 with total angular momentum L=0. (a) Pictures for different frequencies with log scaled normalized intensity. The numbers relate to the vertical lines in (c). (b) Pictures of simulations for the same frequencies. (c) The average size of the array measured as the distance between two opposite vortices. The array size at resonance is about half of the original array size. (d) 2D plot of the vortex centers at different detunings. Although each vortex moves in a circular motion as the detuning is scanned, the full array does not rotate but only contracts. Near the resonance (picture (a3)) the four vortices almost combine to one point with zero amplitude and L=0.

manipulation of the effective optical path, thus allows us to change the optical pattern as if it was taken at different positions along the beam traveling axis. Actually, in order to cause this kind of maximal rotation a free space propagation of about fifth of the Rayleigh length is needed. A more effective EIT setup have the potential to rotate the beam by $\frac{\pi}{2}$ enabling a far field rotation. In this view it is possible to think of the medium as a variable lens with a very high NA [30]. Moreover, contra free-space rotation is analogous to a backward movement of the beam from the origin. This effect is a signature of an index of refraction which is smaller than one. Positive or negative total angular momentum creates an opposite rotation as can be seen in Fig. 3.1.4(a). Due to the real part of the complex diffusion an actual diffusion of the beam occurs.

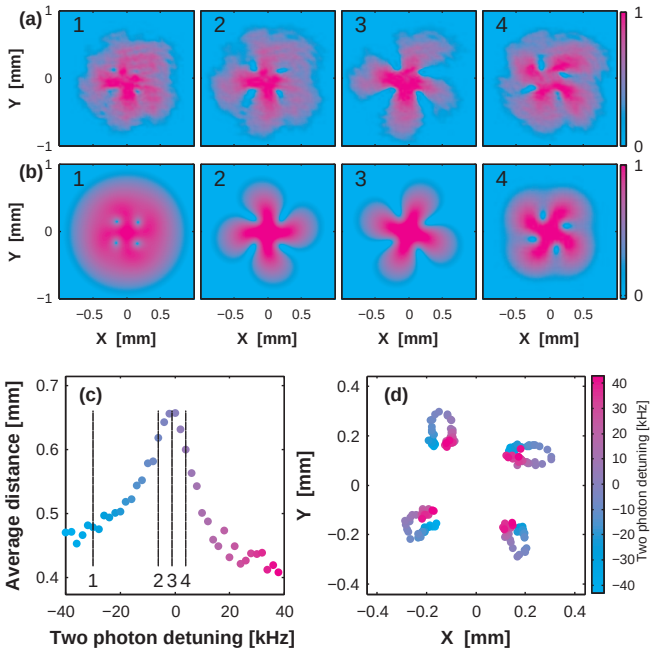

Figure 3.1.2: Experimental results for the collective rotation of four l=+1 vortices with total angular momentum L=4. (a) Pictures for different frequencies with log scaled normalized intensity. The numbers relate to the vertical lines in (c). (b) Pictures of simulations for the same frequencies. (c) The average size of the array measured as the distance between two opposite vortices.(d) 2D plot of the vortex centers at different detunings. In this case, as with L=0, each vortex moves in a circular manner as the detuning is scanned, but here due to the fact that all the vortices rotate in the same direction, there is a global rotation of the entire array.

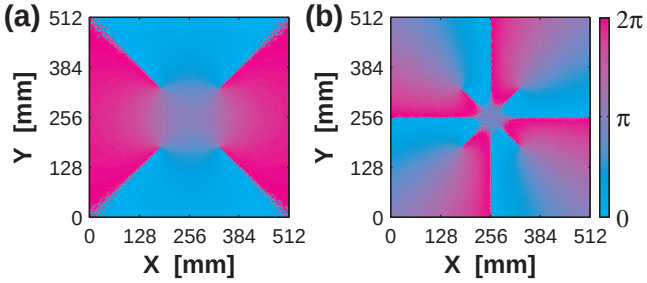

Figure 3.1.3: Phase patterns of four vortex array. The phase of each vortex is These patterns are imprinted on the SLM with the gaussian probe beam directed to the center of the pattern. (a) Two ml=1 and two l=-1 vortices. (b) four l=1 vortices.

This effect was observed and measured before by Firstenberg et al. [52]. Here we show an easy way to measure it by looking at the average distance between vortices with the same optical angular momentum as depicted in figure 3.1.4(b). This increase agrees very well with the EIT line presented also in Fig. 3.1.4(b) as expected.

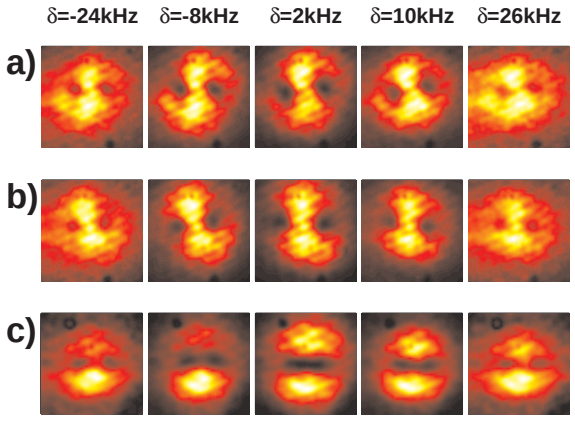

(a) Experimental results for the collective rotation of two vortices. (a) two vortices with $l = +1$ (b) two vortices with $l = +1$ (c) one vortex with l=1 and one with l=-1.

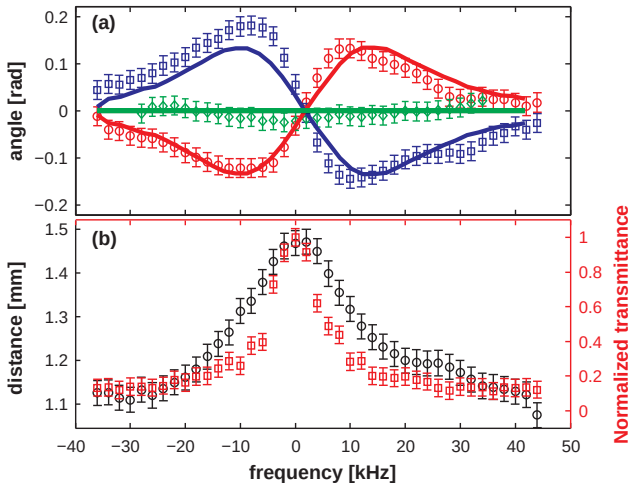

(b) (a) Rotation angle of two vortices. l=1 (red circles), l=-1 (blue squares), l=1 and l=-1 (green diamonds). (b) The distance between two l=+1 vortex centers (Black circles) and the EIT transmission (Red squares) as a function of the two photon detuning. Both curves follow the same trend.

Figure 3.1.4: Quantitative vortex rotation.

Larger arrays of vortices such as 3×3 and 4×4 were also created with similar effects as shown for the 2×2 array case. Due to the fact that the vortices cover a large part of the Gaussian beam, the EIT peak diminishes, thus leading to slightly less pronounced effects. As the dynamics of each vortex is affected by the local field in the point of the vortex, excluding the vortex itself, using a Gaussian field offers a way to manipulate even a single off-centered vortex alone [16]. Moreover, here we exploit the linear regime of the EIT media, but higher intensity will probe the nonlinear Kerr medium with extended rotation spans, not possible in the linear regime [144].

Vortex arrays can be stored in EIT media in a similar manner to previous experiments of storage of patterns using EIT [141, 158, 180]. We measure stored patterns of vortex arrays for different storage times. The stored patterns are similar to the patterns produced in the slow light regime apart from atomic diffusion effects that cause the dark center of the vortices to fill up as the storage time increases. This trend is in agreement with single vortex storage results presented by Pugatch et al. [141]. A typical measurement of such storage dynamics for two vortices with total L=0 can be seen in Fig. 3.1.5. One advantage stored patterns have over the slow light patterns is the spatial purity of the vortex array state. The reason for this purity is that only the EIT controlled light is stored, while in the slow light regime, light that does not go through the EIT process due to optical pumping and incoherent light contamination will also be presented in the pattern.

3.1.7 conclusions

We spectrally control the collective motion of optical vortex arrays by the use of EIT media. It is shown that a non zero OAM vortex array can have an excess free space rotation or contra free space rotation. The EIT effects can be explained by adding a complex diffusion to the free space diffraction and a simulation using the theoretical frame conformed to the experimental data. A major advantage of this method for applications that transfer optical angular momentum to particles [78], such as optical

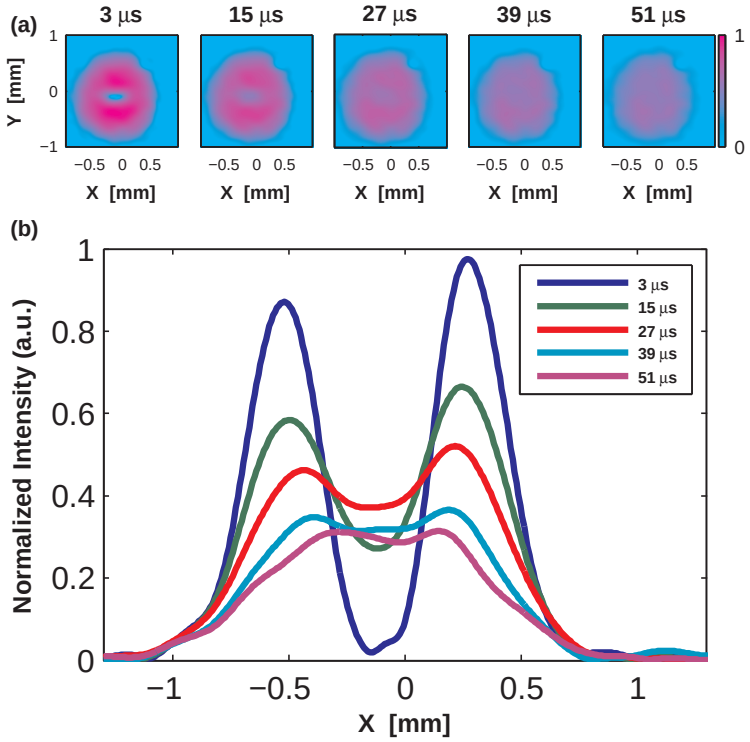

Figure 3.1.5: Storage dynamics of two vortices with total L=0. The storage is done under the condition of zero two-photon detuning. (a) Pictures of the array for different storage times. (b) A cross section of the pictures in (a) along the axis connecting the two vortices. The vortices dark spot vanishes for long storage times.

wrenches, is the ability to move vortices by controlling the frequency. Unlike an actual physical change of the input probe field, which is usually a slow process, frequency control is potentially much faster and more robust. The ability to detect small changes in the displacement of the vortices may also be used in magnetic sensing [122] and quantum measurements of multiphoton states with nontrivial spatial profiles.

3.2 All optical grating using the AC stark shift

3.2.1 Introduction

The ability to control light is of great importance in modern technology and hence society [21, 189]. One of the main ways of controlling light is through the transmission properties of the media. This includes both the phase and absorption of the radiation, through the complex refractive index of the media.

The main methods of refractive control employ a solid infrastructure where the refractive index contrast is designed into the material. The downside of these materials is it is hard to control and tune dynamically. A solution to this shortcoming can be given using light matter interactions. Over the years a variety of different methods for creating electromagnetically induced structures have been discovered [23, 61, 80, 93, 107, 172, 181]. These all have a common element that instead of switching on and off a fixed structure, the structure is created by the electromagnetic field itself [10].

Probably the most noteworthy of these methods is that of the photorefractive effect [61]. Photorefractive materials are both photoconductive and electro-optic, Through the photoconductive effect donors or acceptors are excited from the band gap, where they are free to drift or be driven away. In this way a spatial arrangement of charge can accumulate in the darker regions that will modify the refractive index of the material through the electro-optic effect. Although this effect can be detrimental, such as in Electro-Optic Modulators, it may also be put to good use, such as in holographic recording [61] and electro-holographic switching [149]. While the induced photorefractive effect remains after the initial electromagnetic field ceases, many other systems have a much shorter lived response. These invariably involve using an atomic vapor to mediate the light matter interaction.

Included in these mechanisms is atomic optical pumping [93, 172], where the incident light will excite the electrons in a resonant transition, allowing them to decay to a non resonant ground state, thus changing the number of atoms involved in a particular

transition and correspondingly the resulting susceptibility. A different scheme involves the Faraday effect. Here right and left circularly polarized light interact with different Zeeman sub levels of the ground state. Normally these levels are degenerate, but in the presence of a magnetic field this degeneracy is lifted and Faraday rotation can occur, with the different polarizations experiencing different refractive indicies. A non-linear effect such as "hole burning" causes the non-linear Faraday effect, which can be orders of magnitude larger than the linear regime. Using this effect a grating based upon the control intensity was created [24, 94]. It has also been shown theoretically and experimentally that in EIT media a grating patterned coupling laser beam will cause diffraction to the probe, which can be used for optical routing [23, 107, 123]. In a different set-up a more general coherent Raman process has been shown to produce wave guiding [181].

Here we present and demonstrate a novel means of refractive index control using the AC Stark effect [109]. This concept is an extension of the double Lorentzian atomic prism [162] where an increased atomic density is used to control the refractive index of an atomic vapor. The essential idea is to manipulate this refractive index profile using a control laser, which shifts the transition lines through the AC Stark effect. Hence the most obvious realization of this is in an atomic vapor. However one could envision other systems such as quantum dots or rare earth doped crystals where the same principles could apply. In contrast to previous methods, this is a non-resonant, incoherent process, that can work in systems even at high temperatures. Uses may be found in beam amplification, interferometry, optical interconnections [94] and control of quantum pulses.

3.2.2 Controlled AC Stark Shift

The general theory behind the AC Stark shift in a two level system can be described using dressed states as was described in 1.2.4. Now we wish to consider a sufficiently detuned control field to avoid multilevel effects and a near resonant probe field. The

general Hamiltonian is

$$\hat{H} = \hat{H}_0 + \hat{V}_s + \hat{V}_p \tag{3.2.1}$$

where $\hat{V}_s$ is the AC Stark perturbation from the control laser and $\hat{V}_p$ is the perturbation of the probe laser. In order to find the susceptibility of the probe for a Stark shifted system with atomic transition frequency $\omega_0 = \frac{E_2 - E_1}{\hbar}$ lets consider first the Stark Hamiltonian

$$\hat{H}_s = \hat{H}_0 + \hat{V}_s = \hbar \begin{pmatrix} 0 & \Omega_c/2 \\ \Omega_c^*/2 & \triangle_c \end{pmatrix} \tag{3.2.2}$$

where $\triangle_c = \omega_c - \omega_0$ is the control field detuning and Ω_c is the Rabi frequency.

The eigenvalues of this Hamiltonian are

$$\lambda_\pm = -\frac{1}{2}\Delta_c \pm \frac{1}{2}\sqrt{\Delta_c^2 + \Omega_c^2} \tag{3.2.3}$$

The new energy level, $\hbar\omega' = \hbar(\omega_0 + \triangle\omega_0)$, will be

$$\omega' = \omega_c - \sqrt{\Delta_c^2 + \Omega_c^2} \tag{3.2.4}$$

or alternatively the effective shift to the transition frequency $\triangle\omega_0$ is

$$\Delta\omega_0 = \Delta_c - \sqrt{\Delta_c^2 + \mid \Omega \mid^2} \simeq -\frac{\mid \Omega \mid^2}{2\Delta_c} \propto \frac{\text{Intensity}}{\text{Detuning}} \tag{3.2.5}$$

Due to the fact that the AC Stark effect works through a virtual photon it can be a very fast process, on the order of the detuning Δ_c of the control field (The uncertainty principle is $\triangle E \triangle t \geq 1$, and the energy of the virtual photon will be $\sim \hbar\triangle_c$ giving a timescale of $1/\triangle_c$).

Now it is possible to use the new energy level $\hbar\omega'$ as the unperturbed system for the probe beam, thus the probe Stark shifted susceptibility can be written using Eq. 1.2.11 as

$$\chi_s = \frac{N\mu^2}{\epsilon_0\hbar(\omega - (\omega_0 + \triangle\omega_0) + i\Gamma)} \tag{3.2.6}$$

It should be noted that this approximation assumes that the dipole operator and the decay constants remain unchanged even in the dressed state basis, which will cease to hold at larger mixing angles.

At large values of Ω_c and small detunings ($\Omega_c > \Delta_c$) aside from the Stark shifting there will be significant changes in the populations, with a greatly increased probability of finding the electron in the excited level. With more than two levels, the electron will also decay out of the excited state to other energy levels, leading to optical pumping.

Figure 3.2.1a shows the calculation of the expected susceptibility due to the AC Stark shift based on Eq. 3.2.6. This calculation is taking into consideration the practical limitations of the available control laser in terms of power ($\sim$ 100 mW) and focusing capabilities (f $>$ 4 cm) as well as constraints on heating the available rubidium cell ($\sim$ 100 °C), both in terms of its ability to withstand the heating and the resulting increase in optical density. Of interest is the resulting change in the refractive index and absorption through the cell that would be the consequence of these profiles. If the un-shifted susceptibility is χ_0 and the AC Stark shifted susceptibility is χ_s, then the corresponding refractive indices will be $n_0' + in_0'' = \sqrt{1+\chi_0}$ and $n_s' + in_s'' = \sqrt{1+\chi_s}$. The shift in the real part of the refractive index δn will be

$$\delta \mathrm{n} = \mathrm{n}_0' - \mathrm{n}_\mathrm{s}', \tag{3.2.7}$$

the absorption α_0 is

$$\alpha_0 = \frac{2\pi \mathrm{n}_0''}{\lambda}, \tag{3.2.8}$$

and the shift in α, is $\delta\alpha$ where

$$\delta\alpha = \frac{2\pi\left(\mathrm{n}_0'' - \mathrm{n}_\mathrm{s}''\right)}{\lambda}. \tag{3.2.9}$$

Figure 3.2.1b reveals that a change in the real part of the refractive index of O(10^{-6}) could be achieved away from the center of a transition line, where there is still significant

transmission 20 - 80%. A larger change in the real part of refractive index of O(10^{-5}) would occur at the center of the transition but this is accompanied by a large imaginary part of the refractive index and hence negligible transmission.

3.2.3 Experimental Design

Bragg grating configuration

It was decided to build a thick Bragg grating [92] in order to detect the change in refractive index. The periodic arrangement was chosen to efficiently utilize the predicted small phase shifts, $\delta n \approx 0(10^{-6})$. A thick Bragg grating has the property that light incident at the Bragg angle will be diffracted at the Bragg angle. In an ideal case (sufficiently thick), there will not be other orders of diffraction and the incident light can be completely diffracted into this order.

A thick Bragg grating can be made when two co-propagating coherent electromagnetic fields interfere, if the intensity profile is converted into a corresponding refractive index profile.

Interfering two electric fields $\underline{E}_1 = A_1 \cos(\underline{k}_1 \cdot \underline{r} - \omega t + \phi_1)$and $\underline{E}_2 = A_2 \cos(\underline{k}_2 \cdot \underline{r} - \omega t + \phi_2)$, assuming $A_1 = A_2 = A$ and taking the polarization to be in the y direction, gives an intensity

$$\begin{aligned} \mathrm{I} &\propto \left\langle |\underline{E}_1 + \underline{E}_2|^2 \right\rangle \\ &\propto \left\langle |\underline{E}_1|^2 \right\rangle + \left\langle |\underline{E}_2|^2 \right\rangle + 2\left\langle |\underline{E}_1 \cdot \underline{E}_2| \right\rangle \\ &\propto A^2 + A^2 \cos(2kx \sin\theta + \Delta\phi) \end{aligned} \tag{3.2.10}$$

The intensity grating will therefore have spacing $d = \frac{\lambda_c}{2\sin\theta}$, however the Bragg angle is given by $\sin\theta_B = \frac{\lambda_p}{2d}$. Therefore when $\lambda_p \backsimeq \lambda_c$ such an intensity grating will have the property that the Bragg angle for the probe will be equal to the incident angle of the interfering control lasers.

Therefore for such intensity gratings, the diffracting probe needs to be aligned along

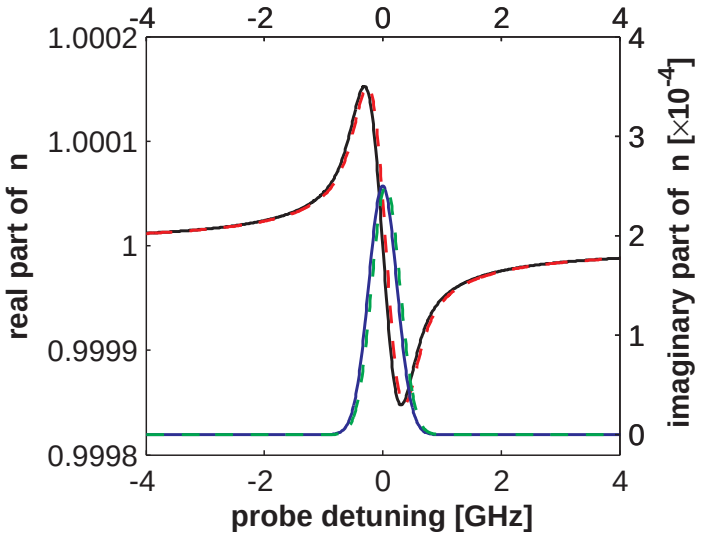

(a) Calculated shift in complex refractive index due to AC Stark, The bold lines show the unshifted refractive index of a rubidium transition (real part - black, imaginary - blue). The dashed lines show the refractive index in the presence of the control laser which induces an AC Stark shift that shifts the refractive index profile (real part - dashed red, imaginary - dashed green).

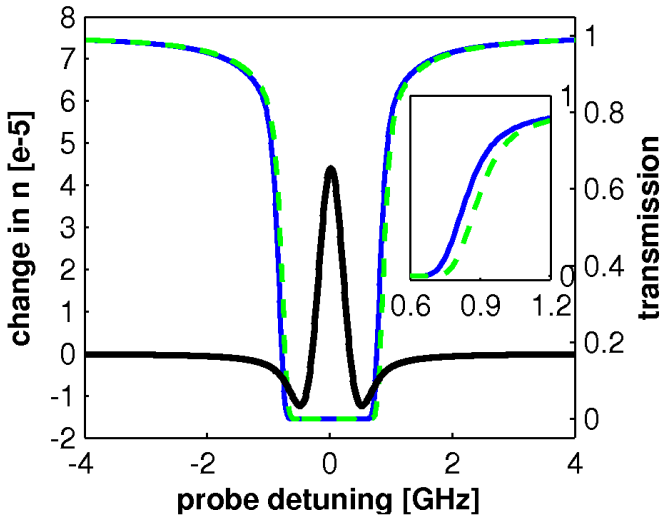

(b) The shift in the refractive index creates a contrast in both the real part of refractive index (black) and the imaginary part. The imaginary part causes absorption through the cell. The unshifted profile (solid blue) is shown contrasted to the shifted profile(dashed green).

Figure 3.2.1: Calculated shift in refractive index due to the AC Stark Effect. Laser power of 60 mW , waist size $800\mu m \times 85\mu m$, detuned by 2.7 GHz. The rubidium cell of 7.5 cm is heated to 85 °C. This calculation is for a single Doppler broadened transition.

one of the control beams, and then the resulting diffracted probe will then lie upon the other control beam.

Experimental setup

We use a configuration of counter-propagating orthogonally linearly polarized beams, see Figure 3.2.2a. This is because such a configuration creates a 'clean' port for the signal.

A picture of the experimental setup is presented in Fig. 3.2.2b. The control laser is split by a non-polarizing beam splitter in order to create two paths, named the "principal control" and the "secondary control". A two mirror walk is added to each control path for the purpose of alignment and grating adjustment. The angle between the principal and secondary control is measured and adjusted by observing the spacing of the grating on a camera. The axis of the principal control is aligned first and kept fixed with other directions and angles being aligned relative to this direction. The resulting control interference, and probe can be seen in Figure 3.2.4.

Atomic media

As atomic media we use rubidium vapor. We use the D1 transition where a total of 8 hyperfine transitions are present within an 8 GHz range, see figure 2.4.1. In most of the presented work we use an isotopically pure ^{85}Rb for the experimental cell, giving four transitions, while the far-detuned frequency of the control laser is identified by the ^{87}Rb transitions (primarily the F=1→F'=2 transition) in a natural abundance cell. Another attractive feature of rubidium is its high vapor pressure, which changes greatly with temperature. This allows for density variations over many orders of magnitude with relatively small changes in temperature (from 25 ^{o}C to 130 ^{o}C the pressure changes from $10^{-7}$to 10^{-3} Torr).

There is flexibility in choosing the frequencies of the control and probe lasers as it is sufficient for them to share a common level for the AC Stark scheme to work. If the

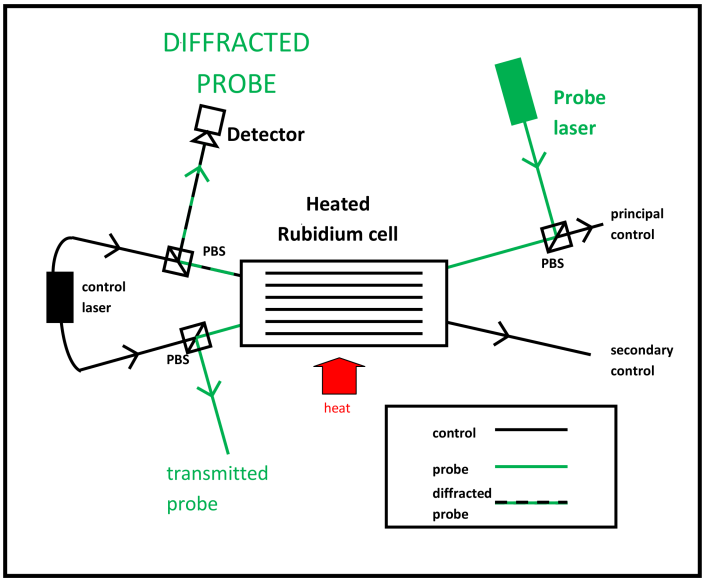

(a) Schematic of experimental set up.

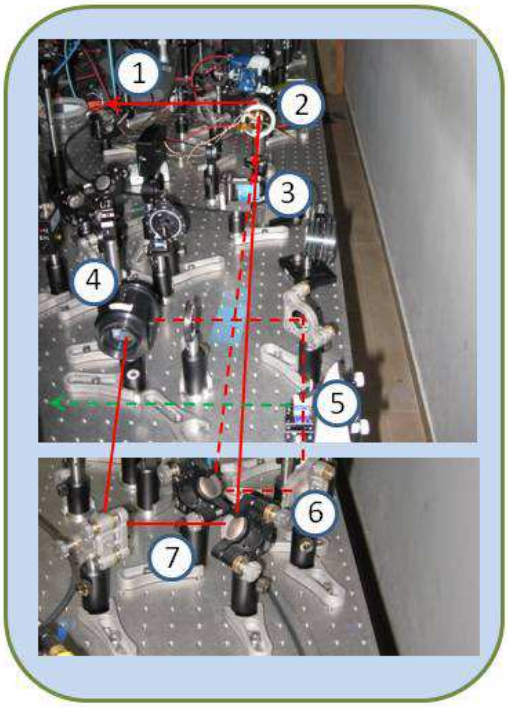

(b) Photograph of the experimental set up. 1 Continuation of control path, 2, Rubidium Cell, 3, Cylindrical lens f=30 cm in vertical direction, 4, NPBS - creating the two control beams, 5, PBS - to separate the diffracted probe (dashed green), 6, Two mirror walk for secondary control (dashed red), 7, Two mirror walk for principal control (red).

Figure 3.2.2: Experimental setup.

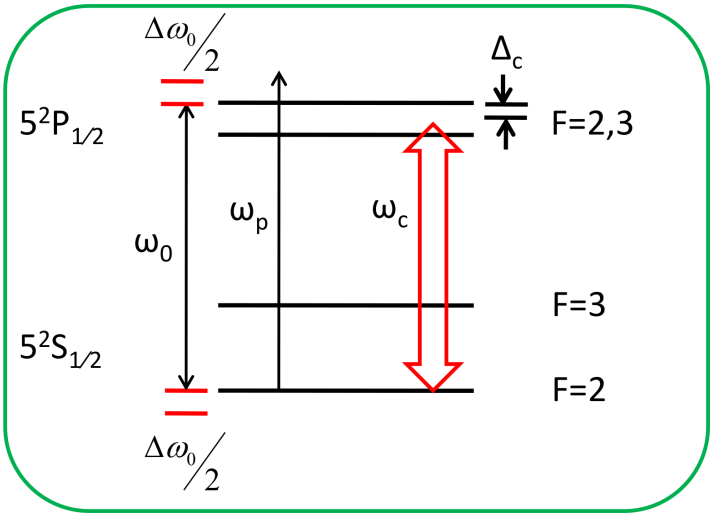

Figure 3.2.3: AC Stark shifting of ^{85}Rb D_1 lines. A control laser detuned from a transition by Δ_c will cause a shift to each of the levels of a transition ω_0 of $^{\Delta\omega_0}/_2$. The probe at frequency ω_p experiences the transition with shifted frequency $\omega_0 + \Delta\omega_0$.

control and probe only share a common ground level then the shift will be half that of equation 3.2.5. The maximum shift will be when they share both the ground and excited levels, however this choice adds a challenge of designing an experiment that will separate the two lasers which will be nearly identical in frequency (separated by approximately the control detuning Δ, O(GHz)). In this work the frequencies used were all close to the ^{85}Rb D_1 lines (795 nm), with the AC Stark shift for one transition shown in Figure 3.2.3.

Scanning and identifying the laser frequencies

The probe laser is a DFB (Toptica DL 100) with very good stability in time (with negligible drift in the course of an experiment) and large mode hop free range (20 GHz). We measure the frequency using a saturation absorption spectroscopy.

The control laser is our home built ECDL (see 2.1.1). The mode hop free range for this laser is much smaller (up to 3 GHz, typically less than 1 GHz). This limited mode hop free range of the ECDL presented a problem in measuring large detunings of the laser ($>$ 2 GHz). Measurement of detunings outside of the absorption lines was

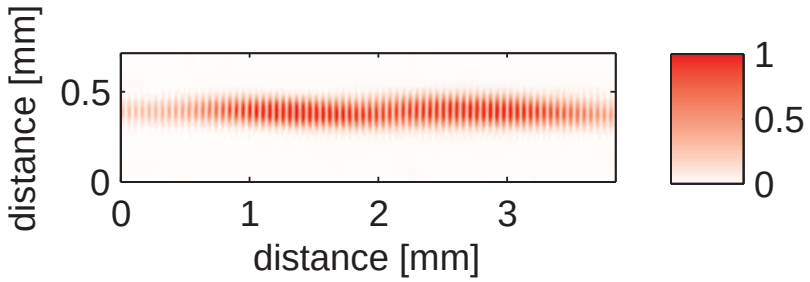

(a) Interference of two control beams, spacing 55 µm, height 150 µm, width ≈ 3 mm through the length (7.5 cm) of the cell.

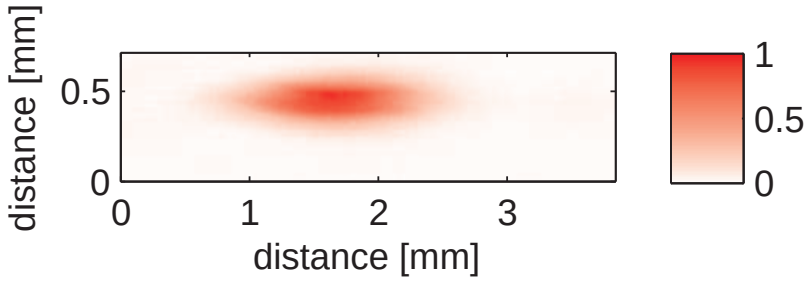

(b) Probe beam in middle of the cell , horizontal waist 615 µm vertical waist 155 µm.

Figure 3.2.4: The interfering light beams are translated into a refractive index grating through the length of the rubidium which causes diffraction of the probe.

accomplished by making small changes in the current (of the laser diode) and dc offset voltages (of the grating piezo electric crystal). These adjustments cause a small shift in the center of the location of the frequency scan of the laser. By keeping the shifts small so that an overlapping frequency region is scanned each time, and under the assumption that the frequency scanning is linear and does not change as the stable region moves, the frequency can be scanned and results of Fig. 3.2.8 were obtained. Using this method it is possible to obtain a scan of over 12 GHz.

Temperature control

Temperature control of the cell is achieved by wrapping the rubidium cell in about eight loops of heating strip (Nikrothal 60). A maximum power of approximatetly 30 W is used to heat the cell. The temperature is monitored using a thermistor (Thorlabs

TH10K) attached close to the cold spot of the cell to give the best measure of the vapor density.

Power variations

The power of the probe and control is varied using a waveplate ($\lambda/2$) in a rotation mount before a polarizer. The transmitted power for a specific phase plate rotation is calibrated by measuring the transmitted power on a power meter.

The signal

The experimental design gives a clean port for the diffracted signal, but this creates a difficulty in locating the exact position of this signal. The control laser is first tuned to a ^{85}Rb D_1 resonance to create an optical pumping grating and the location is optimized with this diffracted signal. Care was taken not to amplify the background signals that reached the diffracted probe path. These consisted of a portion of the control laser that is reflected inside the PBS and part of the transmitted probe that is clipped by the mirror on the secondary control path.

3.2.4 Grating simulation

Although the theoretical efficiency of a thick Bragg grating can be 100%, this is only in an ideal case, and for well defined grating lengths and angles. In the proposed grating produced by two interfering Gaussian beams there will be an envelope in refractive index that follows the intensity of the interfering laser beams. The grating efficiency will also be determined by the fixed cell length and the deviation of the probe from the Bragg angle. Thus a simulation of a probe propagating through space with a spatially dependent phase difference, corresponding to the intensity of the control, was carried out to determine the feasibility of this experiment.

The propagation of light through the grating was simulated by MATLAB script based upon the spatial Fourier component and the propagation transfer function [68].

Using this transfer function a 2D array representing a Gaussian beam was propagated through space. In the grating region an appropriate spatially dependent phase

$$\phi(x,y,z) = \frac{2\pi}{\lambda}\delta n I(x,y,z)z + i(\alpha + \delta\alpha_0 I(x,y,z))z \tag{3.2.11}$$

is added to the profile. The efficiency of the diffraction was measured by taking the far field picture and integrating over the diffracted order.

The simulation results are summarized in Fig. 3.2.5, where it could be seen that a diffracted signal of ∼1 μW is possible, starting with a probe power of 1 mW. This could be achieved with the rubidium cell heated to around 100°C, and two control laser beams with a power of 50 mW each, detuned by 2 GHz from a transition, interfering with an angle of 0.01 rad, all realistic experimental parameters.

It is also possible to see various ways to improve the grating efficiency. Figure 3.2.5a shows the importance of a small interference angle and good alignment. Figure 3.2.5b shows the importance of matching the probe size to the grating. While Figure 3.2.5c shows the importance of achieving a large change in refractive index contrast, δn.

For an AC Stark grating, it is expected that for small values of the refractive index contrast, δn, and large control laser detunings equations 3.2.5 and 3.2.7, could be linked giving,

$$\delta n \propto \delta\chi \propto \frac{\partial\chi}{\partial\omega}\delta\omega \propto \frac{Intensity}{Detuning} \tag{3.2.12}$$

On the other hand, the reflectence of thick Bragg grating is proportional to $(\delta n)^2$ [92, 146], thus the efficiency of the grating, e, is related to the Stark shift by,

$$e[\%] \propto (\delta n)^2 \propto \left(\frac{Intensity}{Detuning}\right)^2 \tag{3.2.13}$$

3.2.5 Results

The first result is the detection of diffraction of the incident probe laser at the predicted Bragg angle. Figure 3.2.6 shows the diffracted probe signal as the probe frequency

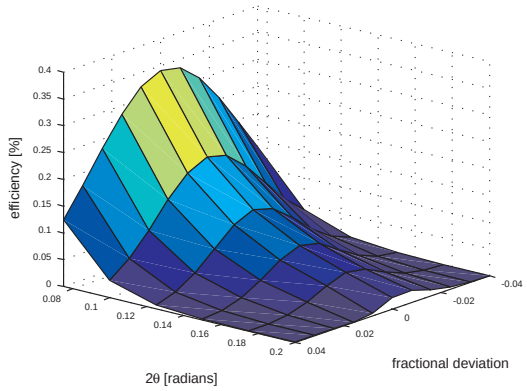

(a) Expected grating efficiency versus angle between control beams, 2θ, and probe fractional deviation from Bragg angle, $\frac{\Delta\theta_{probe}}{\theta_{Bragg}}$, with equally sized probe and control beams, and with refractive index contrast $\delta n = 10^{-6}$, .

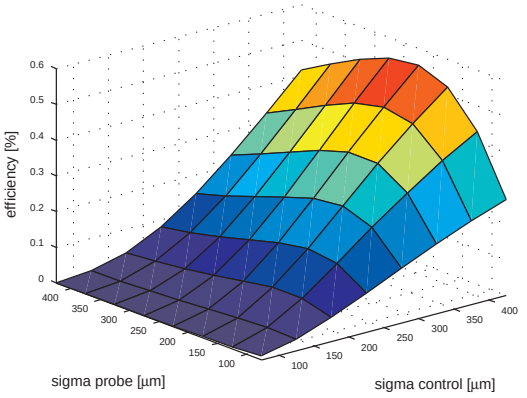

(b) Expected grating diffraction efficiency versus control and probe sizes, with perfect alignment, $2\theta = 0.01$ rad, and with refractive index contrast $\delta n = 10^{-6}$.

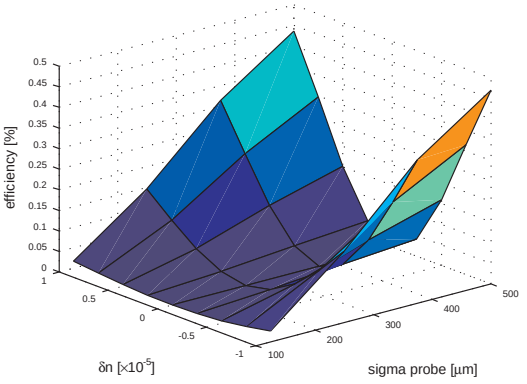

(c) Expected grating efficiency with changing probe size and refractive index contrast.

Figure 3.2.5: Simulations of the expected grating efficiency , show that an efficiency of O(0.1%) can be achieved with an angle between the control laser beams of 0.01 rad and equal control and probe beam sizes. Increasing the δn will increase the efficiency.

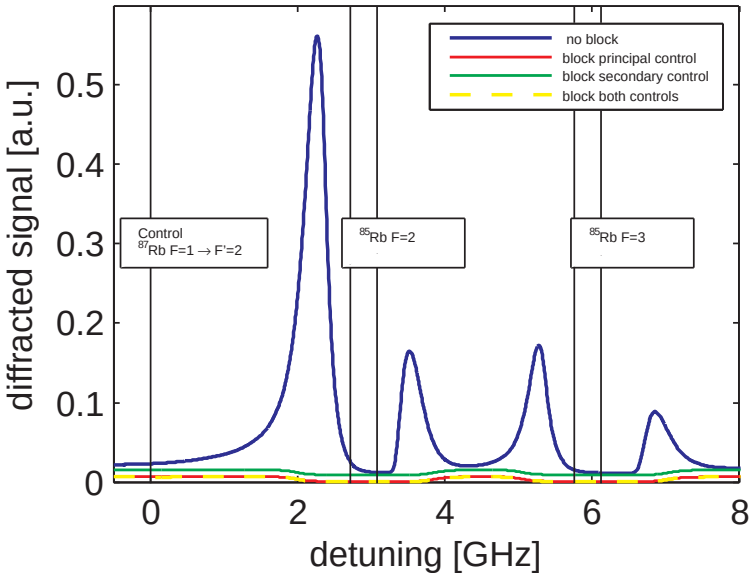

Figure 3.2.6: Diffracted signal with background. The detuning was measured from the ^{87}Rb F1 $\rightarrow$ F′2 transition, where the control laser was positioned. [cell temperature = 135 °C, grating spacing = 55 µm, laser power = 50 mW].

is scanned through the ^{85}Rb D_1 transitions, and keeping the control laser detuning constant. The diffracted signal is stronger at the expected locations, corresponding to the edges of the absorption. The diffracted signal is only observed in the presence of both control beams and probe laser, blocking either control beam destroyed the diffracted signal, thus assuring that the signal is indeed due to the grating. The small background, in the absence of a grating, is derived from two sources. Firstly, a small amount of the secondary control enter the path of the diffracted probe, due to non ideal optical elements. Secondly, due to the shallow angle (<0.5°) between the control beams and hence transmitted and diffracted probes, a small fraction of the diverging probe is clipped by a mirror on the path of the secondary control and hence diffracted probe, which enter the detector for the diffracted probe.

The diffraction signal is clearly the result of a non-resonant AC Stark effect as the control laser is detuned by 2.7 GHz from the closest ^{85}Rb transition. The optical pumping decays as $(1/\Delta)^2$ for large detunings [164] , and therefore is negligible in this

experiment. The fact that the signal appeared at the frequencies on the edge of the transmission signal where a significant change in refractive index, δn, is accompanied by significant transmission is consistent with the theoretical expectation (see Fig. 3.2.1b). There is a peak on each side of the absorption profile, and the overall diffraction efficiency tends to decrease with increased detunings of the control laser corresponding to a reduction in AC Stark effect as predicted by Eq. 3.2.5. The relative heights of the different peaks can largely be explained by considering the absorption. In addition to the decrease in size with detuning, the AC Stark effect also cause a change to the imaginary part of the refractive index. This results in the signal corresponding to the closer side of the absorption occurring at a greater transmission, and hence greater efficiency, than the signal on the further side.

Calculations and simulations were preformed in order to understand the relative heights of the different peaks in the diffracted signal. The simulation included the different hyperfine transitions, their relative strengths and corresponding detunings, whilst including the effects of counter-propagating probe and control lasers, optical pumping (by the probe laser which is not perturbative) and saturation effects. Figure 3.2.7 reveals the overall consistency between the simulation and the results with no fitting parameters.

In a different experiment the control laser frequency is varied while the probe frequency is kept constant. It can be seen in Fig. 3.2.8 that the diffraction efficiency falls off with increased detuning. Fitting to a logarithmic plot gives a value of -1.99 ± 0.02 consistent with the quadratic dependence predicted by theory for large detunings as in Eq. 3.2.13. When the control frequency came close to the ^{85}Rb F=2 lines, optical pumping is increased and the efficiency of the grating decreases. When the control frequency is on the other side of the ^{85}Rb F=2 lines the AC Stark shift is in the opposite direction creating a region of strong absorption for the probe and no diffraction is observed.

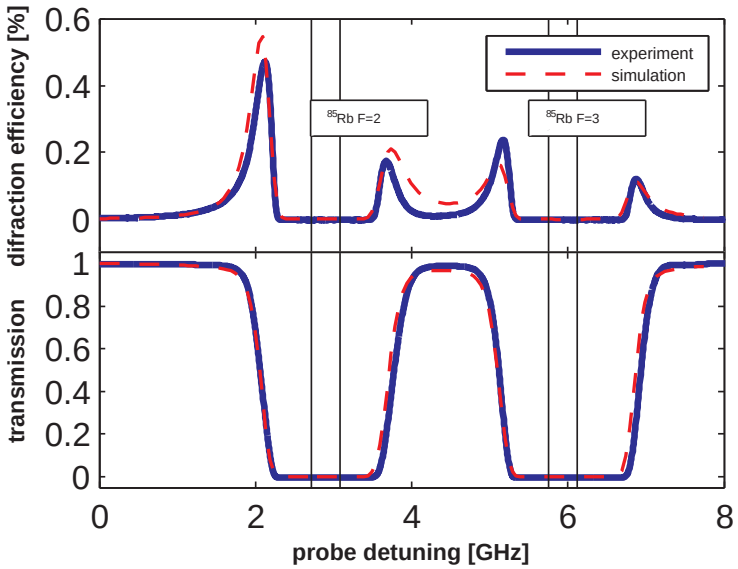

Figure 3.2.7: The probe detuning is scanned while the the control laser frequency is kept at constant frequency on the ^{87}Rb F = 1 $\rightarrow$ F$'$ = 2 transition, the detunings were measured from this frequency. [cell temperature = 135 °C, grating spacing = 55 µm, laser power = 60 mW].

3.2.6 Conclusions

An electromagnetically induced thick Bragg grating has been produced using the AC Stark Effect. This has been achieved by finding the correct parameters of atomic density and control laser intensity and proper arrangement. Diffraction from this grating has been observed for a probe laser close to the ^{85}Rb D_1 lines when the rubidium was heated to around 100 °C, and the control laser was far detuned from these lines ($>$ 1 GHz). The behavior of this grating is consistent with the AC Stark effect as the strongest signal occurs on the edge of the transmission profile. The efficiency also behaves in accordance with expected change in control detuning and intensity. Attempts have been made to explain the subtleties of the effect by considering the optical pumping of the probe, counter-propagating probe and control, hole burning and absorption grating yielding a simulation that fits very well with the results.

A more powerful control laser would produce a greater AC Stark shift and higher efficiency. It should also be possible to increase the efficiency of the grating by heating

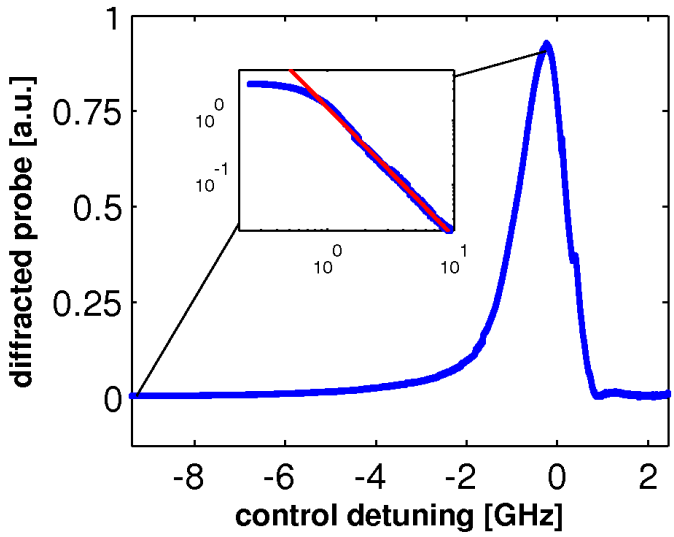

Figure 3.2.8: The control detuning is scanned while the probe detuning is kept constant (at 2.2 GHz from the ^{87}Rb F = 1 → F′ = 2 transition the peak in 3.2.7). The sign of the detuning is chosen to be consistent with Fig. 3.2.7 (moving away from the ^{85}Rb D_1 transitions).

the cell to a higher temperature (this would require a special cell as experience has shown the limits of a standard cell to be about 140°C). A similar work that was done by our collaborators at Rochester university with small cells that can be heated to very high temperatures yielded efficiency of $> 20\%$ [109]. Simulations also indicate that an increased cell length would improve the efficiency.

Although not been found yet, these structures are expected to have fast response times. The fundamental limits to the time response of such a structure could come from two sources, inherently from the AC Stark effect and indirectly from the geometry of the constructed structure. Theoretically the switching time should be limited by the AC Stark effect which scales as $1/\Delta$, in our case <0.5 ns. A faster switching time can be achieved by using larger detunings. This will involve using a greater intensity to achieve a significant Stark shift. Optical pumping caused by the increased intensity seems to be avoided since optical pumping scales as (I/Δ^2).

Theoretically it should be possible to build any structure according to the light intensity. This will require 'structuring' the light in the required pattern, which will have the additional challenge of maintaining the intensity high enough for efficient AC

Stark shifting. Such fast control of light may find uses with control of quantum pulses or maybe even in the transfer of classical information. However practical uses will require greater efficiencies.

3.3 Transient coherence of EIT media under strong phase modulation

3.3.1 Introduction

The narrow linewidth of EIT makes it suitable for applications in many fields such as extreme slow light, quantum storage devices, non linear optics and high sensitivity magnetic sensors. On the other hand, this narrow linewidth directly limits the bandwidth of data that can be processed. A signal which has a broader bandwidth than the EIT linewidth will be filtered such that only part of the pulse having the EIT linewidth will be transmitted and delayed [151, 170]. In terms of sensing this means that although a very high sensitivity is possible using EIT, it is a problem to probe with this sensitivity a broadband field in a simple way. Possible solutions to this problem may arise from different approaches. One idea is to use a heterodyne measurement of the EIT signal with a broadband probe [151] using the interference of the dispersive part of the EIT [111]. This may offer an increased resolution and broaden the sensing bandwidth since the dispersive part is decaying in a slower manner. In order to get a more substantial bandwidth another idea is to use a multimode EIT system where each EIT line has still a narrow bandwidth but spreading the signal across many systems allows for a broader signal. Such systems were devised spatially [43] and spectrally [26, 190] for larger data capacity as well as for broadband magnetic sensing [17, 179]. A different approach is to use dynamic EIT where the transient response may have a much broader bandwidth than steady state EIT. The transient response of an EIT media to a sudden switching [71, 105, 121, 136] as well as for ac magnetic field [117] was explored theoretically and experimentally for various regimes. For a constant detuning the decay of the transients is dictated by the EIT linewidth, while the frequency of the transient oscillations equals the two photon detuning [121, 136]. The detuning can be larger than the linewidth leading to an under-damped oscillator response. In the case of a linear sweep through the resonance the frequency of the transient is chirped [136]

and behaves similarly to a Landau-Zener (LZ) transition [75, 88]. Transients were used also as a magnetic sensing technique to measure the Earth's magnetic field with $1.5\frac{nT}{\sqrt{Hz}}$ sensitivity [101].

Here we take both concepts of multimode spectrum and transient dynamics and combine them together to create a new method for measuring coherent effects. Using a full mapping of the transient response of an EIT system as a function of the detuning we observe the transition from an adiabatic regime to a non-adiabatic regime. We also measure the complex interference pattern that arises when a magnetic field is applied. In this case an interference between transients from three Zeeman sub-levels is visible. The problem of three level crossing in the context of LZ transitions was addressed both theoretically and experimentally [27, 63, 64, 83, 106]. Here we have the ability to change the levels energy gap experimentally implementing the three level crossing for variable level detuning. Moreover, we show that using this interference combined with broadband phase modulation sweep a wideband high sensitivity magnetometer can be achieved.

3.3.2 Theoretical frame - linear response theory

We now describe the effect a phase modulated strong coupling field has upon the temporal shape of a probe pulse going through an EIT media. The coupling field can be written as follows:

$$\mathbf{E_c}(t) = E_{c0}e^{(i\omega_c t - i\phi(t))}, \tag{3.3.1}$$

where E_{c0} is the amplitude of the coupling field, ω_c is the optical frequency and $\phi(t)$ is the time dependent phase modulation. In order to describe the change in the probe field due to this modulated coupling field the full spatio-temporal Maxwell-Bloch equations for an EIT system needs to be solved [89]. In the case of long enough interaction media and perturbative probe intensity the system can reach a steady state solution. The

EIT susceptibility in this case has only temporal and no spatial dependence. For a susceptibility with no temporal dependence the probe transmission amplitude, $p(t)$ is given by the convolution of the entering signal, $E_p(\omega)$, and the susceptibility, $\chi(\omega)$, hence $p(t) = \mathcal{F}[E_p(\omega)\chi(\omega)]$. In the case of a modulated field the susceptibility is time dependent, and this convolution is not valid. A possible way of solving this problem is by taking the spectral decomposition of the susceptibility $\chi(\omega, t) = \sum_{n=-\infty}^{\infty} e^{in\Omega t}\chi_n(\omega)$. Now the transmission is just $p(t) = \sum_{n=-\infty}^{\infty} e^{in\Omega t}\mathcal{F}[E_p(\omega)\chi_n(\omega)]$ [89]. We use a sinusoidal modulation, hence $\phi(t) = Msin(\Omega_c t)$ where M is the modulation depth and $\Omega_c = 2\pi f_c$ is the modulation frequency. The spectrum of such a modulated field can be described as a sum of Bessel functions

$$e^{-i\phi} = \sum_{n=-\infty}^{\infty} e^{in\Omega_c t} J_n(-M). \tag{3.3.2}$$

The spectrum of this modulation has narrow peaks separated by a frequency Ω_c with a full modulation span of $2M\Omega_c$. The transfer function in this case is just an infinite comb of single EIT lines [57] weighted by Bessel functions:

$$\chi(t) = \sum_{n=-\infty}^{\infty} i\alpha \frac{J_n(-M)e^{in\Omega_c t}}{\Gamma - i(\Delta - n\Omega_c) + \frac{R_c^2}{\gamma_{12} - i(\delta - n\Omega_c)}}. \tag{3.3.3}$$

Here $\alpha = \frac{N\mu^2}{\epsilon_0 \hbar}$ is the two-level absorption coefficient, with N the density of the atoms and μ is the transition dipole moment, Γ is the homogeneous decay rate, γ_{12} is the decoherence rate of the two ground states, $R_c = \frac{\mu E_{c0}}{\hbar}$ is the Rabi frequency of the coupling field which is phase modulated, Δ is the one photon detuning of the probe field and δ is the two photon detuning.

In the case of the D1 line of warm ^{87}Rb vapor with buffer gas the FWHM EIT linewidth is [50] $\gamma_{EIT} = 2(\gamma_{12} + \frac{R_c^2}{\Gamma_D + \Gamma})$ where Γ_D is the Doppler broadening. This linewidth is usually a few kHz which is much narrower than the pressure broadened homogeneous linewidth ($\Gamma \sim 100\, MHz$) and the Doppler broadening ($\Gamma_D \sim 500\, MHz$),

thus the probe two level susceptibility is effectively constant for the full modulation bandwidth as long as $M\Omega_c \ll \Gamma$.

Applying a magnetic field removes the Zeeman degeneracy and the energy levels of the hyperfine levels will create a ladder according to the Zeeman splitting of the two lower levels with a Larmor frequency $\mu_B B(g_F m_F - g_{F'} m_{F'})$. B here is the magnetic field, μ_B is the Bohr magneton and g_F is the Lande coefficient of the hyperfine level. The EIT susceptibility will be determined by the Zeeman splitting with several EIT peaks having a certain phase between them. We can write the transfer function as follows:

$$\chi(t) = \sum_{n=-\infty}^{\infty} \sum_{m_F=-F}^{F} \sum_{m_{F'}=-F'}^{F'} i\alpha \times \frac{J_n(-M)e^{in\Omega_c t}}{\Gamma - i(\Delta - n\Omega_c) + \frac{R_c^2}{\gamma_{12} - i(\delta - n\Omega_c - \mu_B B(g_F m_F - g_{F'} m_{F'}))}}. \tag{3.3.4}$$

3.3.3 Experimental setup

The experimental setup is shown in Fig. 3.3.1. For an EIT Λ scheme we use the hyperfine transitions of the D1 line of ^{87}Rb. A DFB laser locked to the $F = 2 \rightarrow F' = 2$ transition is split into probe and coupling beams using a polarizing beam splitter. The phase modulation over the coupling field as well as the pulse creation of the probe is done using AOMs. In order to bring the probe to resonance with the $F = 1 \rightarrow F' = 2$ transition an EOM is used. The beams (orthogonal polarization) are combined together using a Glan-Taylor polarizer and pass through a 7.5 cm cell containing an isotopically pure ^{87}Rb with 10 Torr Ne as buffer gas heated to $\sim 40°C$. The cell is shielded from an outside magnetic field using a 3-layers of μ-metal. An axial magnetic field is created using a uniform solenoid. After the cell another polarizer is used in order to filter the coupling field while the probe is detected using an amplified photodiode.

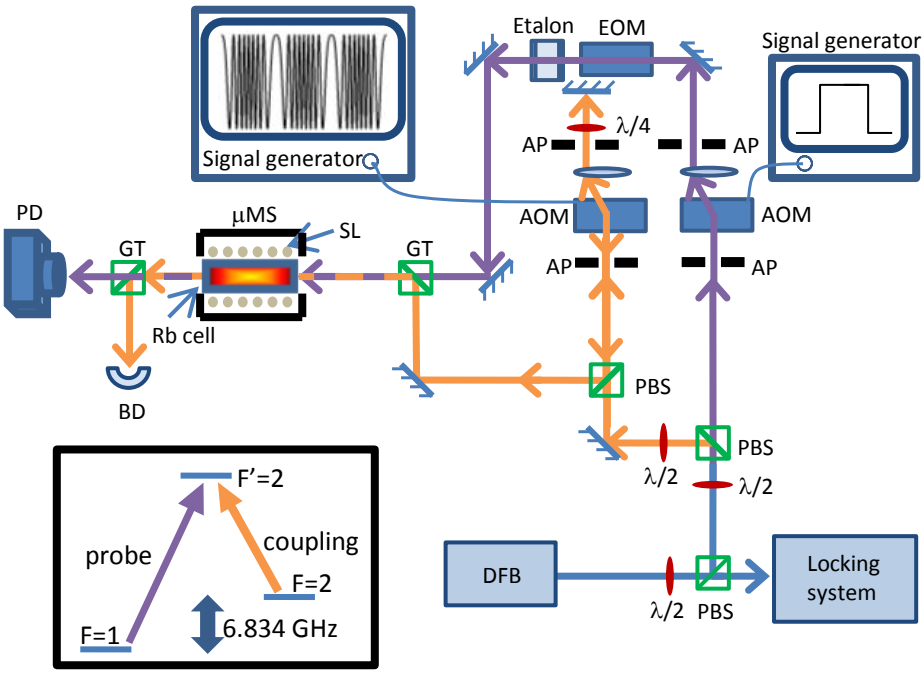

Figure 3.3.1: The experimental setup. DFB - distributed feedback laser, PBS - polarizing beam splitter, AP - aperture, AOM - acousto-optic modulator, EOM - Electro-optic modulator, GT - Glan-Taylor polarizer, μMS - μ- metal shield, BD - beam dump, PD - photodiode, SL - solenoid.

3.3.4 Results

Figure 3.3.2 demonstrates the transmission temporal response of a square probe pulse with intensity of 0.05 $\frac{mW}{cm^2}$ due to a phase modulated coupling field with intensity of 1 $\frac{mW}{cm^2}$ in an EIT media. Two major features are observed, one is a train of pulses that is created with a period and phase that is dependent upon the coupling field modulation frequency and the detuning [89]. The second feature is a transient ringing that is associated with the response of the media to a sudden change in the susceptibility. This ringing has a chirped frequency as expected [136]. It decays with a characteristic time that depends upon $^1/\gamma_{EIT}$ and the chirp rate through the transition. The instantaneous frequency of the coupling field due to the modulation is $\omega(t) = \omega_c + \frac{\partial\phi}{\partial t} = \omega_c + M\Omega_c cos(\Omega_c t)$ while the response has the spectral width of the EIT linewidth, thus the relation between the modulation frequency and the EIT width, sets the adiabaticity of the response.

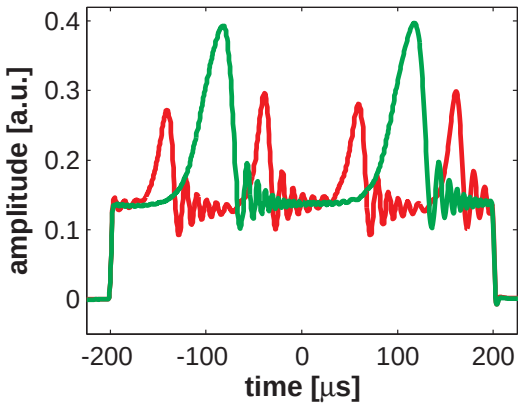

Figure 3.3.2: Transient oscillations of the probe amplitude due to coupling modulation with $f_c = 5\,kHz$ and $M = 20$. Red - $\delta = 0$, green - $\delta = 100\,kHz$.

Figure 3.3.3 shows experimentally and theoretically the transition between the adiabatic regime where the modulation frequency is lower than the EIT linewidth ($\Omega_c \ll \gamma_{EIT}$) and the non-adiabatic regime where $\Omega_c \gg \gamma_{EIT}$. For both regimes the phase of the pulses is determined by the instantaneous frequency hence we see a sine like plot as a function of the detuning with a period $1/\Omega_c$ and an amplitude $M\Omega_c$. In the adiabatic regime the transients decay fast enough so they are hardly noticeable, but as the modulation frequency become comparable to the EIT linewidth [Fig. 3.3.3(b)] the transient ringing is clearly observed. In the non-adiabatic regime the modulation frequency is faster than the decay of the transient ringing creating an interference between consecutive pulses as can be observed in Fig. 3.3.3(c). Simulation of these 2D patterns using Eq. 3.3.3 are depicted in Fig. 3.3.3(c-e) showing a striking similarity to the results. One aspect this linear response theoretical simulation fails to take into account is the smearing of the interference pattern when the probe pulse is turned on as can be visualized particularly in Fig. 3.3.3(c). The cause of this effect is the gradual build up of the dark state polariton and consequently the creation of the EIT line that has a characteristic time of $1/2\pi\gamma_{EIT}$ [121]. Integrating the time domain reveals the steady state spectrum of the probe light. Figure 3.3.3(f-h) shows the integrated spectra of the experimental data (green line) as well as the simulation (red line) in the adiabatic and non-adiabatic regimes. These spectra fit to the phase modulation

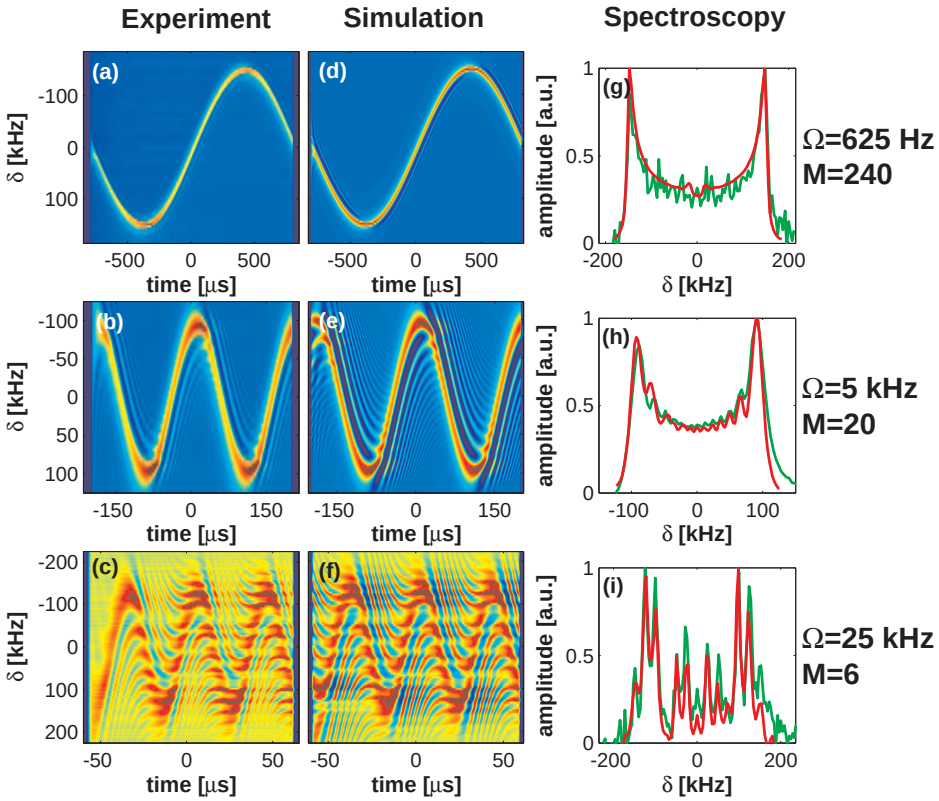

Figure 3.3.3: Adiabatic to non-adiabatic transition. 2D mapping of the spectro-temporal response of the probe pulse is demonstrated in the case of (a) adiabatic regime, (b) intermediate regime and (c) non-adiabatic regime. The parameters of the modulation are (a) $f_c = 625\,Hz$ and $M = 240$, (b) $f_c = 5\,kHz$ and $M = 20$, (c) $f_c = 25\,kHz$ and $M = 6$. All the experiments are done with $\gamma_{EIT} = 14\,kHz$. Plots (d-f) show a simulation of the three regimes that takes into account Eq. 3.3.3 with the parameters written above. Plots (g-i) show the spectrum of the transmission taken as the time integral for each frequency. Green - experimental spectrum, red - simulation spectrum.

spectrum according to the Fourier of Eq. 3.3.2, meaning a delta functions separated by the modulation frequency, broadended due to the finite EIT linewidth. Another way of thinking about the interference shown in Fig. 3.3.3(c) is as a Landau-Zener-Stuckelberg interference pattern where a transition is crossed repetitively faster than the transient decay time [153].

Figure 3.3.4 shows a 2D mapping of the temporal response of the probe for different magnetic fields (The two photon detuning is on resonance with the magnetic insensitive transition). In the adiabatic regime (Fig. 3.3.4(a)) it is possible to see a splitting of

the sole pulse in B=0 into three pulses. These pulses correspond to three EIT lines that are present in the spectrum. For the D1 line of rubidium, using an arbitrary magnetic field, up to 7 EIT lines may appear [33]. Due to the vectorial nature of the magnetic interaction, the relative strength of these lines depends on the angle between the beam direction and the magnetic field as well as the polarization of the pump and probe beams [193]. The specific configuration we use in our setup is $\mathbf{B} \parallel \mathbf{k}$ with linear polarization. In this case only three lines appear in the spectrum [193, 198] as can be seen experimentally 2.5.5. The central pulse matches the $\Delta m = 0$ and thus its phase is constant, while the other two pulses correlate with the $\Delta m = \pm 2$, hence having a sinusoidal phase shift. Figures 3.3.4(b-c) show the non-adiabatic regime where every pulse has an oscillating tail with a certain phase causing an interference pattern. A simulation based on Eq. 3.3.4 is shown in Fig. 3.3.4(d-f) having the same basic features of the experimental results.

The observed interference may be understood in the following way. In the case of hyperfine EIT in a buffer gas and under the condition of $\gamma_{EIT} \ll \Gamma$ it is possible to treat the two ground states as a degenerate set of effective two level systems (TLS) [178, 185]. Adding a magnetic field removes the degeneracy and splits each TLS according to the Zeeman frequency [167]. In our case due to the selection rules stated above the splitting is to three groups with $\Delta m = 0, \pm 2$. As a consequence of this picture it is possible to think of the magnetic sweep in time as a chirp of the three TLS's. (as depicted by the black dashed lines in Fig. 3.3.4(a)) . Thus, the interference we measure is a direct consequence of a three-level degeneracy. It is important to notice that in EIT, due to the strong coupling field, the population remains in the dark state all the time and the measured interference is not a three level LZ population transition but rather a coherence measurement. A more intuitive way of describing the LZ dynamics in our system is presented in 3.3.6.

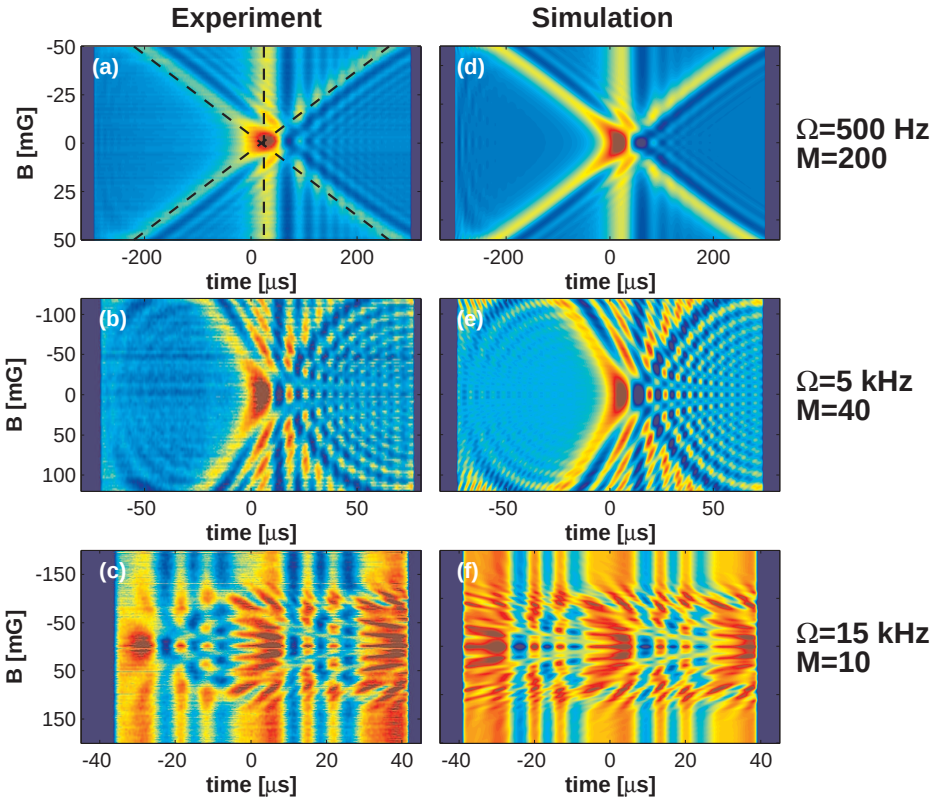

Figure 3.3.4: Temporal response of a probe pulse due to magnetic field for (a) adiabatic regime, (b) intermediate regime and (c) non-adiabatic regime. The parameters of the modulation are (a) $f_c = 500\,Hz$ and $M = 200$, (b) $f_c = 5\,kHz$ and $M = 40$, (c) $f_c = 15\,kHz$ and $M = 10$. Plots (d-f) show a simulation of the three regimes that takes into account Eq. 3.3.4 with the parameters written above.

3.3.5 Wideband magnetic sensing

The dynamic pattern created by the phase modulation can be used for broadband magnetic sensing. Each magnetic field has a certain characteristic pulse timing associated with it. The phase of the first pulse is a prominent feature for broad magnetic sensing as the total amplitude of the modulation is $B_{max} = {}^{M\Omega}/_{\Delta m \mu_B g_F}$. This corresponds to $142\,mG$ and $107\,mG$ for 3.3.4(b) and 3.3.4(c) respectively. Moreover, the interference pattern offers a way of measuring accurately the magnetic field in the area of the interference. The sensitivity to magnetic field is dependent upon the signal (S) to noise ($\widetilde{N}$) ratio and given by [17]

$$\frac{\Delta B}{\sqrt{\Delta\nu}} = \frac{\sqrt{t}}{S/\widetilde{N}} = \frac{\sqrt{t}\widetilde{N}}{\partial A/\partial B} \tag{3.3.5}$$

Where t is the measurement time and $\partial A/\partial B$ is the gradient of the integrated measured amplitude and the magnetic field. In our case, since the transient ringing is a complex multi frequency feature the best way to characterize the transients for different magnetic field is by using the correlation between them

$$A(B) = M(t,B)^T M(t,B). \tag{3.3.6}$$

Using this method we measured the noise and the gradient of the correlation function and estimate our sensitivity to be $1\frac{nT}{\sqrt{Hz}}$ for the 5 kHz modulation and $0.2\frac{nT}{\sqrt{Hz}}$ in the case of 15 kHz. This sensitivity is similar to the one reported using multimode EIT by Belfi et al. [17]. The ultimate sensitivity for a given system is [25] $\frac{\delta B}{\sqrt{Hz}} = \frac{\hbar}{\mu_B g_F}\sqrt{\frac{2\pi\gamma_{EIT}}{NV}}$ where V is the volume of the magnetometer. In our case this sensitivity is $\sim 400\frac{fT}{\sqrt{Hz}}$ well below the measured sensitivity. The main reason for that is the electrical noise in the detector and amplifier which is used in order to observe the data in the oscilloscope. Better electronics may allow at least one order of magnitude improvement.

A different way of evaluating the sensitivity of our method is by analyzing the interferogram created by the multi level interference as can be seen for example in Fig. 3.3.4(b). Simulation shows that the width of the central peaks (around B=0) narrows linearly as the number of Zeeman levels participating in the interference grows, meaning higher interferometric sensitivity. A similar effect of multi Zeeman sublevels interference was measured in cold atoms yielding a corresponding enhancement in the sensitivity [138].

3.3.6 Dressed states interpretation

The ringing observed in Fig. 3.3.2 is a manifestation of a non-adiabatic transition through the EIT resonance. LZ theory deals with this kind of transitions and gives

analytic prediction to the population transfer between the levels. In the case of an EIT in buffer gas the best way to describe the system is using the dressed states picture. Taking the Hamiltonian of the bare three levels under the rotating wave approximation

$$\begin{pmatrix} 0 & 0 & \frac{1}{2}R_p^* \\ 0 & \delta & \frac{1}{2}R_c^*(t) \\ \frac{1}{2}R_p & \frac{1}{2}R_c(t) & \Delta \end{pmatrix} \tag{3.3.7}$$

where $R_c(t) = R_{c0}e^{-i\phi(t)}$, R_p are the Rabi frequencies of the coupling and the probe fields respectively, δ is a constant two photon detuning and Δ is one photon detuning (in the case relevant to us $\Delta = 0$). In order to see the resemblance to the LZ case it is instructive to change to a new basis where

$$\begin{aligned} |1\rangle' &= |1\rangle \\ |2\rangle' &= |2\rangle\, e^{-i\phi(t)} \\ |3\rangle' &= |3\rangle\, e^{i\phi(t)} \end{aligned} \tag{3.3.8}$$

The new Hamiltonian will become

$$\begin{pmatrix} 0 & 0 & \frac{1}{2}R_p^* \\ 0 & \delta - \frac{1}{2}\frac{\partial\phi}{\partial t} & \frac{1}{2}R_{c0}^* \\ \frac{1}{2}R_p & \frac{1}{2}R_{c0} & \frac{1}{2}\frac{\partial\phi}{\partial t} \end{pmatrix}. \tag{3.3.9}$$

The 2×2 matrix of levels $|2'\rangle$ and $|3'\rangle$ is a LZ Hamiltonian. Under EIT conditions $R_c \gg R_p$ it is possible to diagonalize this 2×2 matrix obtaining two new dressed levels with eigenvalues $\epsilon_\pm = -\frac{1}{2}\delta \pm \frac{1}{2}\sqrt{\delta^2 + R_{c0}^2 + (\frac{\partial\phi}{\partial t})^2 - 2\frac{\partial\phi}{\partial t}\delta}$. In the simple case where $\delta = 0$ these states are just $|+\rangle = \sin\theta\,|2'\rangle + \cos\theta\,|3'\rangle$ and $|-\rangle = \cos\theta\,|2'\rangle - \sin\theta\,|3'\rangle$ with $\tan 2\theta = {}^{R_{c0}}\!/_{\frac{\partial\phi}{\partial t}}$ [163]. It is important noticing that no actual population is being transferred between the two levels since only level $|1\rangle$ is populated at all times. This two dressed states dynamics is interrogated by the probe field, meaning that the transition matrix element $|1\rangle \rightarrow |3\rangle$ we are measuring in the experiment, drives the dynamics

described above as depicted in Fig. 3.3.5(a). In our experiment a phase modulation sweep in time causes a periodic crossing between the two dressed levels.

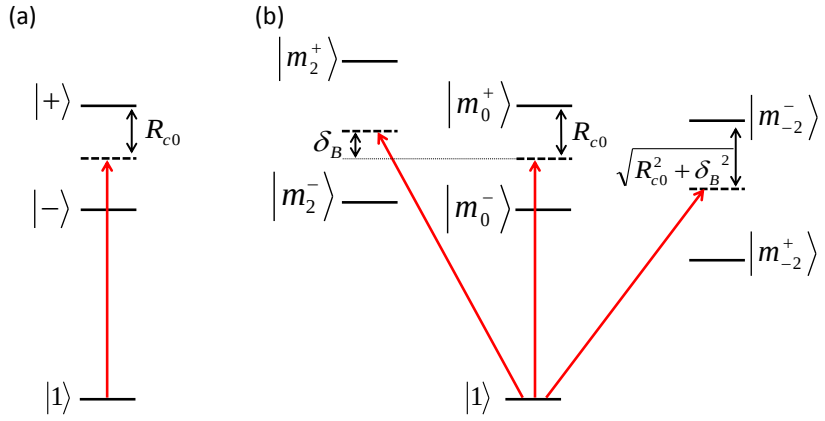

Figure 3.3.5: Dressed states (on two photon resonance ($\delta = 0$)) for (a) no magnetic field (b) with magnetic field. Red arrows represent probe transition on resonance.

When a magnetic field is applied the system is split into three sub-systems with three levels in each one of them [167]. Each one of these sub-systems behaves exactly as a single EIT system with the exception of a magnetic Zeeman shift $\mu_B B(g_F m_F - g_{F'} m_{F'})$. As a consequence the energy levels of the sub-systems $\Delta m = +2$ and $\Delta m = -2$ are reversed with respect to the magnetic field (with $\delta = 0$) while the energy levels of the sub-systems $\Delta m = 0$ is degenerate up to the interaction avoided level crossing as depicted in Fig. 3.3.5(b).

One interesting characterization of the LZ transition is the transition time. This time can be measured by the decay time of the oscillations after the transition [177]. The two parameters that determine the transition's properties is the coupling Rabi frequency and the chirp rate, defined as $\frac{\partial^2 \phi}{\partial t^2}$. In the case of sinusoidal phase modulation,

where $\phi(t) = Mcos(\Omega t)$, the chirp rate at $\delta = 0$ is $\frac{\partial^2\phi}{\partial t^2} = M\Omega^2$. It is useful to define the transition using a dimensionless parameter $\beta = \frac{R_c}{\sqrt{\partial^2\phi/\partial t^2}} = \frac{R_c}{\sqrt{M\Omega}}$. Figure 3.3.6 shows the decay time, τ, as a function of β for our experimental results (red squares) as well as for our simulation results (black circles). The relaxation time is found from an exponential fit to the ringing peaks as depicted in the inset in Fig. 3.3.6.

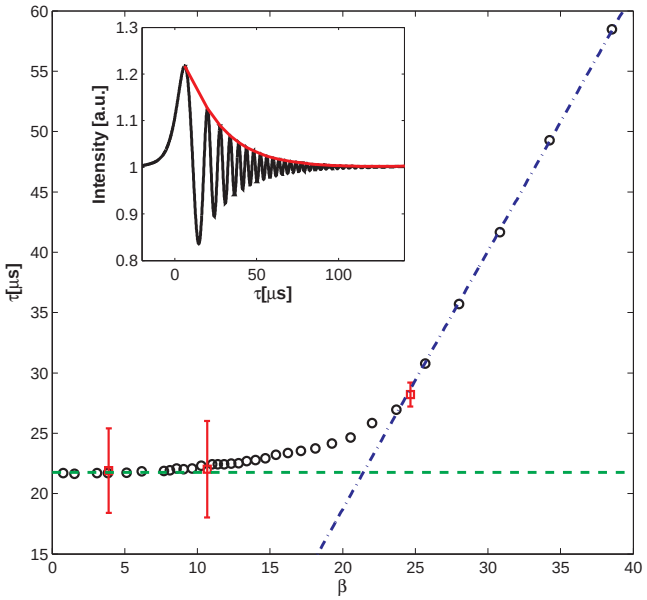

Figure 3.3.6: Decay time of the ringing at as a function of β. Black circles - simulation, red squares - experiment. The decay time is calculated using an exponential fit to the peaks of the ringing as shown in the inset. Green dashed line - the EIT decay according to $\frac{2}{2\pi\gamma_{EIT}}$. Blue dash dotted line - linear fit for the adiabatic case. Simulation parameters are similar to the one in Fig. 3 with variable modulation index and modulation frequency.

The probability of a LZ transition (without decoherence) with respect to time is a parabolic cylinder function that can be approximated in the case of the relaxation time to a chirped oscillatory function multiplied by some polynomial decay [177]. Adding decoherence will add an exponential decay to the LZ relaxation. Our fit is indeed not to the full function, but to an exponential decay, which allows a qualitative estimation for the LZ relaxation as a function of β. We see that in the diabatic limit (low β) the decay time is nearly constant and converging towards $\frac{2}{2\pi\gamma_{EIT}}$, meaning LZ relaxation which is much longer than decoherence relaxation. At the adiabatic limit (high β) the

decay is linear with β. Similar theoretical results for the LZ theory have been reported before [125, 177], but with different scaling of β.

3.3.7 Conclusion

We present a method for measuring broadband coherent effects using the transient dynamics of a strongly modulated system. Specifically, we show the transient response of an EIT media to a phase modulated pump. This response reveals explicitly the coherent nature of the EIT susceptibility. In the non-adiabatic regime where EIT peaks are spectrally resolved we clearly observe interference between the different modes. Albeit the interference between these modes does not contribute to EIT spectral narrowing and as a consequence to a slower light propagation [26, 73], it does create a transient behavior useful for broadband data transfer. Applying a magnetic field splits the EIT line into three, allowing us to see an interference pattern dynamics caused by three levels LZ crossing. Along with the wideband sweep due to the high modulation index it is shown to be a useful tool for sensitive wideband magnetometry.

3.4 Heralded entanglement using atomic vapor

3.4.1 Introduction

All previous sections dealt with semi classical systems in the sense that the atoms were treated quantum mechanically but light was treated classically. Here we present a theoretical framework and results of a purely quantum process, heralded entanglement using atomic vapor. Entanglement is a unique property of quantum multisystems, where the state of one system is not independent on the others [135]. Entanglement serves as the main tool in fundamental research of quantum theory as well as in the rapidly-developing area of quantum information [81]. Photons are prominent quantum systems due to their weak interaction with the environment which increase their immunity to decoherence. On the other hand, this weak interaction makes the creation of an entangled state of photons a difficult task that usually requires a very high nonlinearity.

In the early days of quantum optics sources of entanglement were atomic cascades [12], but nowadays the main source for entangled photons is the nonlinear process of spontaneous parametric down conversion (SPDC). This is an efficient source that can create polarization [97] or time-bin entanglement [98], but has two major drawbacks for efficient quantum communication schemes. Namely, it is not deterministic and has a broadband spectrum. Deterministic single photon sources include quantum dots, single atoms in a cavity and atomic ensembles [47, 95]. Atomic ensembles offer another asset, which is the generation and storage of a single photon in a heralded way. This is the main building block for a quantum repeater as proposed in the DLCZ protocol for long range quantum communication ([40, 148] and Sec. 1.4.2). Single photon storage times of up to a few ms were observed using trapped Rubidium ensembles [194, 196] and a few tens of μs using warm vapor [15, 174]. Moreover, the ability to store a multi photon entangled state from an SPDC source was also shown [31, 34].

Recently, several alternatives to SPDC as an entanglement source were presented. Quantum dot biexcitons were developed as an efficient source for entangled photons

that can be created in a triggered way [4, 166]. Using a single quantum dot ensures a single pair of entangled photons, but the yield up until now is not high compared to SPDC. Moreover the photons are emitted together and are still broadband with respect to the needs of quantum repeaters [148]. New schemes of exploiting atomic media as an entanglement source were also presented. One proposal uses a double-Λ level configuration for a deterministic entanglement of N photons [65]. This procedure suffers mostly from the difficulty of working with one atom in a cavity. Another promising direction for an entangled photon source is the use of non linear effects in atomic ensembles such as four wave mixing [114, 161] and Rydberg blockade [127, 140]. Porras and Cirac suggested a use of an excited symmetric spin wave in double Λ atoms as a way to entangle photons in a deterministic way [140].

Here we take this idea in a different direction and apply it in an atomic ensemble. We utilize single photon quantum storage in atomic gases combined with the property of Zeeman splitting of hyperfine manifolds in order to create a heralded polarization entanglement. The scheme relies on using the magnetic Zeeman levels as an effective polarization beam splitter for single photons in order to entangle the two photons. This source creates two polarization entangled photons that are distinguished in time and have a narrow bandwidth that can be suitable for quantum communication [183]. We show the dependence of the fidelity and pair production rate upon the detection efficiency. In section 3.4.2 the general scheme of the entanglement process is described. Section 3.4.3 discusses the practical limitations of the scheme and how the fidelity and production rate of the entangled pair is affected by them. Section 3.4.4 shows some preliminary results showing none classical single photons and Section 3.4.5 gives some concluding remarks.

3.4.2 General Scheme

The general sequence for creating heralded entanglement is presented schematically in Fig. 3.4.1. As the source for entanglement we use an atomic ensemble with N atoms.

Each atom has a Λ configuration energy level scheme. Each energy level should contain its own Zeeman sublevel manifold, such as a hyperfine splitting with F>0. Without loss of generality we will concentrate here on the case where the long lived ground state $|g\rangle$ has a hyperfine level with F=1, the long lived metastable level, $|s\rangle$ has a hyperfine level with F=2 and the excited state $|e\rangle$ is F'=2. One specific example that fits to this case is the D1 transition of ^{87}Rb. Each hyperfine level has Zeeman sublevels that becomes non degenerate when applying a magnetic field. A schematic picture of the relevant levels is depicted in figure 3.4.2. Using a circular polarized pumping it is possible to transfer all the population to the F=1, $m_s = -1$ level which is the $|g^-\rangle$ state. The collective state of the atoms and light can be written as follows :

$$|\Psi_0\rangle = \left|g^-\right\rangle^N |0\rangle\,, \tag{3.4.1}$$

where $|0\rangle$ is the state of zero photons in a defined spatial and spectral mode. This mode will be defined later as the Stokes or anti Stokes (AS) mode.

Immediately after the pumping, a weak and short write pulse with a circular σ^+ polarization is applied to the ensemble. The laser detuning should be large enough in order for the main atom light interaction to be a spontaneous Raman transition to the $|s\rangle$ state. Since the circular polarization dictates a transition to the Zeeman sublevel $|e, m_s = 0\rangle$, the spontaneous Raman decay can be to levels $|s, m_s = 0, \pm 1\rangle$, but since F = F$'$ the transition to $|s, m_s = 0\rangle$ is forbidden and the other two sublevels have the same probability [2] . Thus, upon a successful detection of one photon in one of the polarizations σ^+ or σ^-, the spin state of the metastable level will become $|s, m_s = -1\rangle$ or $|s, m_s = +1\rangle$ respectively. If for example the detected photon is σ^+ then the collective state will be

[2] In real schemes the probability for the two polarizations can be different due to spontaneous Raman emission from a second hyperfine excited level. Effectively, it lowers the rate of entanglement creation, but does not harm the fidelity of the state. For more details see [182].

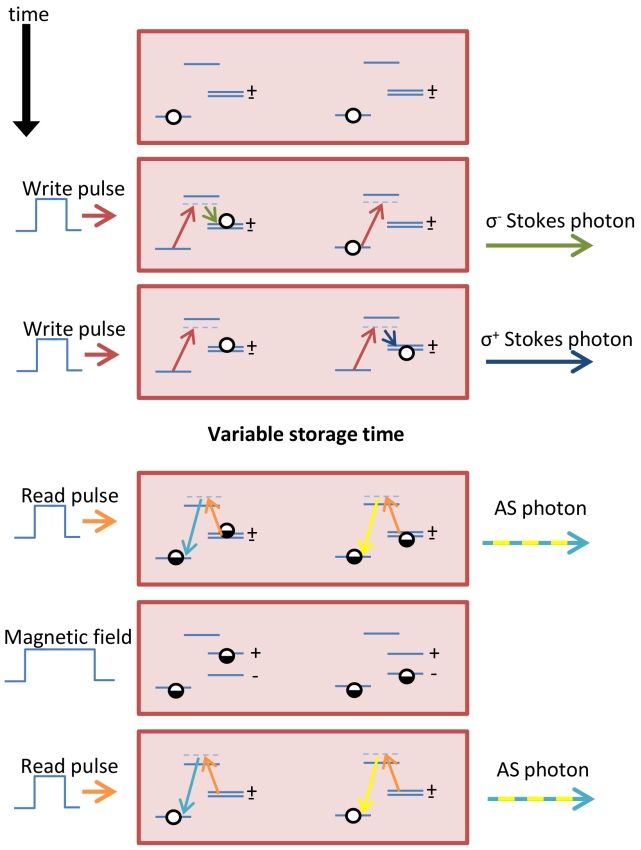

Figure 3.4.1: Schematics of the experiment. Each of the two atoms shown represents one of the N states in the sum of the Dicke state.

$$|\Psi_{s1}\rangle = \frac{1}{\sqrt{N}} \sum_{i=1}^{N} e^{i(\mathbf{k_w}-\mathbf{k_s})\mathbf{x_i}} \left|s_i^-\right\rangle |+_s\rangle \,, \tag{3.4.2}$$

where $\left|s_i^-\right\rangle$ means that the ith atom is now at the state $|s, m_s = -1\rangle$ while all other atoms are in the ground $|g^-\rangle$ state. $|+_s\rangle$ means a Stokes photon with σ^+ polarization is emitted, $\mathbf{k_w}$ is the write laser wave vector, $\mathbf{k_s}$ is the Stokes photon wave vector and $\mathbf{x_i}$ is the coordinate of the ith atom.

The atomic state is in a Dicke-like state [36]. This is a long lived atomic coherence where the main decoherence process is the atomic motion that can change the phases between the different atomic states [39]. In the following, we will assume no motion, meaning that these phases do not alter during the storage time. In this case, upon

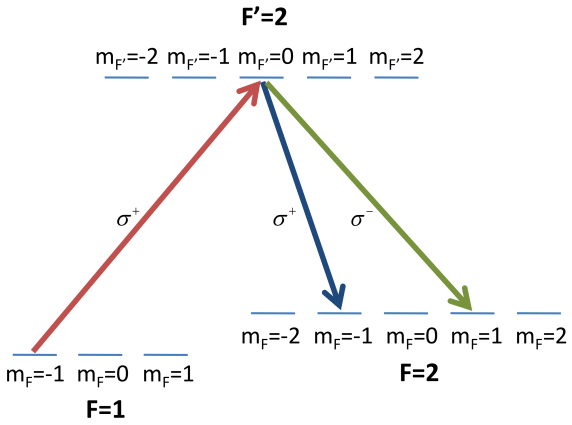

Figure 3.4.2: The possible alternatives for single Stokes photon generation during the write process. Red arrow - write beam, Green and blue arrows - Stokes photons.

applying a read pulse with a perfect phase matching condition $\mathbf{k_w} + \mathbf{k_r} = \mathbf{k_s} + \mathbf{k_{as}}$, a constructive interference in the direction of the AS wave vector will cause this mode to dominate all other directions [148]. Thus, in the case of no atomic motion and perfect phase matching, the phase terms just sum up to unity so it is possible to omit them from now on.

Now it is possible to quickly repeat the write pulse in order to create another excitation in the metastable state (of course, this pulse will create an excitation only with low probability, but since it is a heralded scheme, we are looking only upon successful events). Let us concentrate on the events where the second Stokes photon that is emitted has the opposite polarization than the first one, thus the collective state will be now

$$|\Psi_{s2}\rangle = \frac{1}{\sqrt{2N(N-1)}} \sum_{i\neq j=1}^{N} \left|s_i^- s_j^+\right\rangle |+_s -_s\rangle \,. \tag{3.4.3}$$

Practically, since the temporal phase between the two Stokes photons is not important, it is possible to use one long write pulse with the same excitation probability instead of two separate pulses (see section 3.4.3 for further discussion).

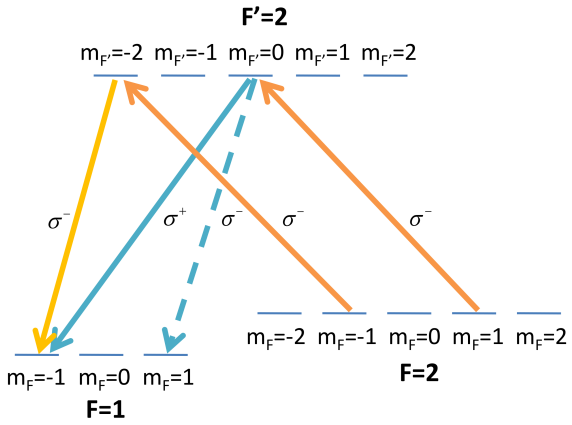

Figure 3.4.3: The possible alternatives for single AS photon generation during the read process. orange arrows - read beam, blue, dashed blue and yellow arrows - AS photons.

After a certain storage time, a σ^- polarization read pulse is sent into the media. This pulse can interact with one of the excited Dicke states releasing, with some probability, one AS photon. There are two possibilities, one that the atoms are in the $|s, m_s = +1\rangle$ state and one that the atoms are in the $|s, m_s = -1\rangle$ state. Each of these options can produce different AS single photons as described in Fig. 3.4.3. The AS transition strengths may not be the same due to different Clebsch–Gordan coefficients, thus there is a need to multiply each transition with the proper probability amplitude denoted by $P_{kl}^{(\mathrm{F})}$ where k is the Zeeman sublevel of the excited state, l is the Zeeman sublevel of the ground state and F is the hyperfine level of the ground state.

The AS photon polarization is correlated with the atomic spin level that remains in the ensemble and the state becomes

$$|\Psi_{as1}^{0}\rangle = \frac{1}{\sqrt{2N(N-1)}} \sum_{i\neq j=1}^{N} P_{0,1}^{(2)} \left|s_i^-\right\rangle \left(P_{0,-1}^{(1)} \left|g_j^-\right\rangle |+_{as}\rangle + P_{0,1}^{(1)} \left|g_j^+\right\rangle |-_{as}\rangle \right) + P_{-2,-1}^{(2)} P_{-2,-1}^{(1)} \left|s_i^+\right\rangle \left|g_j^-\right\rangle |-_{as}\rangle \,, \tag{3.4.4}$$

where $|g^-\rangle$ and $|g^+\rangle$ are the relaxation of the first AS photon to the Zeeman ground state sublevels $m_F = -1$ or $m_F = +1$ respectively.

Now a magnetic field is applied to the ensemble creating a Zeeman splitting of the $|s\rangle$, $|g\rangle$ states. The two Zeeman levels will acquire a different phase during the single excitation storage time according to the energy splitting. For an energy splitting ω_m in the $|s\rangle$ level and ω_n in the $|g\rangle$ level and after a storage time τ the state will become

$$\begin{aligned}|\Psi^{\tau}_{as1}\rangle \quad = \quad & \frac{1}{\sqrt{2N(N-1)}}\sum_{i\neq j=1}^{N} P^{(2)}_{0,1}e^{-i\omega_m\tau}\left|s_i^-\right\rangle \\ & \times\left(P^{(1)}_{0,-1}e^{-i\omega_n\tau}\left|g_j^-\right\rangle|+_{as}\rangle + P^{(1)}_{0,1}e^{i\omega_n\tau}\left|g_j^+\right\rangle|-_{as}\rangle\right) \\ & +P^{(2)}_{-2,-1}P^{(1)}_{-2,-1}e^{i(\omega_m-\omega_n)\tau}\left|s_i^+\right\rangle\left|g_j^-\right\rangle|-_{as}\rangle\,. \end{aligned} \tag{3.4.5}$$

Sending another read pulse strong enough to create a second AS photon will produce the following state [3]:

$$\begin{aligned}|\Psi^{\tau}_{as2}\rangle \quad = \quad & \frac{\alpha}{\sqrt{2N(N-1)}}\sum_{i\neq j=1}^{N} e^{-i\omega_m\tau}\left(P^{(1)}_{0,1}e^{i\omega_n\tau}\left|g_j^+\right\rangle^A|-_{as}\rangle^A + P^{(1)}_{0,-1}e^{-i\omega_n\tau}\left|g_j^-\right\rangle^A|+_{as}\rangle^A\right)\left|g_i^-\right\rangle^B|-_{as}\rangle^B \\ & +e^{i(\omega_m-\omega_n)\tau}\left(P^{(1)}_{0,-1}\left|g_i^-\right\rangle^B|+_{as}\rangle^B + P^{(1)}_{0,1}\left|g_i^+\right\rangle^B|-_{as}\rangle^B\right)\left|g_j^-\right\rangle^A|-_{as}\rangle^A\,, \end{aligned} \tag{3.4.6}$$

where the A, B notations represent the emitted AS photon during the first or second read pulse respectively and $\alpha = P^{(2)}_{0,1}P^{(2)}_{-2,-1}P^{(1)}_{-2,-1}$. For simplicity in the following we will abbreviate $|-_{as}\rangle^A|-_{as}\rangle^B \equiv |--\rangle$ etc., hence the state can be written as

[3] We assume here that the AS photon extraction probability is sufficiently bellow unity. If this is not the case, corrections are needed for eq. (3.4.6) due to a breaking of the symmetry between the extraction probabilities of the first and the second AS photons and the final state is no longer maximally entangled.

$$
\begin{aligned}
|\Psi^{\tau}_{as2}\rangle \quad = \quad & \tfrac{\alpha}{\sqrt{2N(N-1)}} \sum_{i\neq j=1}^{N} e^{-i(\omega_m+\omega_n)\tau} P^{(1)}_{0,-1} \left|\mathrm{g}^{-}_{j}\,\mathrm{g}^{-}_{i}\right\rangle |{+}{-}\rangle \\
& + e^{-i(\omega_m-\omega_n)\tau} P^{(1)}_{0,1} \left|\mathrm{g}^{+}_{j}\,\mathrm{g}^{-}_{i}\right\rangle |{-}{-}\rangle \\
& + e^{i(\omega_m-\omega_n)\tau} P^{(1)}_{0,-1} \left|\mathrm{g}^{-}_{j}\,\mathrm{g}^{-}_{i}\right\rangle |{-}{+}\rangle \\
& + e^{i(\omega_m-\omega_n)\tau} P^{(1)}_{0,1} \left|\mathrm{g}^{-}_{j}\,\mathrm{g}^{+}_{i}\right\rangle |{-}{-}\rangle \,. \qquad (3.4.7)
\end{aligned}
$$

Since there is a sum over all the ensemble, the time ordering may be switched and different indices for the atoms can be dropped. As $|\mathrm{g}^{-}\rangle$ is just the ground state it can be omitted from the equation and we get

$$
\begin{aligned}
|\Psi^{\tau}_{as2}\rangle \quad = \quad & 2\alpha P^{(1)}_{0,1} \cos[(\omega_m-\omega_n)\tau]\,|{-}{-}\rangle \left(\frac{1}{N}\sum_{i=1}^{N}\left|\mathrm{g}^{+}_{i}\right\rangle\right) \\
& + \alpha P^{(1)}_{0,-1}\left(e^{i(\omega_m-\omega_n)\tau}\,|{-}{+}\rangle + e^{-i(\omega_m+\omega_n)\tau}\,|{+}{-}\rangle\right). \qquad (3.4.8)
\end{aligned}
$$

Let us normalize the state for every storage time, thus the normalized state will be (taking into account that $P^{(1)}_{0,1} = P^{(1)}_{0,-1}$)

$$
\begin{aligned}
|\Psi^{\tau}_{as2}\rangle \quad = \quad & \sqrt{2}\frac{\cos[(\omega_m-\omega_n)\tau]}{\sqrt{2\cos^2[(\omega_m-\omega_n)\tau]+1}}\,|{-}{-}\rangle \left(\frac{1}{N}\sum_{i=1}^{N}\left|\mathrm{g}^{+}_{i}\right\rangle\right) \qquad (3.4.9) \\
& + \frac{1}{\sqrt{2}}\frac{1}{\sqrt{2\cos^2[(\omega_m-\omega_n)\tau]+1}}\left(e^{i(\omega_m-\omega_n)\tau}\,|{-}{+}\rangle + e^{-i(\omega_m+\omega_n)\tau}\,|{+}{-}\rangle\right).
\end{aligned}
$$

The second term is actually a generalized Bell state. The most interesting case will be for storage time where the phase is $(\omega_m-\omega_n)\tau = \pi/2$. In this case the first term vanishes and the photonic state is just a rotated maximally entangled Bell state $|\Psi'\rangle = \frac{1}{\sqrt{2}}\left(|{-}{+}\rangle + e^{i\phi}\,|{+}{-}\rangle\right)$.

3.4.3 Practical issues

The previous section dealt with an ideal case. For real applications two main issues should be addressed, the coherence time and the fidelity of the process due to detection imperfections.

Coherence

In order for the scheme to succeed the coherence time of the collective state of the atoms should be much longer than the experiment time. A typical coherence can reach up to 1 ms in cold atoms and a few hundred μs in warm vapor [194]. In warm vapor the spatial coherence of the collective spin state limits the lifetime. Measurements in rubidium of single photon storage reveal a quantum nature up to 5 μs [15]. We need to take a much shorter time for the magnetic field stage. On the other hand, the needed peak amplitude of the magnetic field should not be to high in order for a switching mechanism to work. A 100 ns magnetic pulse for example will cause a substantial phase shift if the the frequency will be on the order of 10 MHz ($\omega t \sim 1$) meaning a magnetic field of $\sim$10 G (In rubidium the Zeeman splitting is $\sim 0.5 - 1$ MHz/G). Switching on and off such a field with a 100 ns time scale is achievable.

Fidelity

The fidelity of the entangled state is affected by three major contributions. The first one is having only two excited Stokes photons and one excited AS photon per read pulse, the second one is the detection efficiency and the third one is the detector's dark counts [148]. In general, for spontaneous Raman scattering the state after a write pulse can be written as

$$\begin{aligned} |\Psi\rangle &= \sqrt{P_\lambda(0)}\,|e\rangle\,|0_s\rangle + \sqrt{P_\lambda(1)}\frac{1}{\sqrt{N}}\sum_{i=1}^{N}|s_i\rangle\,|1_s\rangle \\ &\quad +\sqrt{P_\lambda(2)}\frac{1}{N}\sum_{i=1}^{N}\sum_{j=1}^{N}|s_i s_j\rangle\,|2_s\rangle + ..., \end{aligned} \tag{3.4.10}$$

where $P_\lambda(n)$ is the probability of exciting n atoms in the specific mode and $|n_s\rangle$ is a state with n Stokes photons. For low excitation number each excitation is independent, thus this probability will have a Poisson distribution defined by parameter λ, which is the average excitation number. In order to have only two excitations, at most, due to the write process we need to use a weak pulse such that $P_\lambda(0) \gg P_\lambda(1) \gg P_\lambda(2)$. Two Stokes photons can be produced via two processes: two photons in one of the pulses and zero in the second and one photon in each write pulse. For our experiment both options are fine, as long as the two photons can be detected separately and the creation of three photons is negligible. Moreover, each photon is detected with a lower probability due to detectors efficiencies, fiber couplings, and filters. This lower detection efficiency may cause, for example, three photons to be detected as two, thus the probability of detecting only two photons while exciting n atoms will be

$$P_{det}(n,2) = \begin{pmatrix} n \\ 2 \end{pmatrix} \times P_\lambda(n) \times P_{detector}^2 \times (1 - P_{detector})^{n-2}, \tag{3.4.11}$$

where $P_{detector}$ is the detection efficiency. In the case two photons are created the probability to detect them will be in our case $P_{det}(2,2) = P_\lambda(2) \times P_{detector}^2$. Dark counts also contribute to lower the fidelity by adding a false detected photon. The probability for one dark count per pulse up to first order will be

$$P_{dark}(1) = P_\lambda(0) \times P_{dc} + P_\lambda(1) \times (1 - P_{detector}) \times P_{dc}, \tag{3.4.12}$$

where P_{dc} is the probability for a dark count per pulse that is related to the length of the pulse.

In order to quantify the total fidelity of the state created and the rate of successful events we assume a post selected measurement where we measure one AS photon after each read pulse. In this case a successful event is regarded as an event where two Stokes photons are created and detected with different polarization, thus the probability of such an event is $P_{succes} = P_{det}(2,2)$. False events are all the events with excitation number $n \neq 2$ that lead to a detection of two Stokes photons. Figure 3.4.4 shows the probabilities of false and successful events as a function of the Poisson parameter. Here we take a detection efficiency of $P_{detector} = 75\%$ and dark counts rate of 10 Hz [47], thus for a 100 ns pulse $P_{dc} = 10^{-6}$. The fidelity can be taken as the ratio between false and successful probabilities, thus a fidelity of 95% is achievable using a Poisson parameter $\lambda = 0.2$.

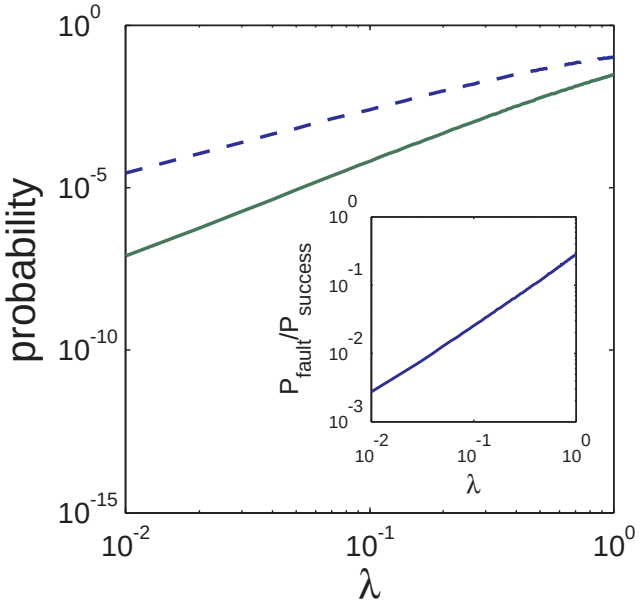

Figure 3.4.4: Probability for a successful and false events as a function of the Poisson parameter (dashed blue - successful event, green - false event). The calculation uses dark counts probability of 10^{-6} and detection efficiency of 75%. Inset shows the ratio between the events probabilities.

Figure 3.4.5 presents the probabilities of the main false events. The predominant false events in low λ are dark counts in the detector while high λ suffers mostly from events related to false detection of higher excitation modes due to the imperfect detection efficiency. It is important to notice that there is a trade off between maximizing the rate of successful events (larger λ) and minimizing the false detection of higher events (smaller λ).

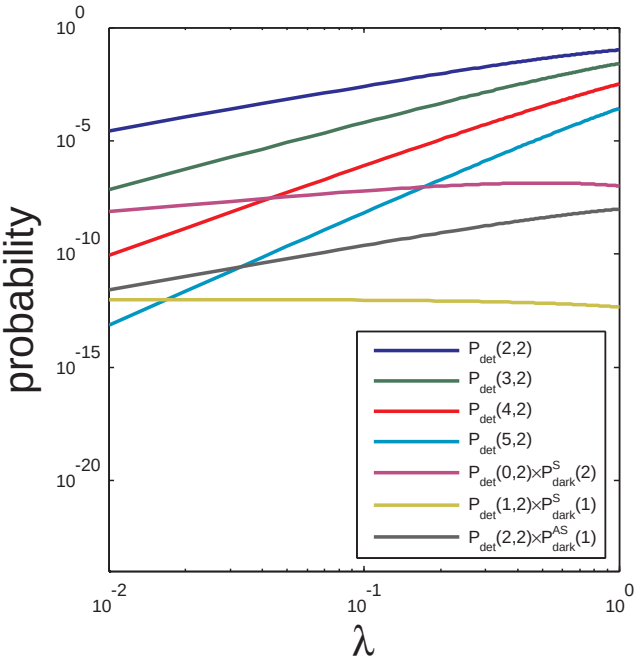

Figure 3.4.5: Probabilities of the main events that can contribute to a post selected experiment when two Stokes photons and two AS photons are detected. $P_{det}(2,2)$ is a successful event, while all others contribute to false events. The sum of all these false events is shown in Fig. 3.4.4. The S or AS superscript in the dark count probability refers to the Stokes or AS detectors respectively.

The rate of such a two photon entanglement source can be estimated by calculating the probability for a successful experiment which is

$$\frac{1}{2} \times P_{det}(2,2,\lambda = 0.2) \times \left(P_B(1) \times P_{detector}\right)^2 \approx 10^{-3}, \tag{3.4.13}$$

where the half is due to detections of $|+_s+_s\rangle$ / $|-_s-_s\rangle$ and $P_B(1) = 0.5$ is the optimal

probability for one AS emission according to the Binomial distribution with a total of two excitations. This ensures a maximal rate for the read process. This probability will create an entangled pair with fidelity of 95%. Assuming a repetition rate of 10 MHz, bounded by the pumping rate due to the natural lifetime of the atoms, the rate of successful entanglement events will be ∼10 kHz. This calculation takes into account the best up to date detectors, with minimal fiber coupling losses. A more conventional setup may have lower detection efficiencies of ∼30%. This will lower the rate substantially to ∼20 Hz for the same fidelity. The tremendous progress in the field of single photon detection [47] implies that even higher rates will be possible in the near future.

3.4.4 Experimental realization

The first step towards realizing the proposed scheme is measuring single photon Stokes-AS correlations in a DLCZ type setup. Figure 3.4.6 shows our experimental setup for measuring single photon correlations, which is similar to the setup reported in refs. [15, 174].

The basic idea is to create a single excitation using a spontaneous Raman process (write process) that is verified by a single Stokes photon measurement. The retrieval is carried out by a detuned EIT process (read process) emitting a single AS photon. The full procedure goes as follows, first a pump beam tuned to F=2→F'=1 transition pumps all the population to level F=1. Practically, we use for this pumping an ECDL laser tuned to the D2 line of ^{87}Rb, meaning the same ground level ($5S_{1/2}$) but a different excited level ($5P_{3/2}$). Since this laser is far detuned from the D1 line (780 nm Vs. 795 nm) it is easier to filter it. We turn off the pump as close as possible to the beginning of the write process (200 ns) in order to decrease the decoherence of the ground state. For the write process we use a DFB laser that is red detuned by ∼1 GHz from the F=1→F'=1 transition. The laser is spectrally filtered twice in order to avoid the broad non coherent background of the laser [46], first with a grating followed by an iris and

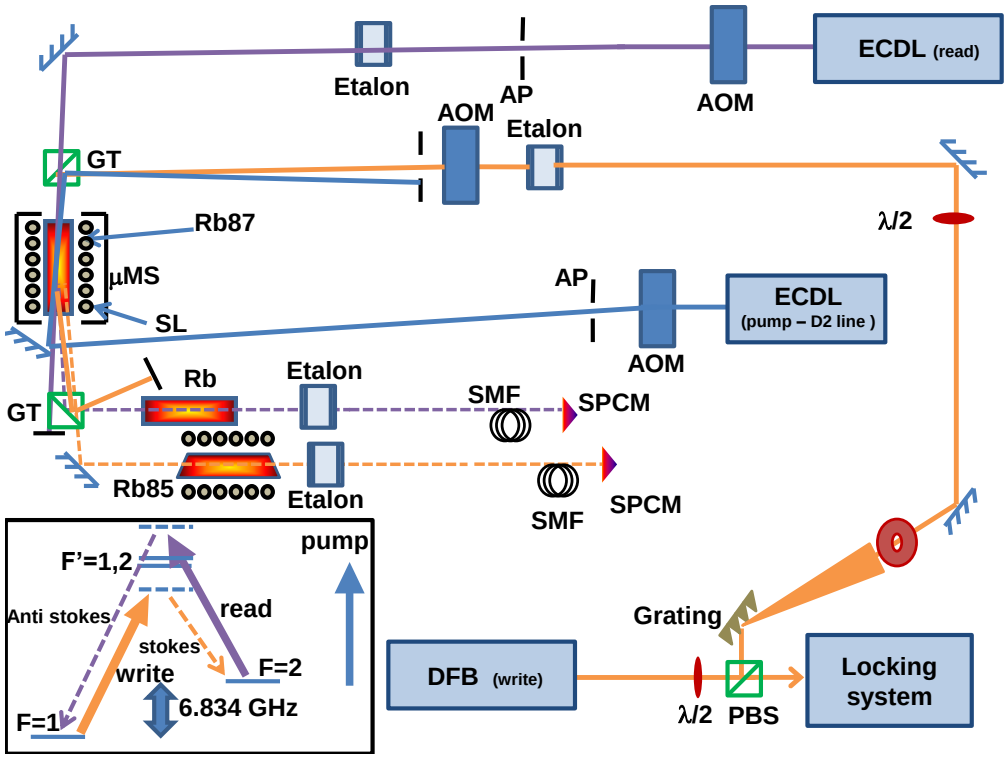

Figure 3.4.6: Single photon storage setup.

afterward with an etalon (finesse is F=30 and FSR=10 GHz). The Stokes photon is measured using a single photon detector (SPCM-AQ4C, Excelitas). In order to filter the classical write beam we use a few filtering mechanisms. a. We make use of the fact that the Stokes photon has an opposite polarization than the write beam and filter the write beam with a Glan-Taylor polarizer to about 10^5. b. A high finesse etalon (F=100) tuned to the Stokes frequency. The etalon is tuned and locked using a temperature PID controller. The filtering of the etalon is approx. 10^4. c. Heated ^{85}Rb cell is used in order to filter the write beam which is detuned to be inside the absorption spectrum. The amount of filtering depends upon the temperature of the cell (Fig. 3.4.7 shows a simulation of the absorption in various temperatures.) and can be extremely high for low enough write power. When the laser power is close to $I_{sat} \sim 2$ mW/cm^2 the transition is saturated and the filter loses its effectiveness, thus it is important that the filter cell is located after the polarization filter. As can be seen in Fig. 3.4.7(d), the high

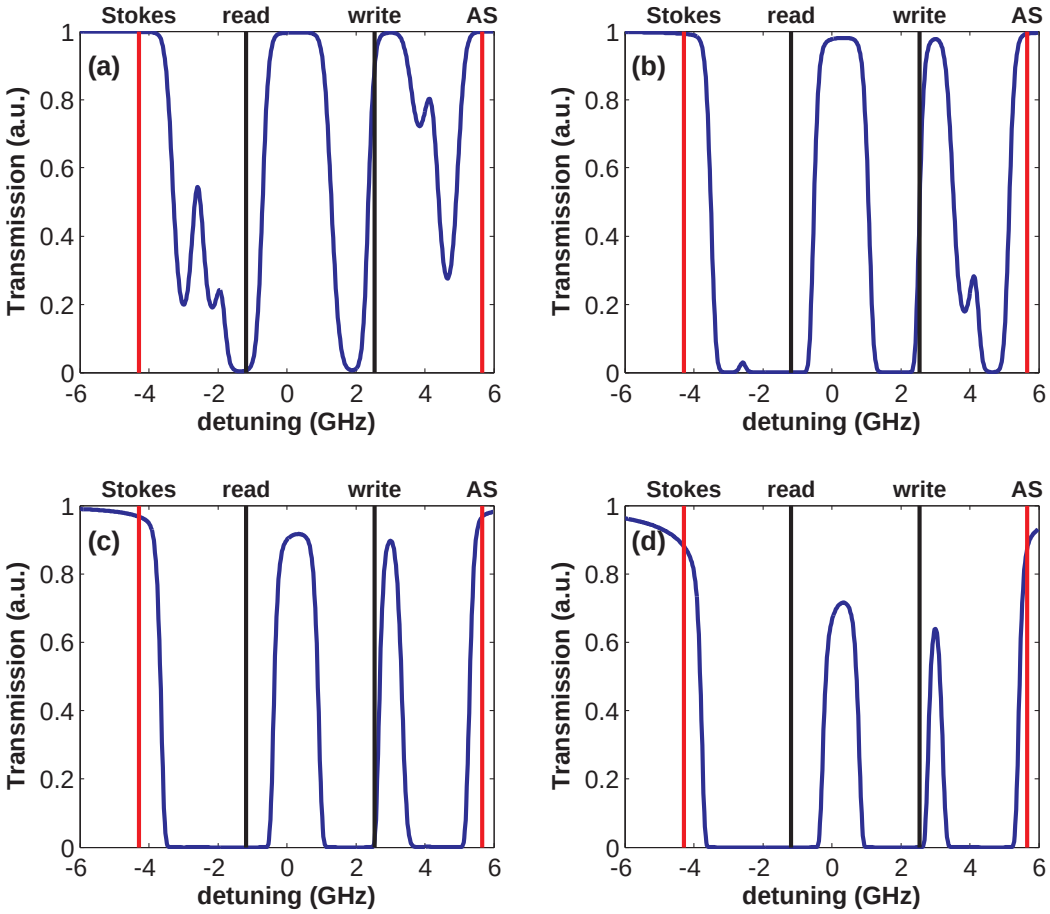

Figure 3.4.7: Transmission spectrum of rubidium for several temperatures. (a) 50°C (b) 70°C (c) 90°C (d) 110°C .Write and read lasers detunings are 1.3 GHz and 1 GHz respectively.

temperature also broadens the other lines that can absorb the Stokes photons. In this case it is possible to work with a lower temperature and shift the atomic line using a magnetic field. After those three filtering stages the beam also goes through two filters for stray light, one is a narrow spectral filter (785-800 nm transmission window) and the second is a single mode fiber. The single mode fiber is also important in order to determine the spatial mode of the Stokes photon.

The Read laser is an ECDL laser that is blue detuned by ∼1 GHz from the F=2→F'=2 transition. The read laser angle is slightly deflected from the write beam. Due to phase matching the AS photons is also deflected from the read beam by the same angle making it easier to filter. Here also we use the same filtering mechanisms that were specified

for the Stokes photons.

Figure 3.4.8(a) shows the Stokes peak by scanning the Fabry-Perot (F-P) etalon filter for different write laser detunings. The movement of the peak center in accordance with the write detuning certifies this peak to be the Stokes. For write detuning of 1.12 GHz the background becomes much higher due to the fact that the write is not sufficiently filtered in the ^{85}Rb cell. In order to store a single excitation thus measuring a single Stokes photon, the write pulse should be weak enough allowing only spontaneous Raman emission to occur. Figure 3.4.8(b-d) shows the transition between spontaneous and stimulated Raman emission for various parameters : pulse length, write laser power and cell temperature. For our entanglement scheme and due to the decoherence time (few μs) we wish to work with short write and read pulses ($\leq$1μs). On the other hand we wish to maximize the retrieval efficiency of the AS photon, thus we use a high temperature of $\sim$70°C. The control over the probability of a single Stokes photon, $P_\lambda(1) \equiv p(s)$, is by modifying the write power.

Next we measure AS photons that are created due to stored excitations. Figure 3.4.9 shows the AS counts measured with and without pumping. After the pumping most of the population is in F=1 level leading to higher spin chain excitation and Stokes emission. The write pulse transfer the population to level F=2 inducing an increase in the AS photon number following the read pulse.

A quantitative measurement of the single photon Stokes/AS correlation can be done using the $g^{(2)}$ correlation function

$$g^{(2)}(S, AS) = \frac{p(AS \mid S)}{p(S)p(AS)} = \frac{\langle n_{AS,S} \rangle N}{\langle n_S \rangle \langle n_{AS} \rangle}, \tag{3.4.14}$$

where N is the total number of iterations, $\langle n_S \rangle$ / $\langle n_{AS} \rangle$ are the number of Stokes and AS photons respectfully and $\langle n_{AS,S} \rangle$ represents how many times AS and Stokes click together. When the Stokes and AS are not correlated $g^{(2)}(S, AS) = 1$, and for correlated beams $g^{(2)}(S, AS) \gg 1$. $g^{(2)}(S, AS) \gg 2$ is almost always an indication for quantum correlations [15, 148]. Figure 3.4.10 shows the $g^{(2)}(S, AS)$ as a function of

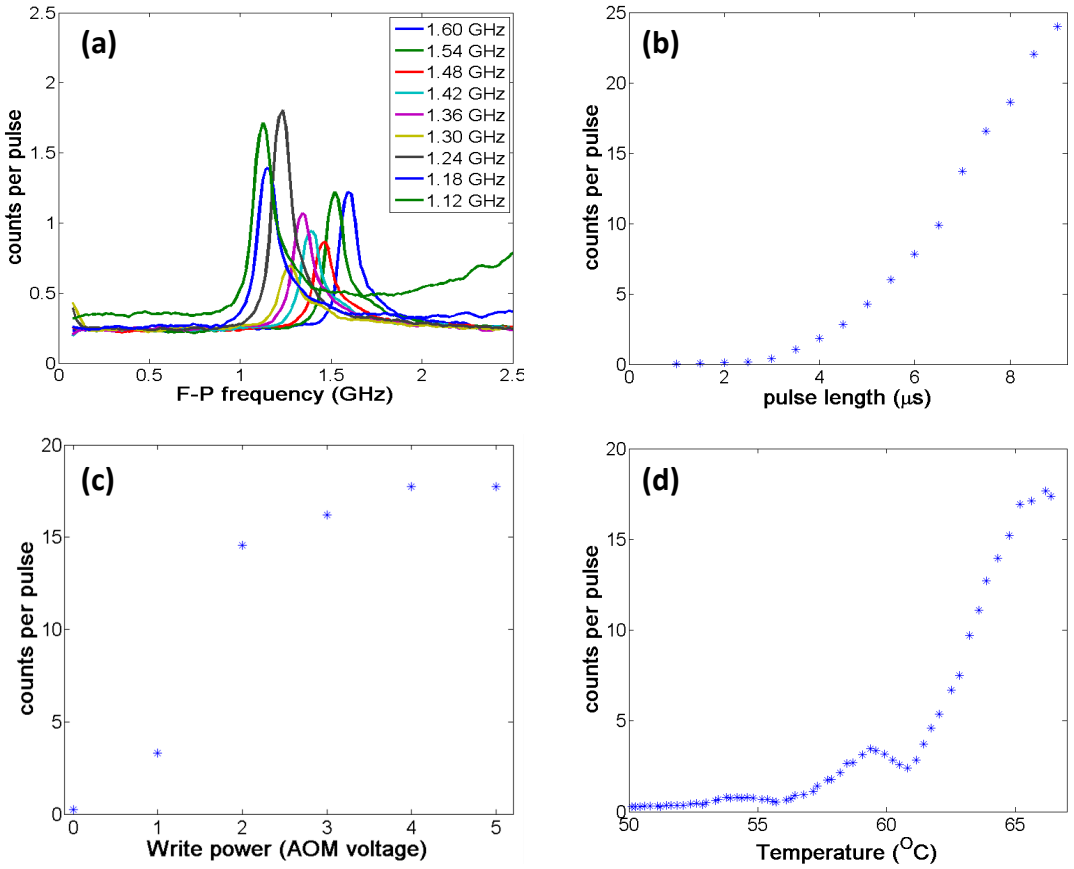

Figure 3.4.8: Stokes measurements. (a) A F-P etalon scan for different write detunings. The Stokes peaks frequency changes according to the write detuning. (b-d) No. of Stokes counts as a function of pulse length, write laser power and cell temperature. All data unless specified else is taken with a pulse length of 7 μs and temperature of 67°C.

frequency for two storage times: 0.5 μs and 3 μs. The results are an average of 6×10^5 iterations with ∼15 % Stokes counts and 0.3 % AS counts. Two observations can be deduced from this result. First it is obvious that there is a peak in the $g^{(2)}$ which is higher than 1 revealing Stokes-AS correlations. These correlations diminish with the storage time, so after 3 μs no apparent correlations is measured. A second observation is the low background having $g^{(2)} \sim 0.85$. This is a result of the high Stokes efficiency allowing for a substantial percentage of two Stokes photons events.

The next step after managing a single photon storage will be applying it twice in order to measure quantum entanglement. The basic setup that is needed for this

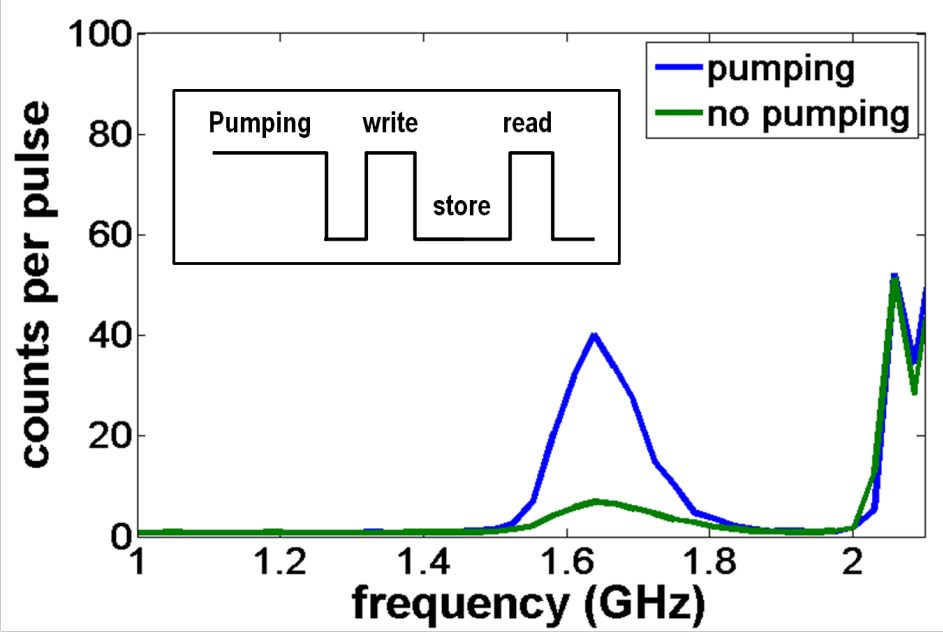

Figure 3.4.9: AS photon detection after storage. The effect of pumping on the peak reveals that the signal is indeed AS photons due to stored excitations.

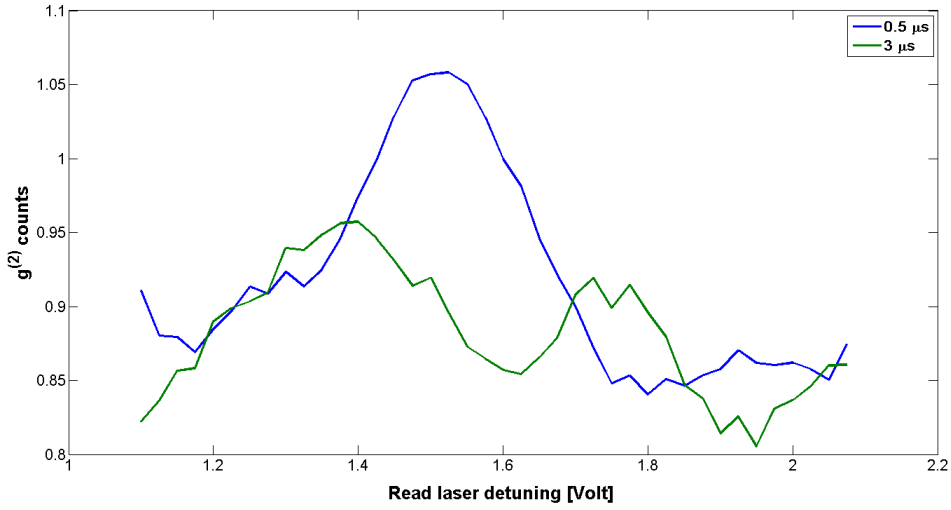

Figure 3.4.10: $g^{(2)}$ measurement.

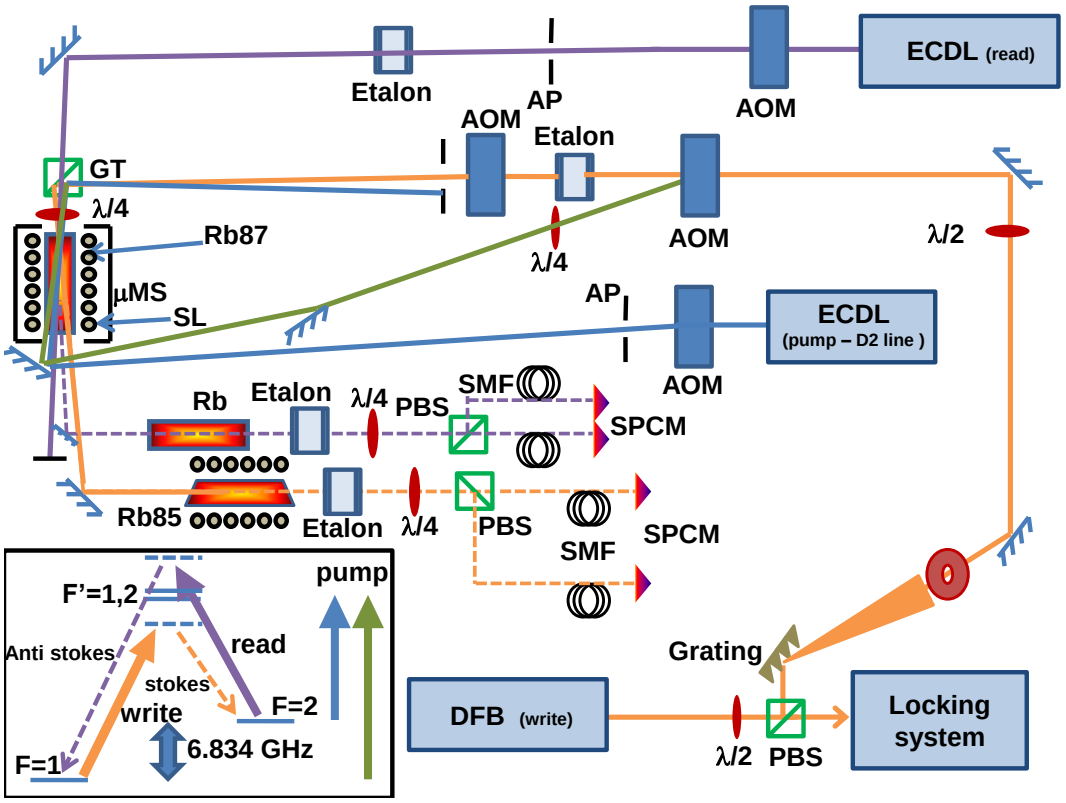

Figure 3.4.11: Two photon entanglement proposed experimental scheme.

measurement is depicted in Fig. 3.4.11. This setup is similar to the single photon storage with a few exceptions. a. Since the polarization of the photon should not be measured the polarization filter (GT polarizer) is removed. As a filtering replacement the rubidium cell filtering should be better now, meaning a higher temperature should be used (on the expense of lower detection efficiency). b. Another pump beam is added. This pumping, on the F=1→F'=1 transition, is done with circular polarization in order to pump the ground state to the $m_F = -1$ state. c. The measurement of the two channels is now done in the polarization Bell basis using polarization beam splitters.

3.4.5 Conclusions

A scheme for the creation of a polarization entanglement between two photons using an atomic ensemble was presented. This scheme relies on the fact that optical transitions between Zeeman sublevels in the single photon regime may act as a polarization beam splitter. Considering realistic experimental restrictions, we estimate a fidelity that can reach up to 95% with entangled pair production rate of 10 kHz. Preliminary measurements of single photon storage were presented and revealed correlations between Stokes and AS photons. The proposed scheme has the potential to become a useful source for quantum communication beyond current available sources.

Chapter 4

Summary and Outlook

Harnessing the light-matter interaction for applicative use is a long term goal of physics research. Although basic research regarding light interacting with atomic media concentrated on simple light structures in steady state conditions, it is obvious that most real applications involve structured light and transients. As part of this ongoing research, the following thesis has provided new insights to the interaction of atomic ensembles with spatially and temporally modulated light both in the classical and in the quantum regimes.

We have shown the ability to use the complex EIT susceptibility in order to spectrally control the motion of vortex array. This motion can be divided into two effects, one is controlled diffraction that causes a nonzero total OAM arrays an extra rotation or counter free space rotation. The second effect is diffusion of the pattern resulting from the actual diffusion of the atomic media. This control of vortices may be useful to applications demanding OAM transfer such as optical wrenches [78]. Another place where vortex beams, or LG beams specifically are being used is quantum entanglement. This vortex array may be used as a basis for hyper-entanglement [188]. In this case a control is needed in order to measure different states.

A different way of modulating light spatially is using a strong laser field that creates an AC Stark shift in the medium. We have demonstrated this effect by creating an optical grating inside the atomic ensemble and measure a probe beam diffracting from it. The efficiency of our setup is only a few percent, but more suitable conditions (high temperature and short cell) may offer much higher efficiencies [109]. Although not measured yet, this method allows, at least theoretically, a very high switching

frequency as the transient response of the atoms should go as $1/\Delta$. Unlike warm vapor EIT where the pump and the probe should be collinear, the incoherent nature of the AC Stark effect allows for a more elaborate 3D pump fields, thus creating light induced photonic crystals.

We have presented a new method for measuring the coherence of EIT media using strong phase modulation of the the pump field. These phase modulations create pulse trains of the probe light that are accompanied by transient oscillations. We have used a time vs. detuning mapping in order to differentiate between adiabatic and non adiabatic regimes where the ratio of EIT linewidth to modulation frequency defines the transition. When a magnetic field is applied the transient oscillations of different Zeeman sublevels interfere. We have shown how to use this interference for high sensitivity broadband magnetic sensing. In our system only three transitions take place, but applying a more general magnetic field can drive up to 7 transitions making this method even more effective. An interesting situation may occur if the phase modulation is combined with some probe spatial modulation such as the vortex array described above. In this case due to the pulsing created in the media, slow moving 3D light structures inside the EIT media can be created.

Finally a theoretical scheme for the creation of heralded two photon entanglement using atomic ensemble was presented. In this scheme the role of atomic media is twofold, first it is used as a quantum storage media for two quantum bits. This is done in the same manner as proposed in the DLCZ protocol [40]. Secondly, using the Zeeman sublevels manifold, a single photon beam splitter is devised. In order to achieve a maximally entangled state a magnetic field is applied. Realistic calculations show 10 kHz entangled pair production taking into account a fidelity of 95%. We have devised an experimental setup to explore this scheme. we have presented early results showing Stokes-AS correlations, But further investigation is needed. In the more general context, our scheme highlights the need to explore not only the storage of single Raman excitations, but also higher order excitations. Together with proper atomic level

schemes it may be possible to create deterministic Fock states or other interesting few photon quantum states.

Chapter 5

Appendix

5.1 Sub-natural linewidth in degenerate two level metastable neon

5.1.1 Introduction

Like most of the research in this thesis, EIT as well as other subnatural linewidth resonances such as EIA and double-dark resonance have been extensively investigated using alkali vapors such as rubidium [104, 124, 132, 192, 197] and sodium [123] using the relevant hyperfine levels. More recently EIT was also demonstrated on the Zeeman levels of metastable helium [66,67,96]. Due to the zero nuclear spin of ^4He, This system is unique for EIT research as it is a Λ system with pure electronic spin, unlike alkali vapors where EIT is realized using hyperfine levels.

In this section sub-natural linewidth resonances in metastable neon are demonstrated for the first time. ^{20}Ne has some special features that separate it from helium or alkali vapors. Similarly to ^4He, and unlike the alkali vapors, metastable neon is a closed two level system that possesses no nuclear spin. The metastability of the system ground state offers some unique advantages. First, it is possible to control the population ratio of the metastable neon via changing the excitation mechanism. Moreover, the stable neon atoms can potentially act as a buffer gas (see sec. 5.1.4 for further discussion). Thus, no additional buffer gas is required.

Although most properties of metastable neon are shared also by helium, there are few distinctions. Neon has approximately five times larger atomic mass [1], thus the

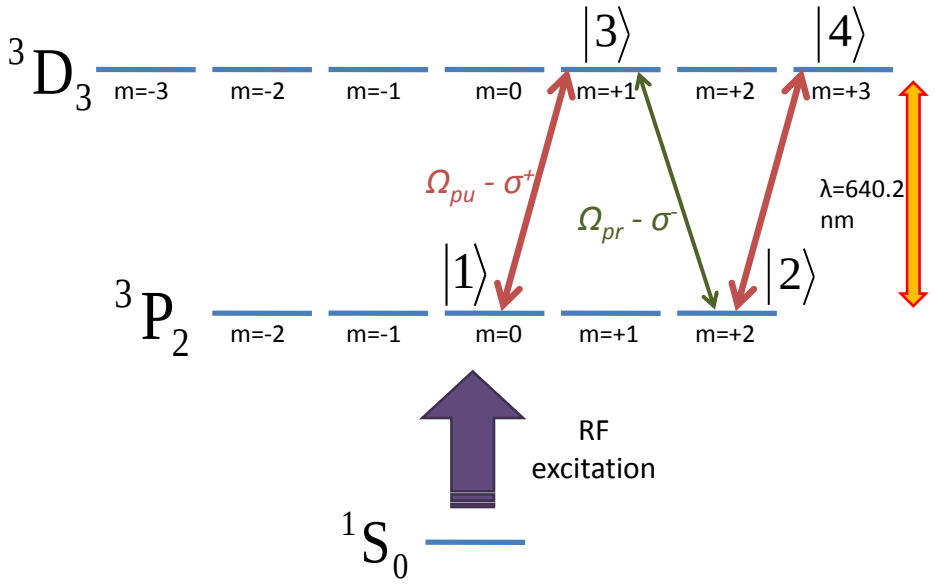

Figure 5.1.1: Schematic energy level diagram for EIA in metastable neon. [11, 147].

EIT resonance width is less limited due to the transit time broadening. However, penning ionization in polarized metastable helium is suppressed by an additional two orders of magnitude relative to neon [176]. Another difference is that the metastable neon system is suitable for Electromagnetically Induced Absorption (EIA) [103], while metastable helium is a true EIT system. The reason for this difference lies in the angular momentum of the two levels. In helium the transition is $J = 1 \rightarrow J' = 0$ [67], thus the excited state has a lower angular momentum than the ground state. The transition in neon, on the other hand, is $J = 2 \rightarrow J' = 3$. Degenerate two level systems exhibit EIA only when $J \rightarrow J' = J + 1$ while EIT is possible using all the configurations [69, 108].

5.1.2 Experimental Setup

We use the neon $^3P_2 \rightarrow ^3D_3$ closed transition. This is a Zeeman degenerate two level system with energy splitting corresponding to a wavelength of 640.2 nm. The ground metastable state $^3P_2$ has a total angular momentum quantum number of $J = 2$ while the

stable ground state $^1S_0$ has an angular momentum quantum number of $J = 0$. Hence, an electric dipole transition is excluded and thus the $^3P_2$ level is a very long metastable state with approximately 15 seconds lifetime [199]. A schematic representation of the relevant neon energy levels is presented in Fig. 5.1.1, where the N system applicable to EIA is marked specifically.

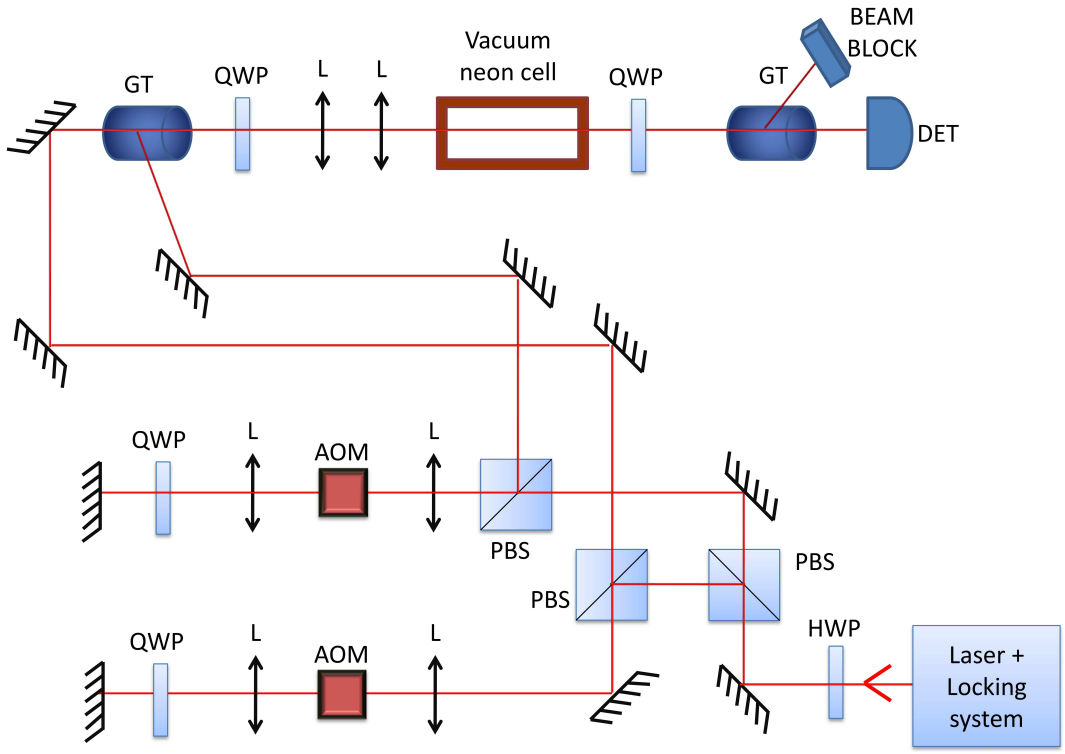

Figure 5.1.2: Experimental optical setup. HWP - half wave plate, QWP - quarter wave plate, L - lens, PBS - polarizing beam splitter, GT - Glan-Taylor polarizer, AOM - acousto optic modulator, DET - photodetector.

Figure 5.1.2 shows our experimental setup for observing EIA in a hot metastable neon vapor. The laser source is an amplified external cavity diode laser at ∼1280 nm which is converted to the transition wavelength by second harmonic generation. The laser is stabilized to the required transition using a standard saturation absorption locking setup [35]. The laser is split into pump and probe beams with different polarizations using a half wave plate. The frequency of each beam is controlled using an acousto-optic

modulator in a double pass configuration to avoid frequency dependent beam deflections. After the frequency modulation the beams are combined using a Glan-Taylor calcite polarizer and pass through the neon cell spatially overlapping. Two quarter wave plates are inserted before and after the cell in order to change the polarization to circular relative to the beams propagation and back to linear polarization. After the neon cell the probe is separated from the pump using another Glan-Taylor polarizer and measured using a photodetector. The metastable neon excitation is achieved by a coaxial resonator with helical inner conductor [113] that surrounds the cell and resonates at 61 MHz with an unloaded Q factor of $\sim$ 200. We use a pair of Helmholtz coils for axial magnetic field measurements. The vapor cell is shielded by a mu-metal housing reducing stray magnetic field by a factor of $\sim$100.

5.1.3 Results

Figure 5.1.3(a) shows the probe transmission spectra for different pump intensities. The 8 MHz shown is the limit of our scan before a sharp decrease in transmission due to the AOM's efficiencies masks the data. Both pump and probe beams are approximately Gaussian with a waist of 1 mm. The optical power of the probe is 0.3 mW. Three major observations can be inferred from Fig. 5.1.3(a). First, higher pump intensities result in an increase of the overall transmission due to hole burning. For the used pump intensities, this feature is much broader than the natural linewidth due to power broadening. Near the two photon resonance we observe two opposite features. The first one is a broad (few MHz), but sub-natural linewidth absorption line. This line is observed best for low powers as it is power broadened. The second feature is a narrow peak of enhanced transmission around the two photon resonance. These two effects are a manifestation of EIA at high pump powers [69]. It is important to notice that in standard EIA, when the pump power is lowered substantially bellow the natural linewidth, the transmission peak at the center should vanish and narrow absorption peak should take its place [69, 90]. We were unable to see this effect in our system.

Possible reasons for that are given in 5.1.4.

Using a Lorenzian fit to the central transmission peak, shown as dashed red lines in Fig. 5.1.3(a), the widths for the various intensities was extracted and plotted in Fig. 5.1.3(b) to show the power broadening of the central peak. In order to understand this power broadening quantitatively we compare it to the theory of Doppler broadened EIT. The broadening of EIT with no collisions predicts a quadratic function of the pump Rabi frequency Ω [66]:

$$\Gamma_{EIT} = 2\gamma_g + \frac{\Omega^2}{\delta} \tag{5.1.1}$$

where γ_g is the ground state decoherence and δ is an effective pumping rate that depends on the power of the pump. For low intensities such that $(\frac{\Omega}{W_D})^2 \ll \frac{2\gamma_g}{\Gamma}$, where W_D is the doppler width and Γ is the natural decay rate, only a small resonant fraction of the atoms participate in the EIT. The effective rate in this case is $\delta_{low} = \Omega\sqrt{\Gamma/\gamma_g}$. In the opposite regime, $(\frac{\Omega}{W_D})^2 \gg \frac{2\gamma_g}{\Gamma}$, the intensity is strong enough to pump all the Doppler broadened population and the effective rate is $\delta_{high} = W_D$. In our experiment 10 MHz$< \Omega <$40 MHz, Γ=8 MHz and $W_D \simeq$1.3 GHz. The ground state decoherence is governed mostly by the transit-time broadening [169]. Our beam has a width of $\sim$2 mm and the atomic ballistic velocity at room temperature is $\sim$500 m/s, thus the decoherence due to the transit-time can be estimated to be 250 kHz. Taking into account velocity changing collisions (VCC) with the stable neon atoms the atomic motion becomes diffusive, increasing the transit-time. For the pressure we use (200 mtorr) the diffusive transit-time is $\sim$ 2.5 longer than the ballistic one, making the decoherence $\sim$100 kHz. Using these values reveals that our system should be in the low intensity limit, hence the power broadening should be $\propto \sqrt{I}$. Strikingly, Fig. 5.1.3(b) depicts a linear trend with the intensity. We fit the data to a linear function obtaining δ =0.9 GHz which is very similar to W_D. It is important to note that Goldfarb et al. showed a similar effect in metastable helium that was attributed to many VCC that effectively explored all the Doppler velocity range [67]. In their experiment they estimated 10^4 collisions during the diffusion, but in our case due to smaller beam diameter and lower pressure the

number of collisions is estimated to be ~ 5. Figure 5.1.4 shows the central peak power broadening for several low pressure neon cells. It is apparent that even at very low pressures, where the number of collisions is $\ll 1$ and the dynamics should be ballistic, the broadening is approximately linear, with $\delta \sim W_D$.

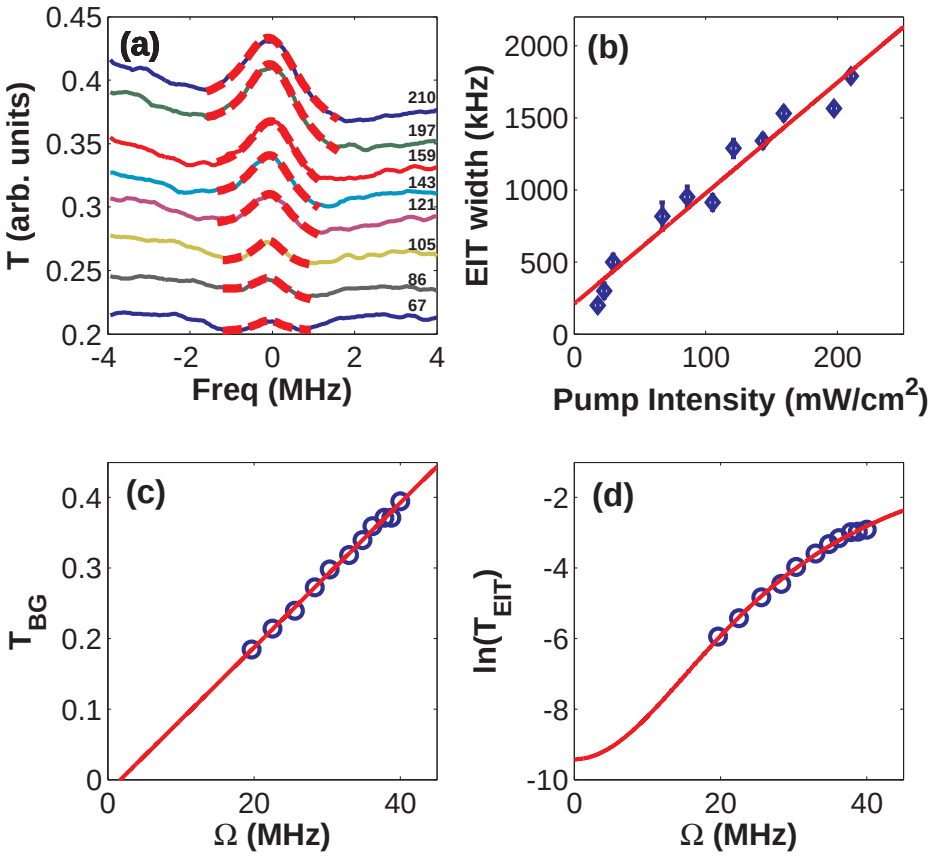

Figure 5.1.3: (a) Probe transmission as a function of the two photon detuning for several pump intensities. Dashed red lines are Lorentzian fit to the central peak. The intensity on the right hand side is in mW/cm^2. (b) FWHM width of the central peak as a function of the pump intensity. The solid line is a linear fit to the data. (c) Background transmission $(-\ln OD))$ as a function of the Rabi frequency. Solid line is a linear fit to the data. (d) Central peak height as a function of the Rabi frequency. Solid line is a fit according to Eq. 5.1.2.

Another interesting aspect of central peak is its height. Figure 5.1.3(d) shows the natural logarithm of the peak heights as a function of the Rabi frequency. The peak transmission can be estimated to be

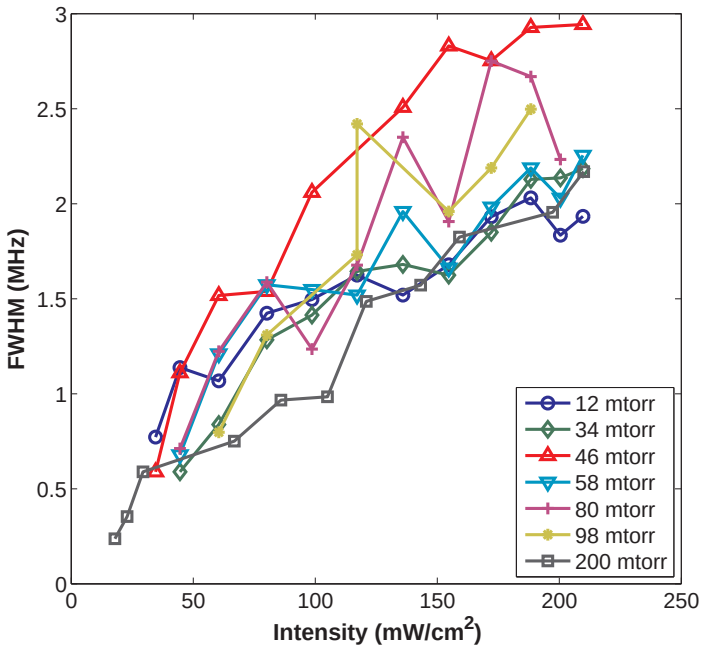

Figure 5.1.4: Power broadening of the central peak for different neon pressures. The lines connecting the experimental data are guidance for the eye. The data for 200 mtorr is taken from Fig. 5.1.3(b).

$$\ln\left({}^{T}/_{OD}\right) = \frac{\ln T_0}{1 + \frac{\Omega^2}{4W_D\gamma_g}}, \tag{5.1.2}$$

where $OD = -\ln T_{BG}$ is the optical density of the medium with T_{BG} taken from Fig. 5.1.3(c) and T_0 is the transmission with no pump field. This expression is similar to the one used in [67] for EIT, but with the exception of normalizing the transmission with the OD due to the hole burning effect. The data was fitted to Eq. 5.1.2 with the best fit presented as the solid line in Fig. 5.1.3(d). The fit yields $4W_D\gamma_g = 7 \times 10^{14}\,\mathrm{Hz}^2$ which is in good agreement with our estimation of the ground state decoherence.

In our setup we can also control the RF power of the excitation, thus controlling the percentage of metastable neon. Figure 5.1.5 shows a comparison of the power broadening slope for different RF powers (blue circles). This slope was calculated in the same way as in Fig. 5.1.3(b). Higher RF powers have smaller slopes suggesting a narrowing. This narrowing can be explained when taking into consideration the effect

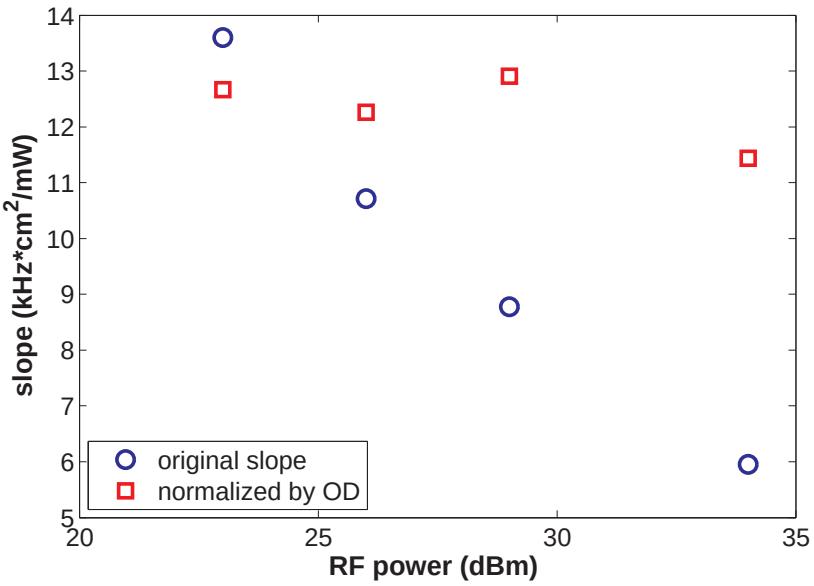

Figure 5.1.5: Power broadening slope as a function of the RF power. blue circles - original slope. red squares - normalized slope by the optical density.

of optical density such that [57] :

$$\Gamma_{EIT} = 2\gamma_g + \frac{\Omega^2}{\delta}\frac{1}{\sqrt{OD}}. \tag{5.1.3}$$

We use Eq. 5.1.3 for normalizing the slope by multiplying with $\sqrt{OD}$ (red squares). The results clearly show that the narrowing effect is due to the more effective population transfer to the metastable state at high RF powers.

5.1.4 Discussion and conclusions

It is well known theoretically and experimentally that transmission peak appears in EIA systems under two conditions, a. when the degeneracy of the Zeeman sublevels is lifted. b. If the intensity of the pump is high enough such that $\Omega \gg \Gamma$ [69, 90, 108]. All the results presented above were taken for high enough pump intensity such that the EIA should have a transmission peak. On the other hand, when we lowered the intensity no narrow EIA was discovered. Regarding the degeneracy, the main process that can lift it is the magnetic field due to the RF excitation. For the highest RF power we use, the

magnetic field is estimated to be ∼1 G which is equivalent to $\sim 1.5\,\mathrm{MHz} < \Gamma$. Hence the magnetic field is not enough to lift the degeneracy. Moreover, we also applied a constant axial magnetic field of up to $2\,G$ using a Helmholz configuration. This field shifted the resonance linearly with the applied magnetic field as expected by the Zeeman splitting theory, but otherwise did not change any other transmission attributes. A different mechanism by which EIA can become EIT is due to high buffer gas pressure [49]. This happens because frequent spin-exchange collisions prevent substantial coherence buildup in the excited state that is essential to EIA. This is an unlikely explanation in our case due to the fact that we did not discover any EIA trace even for very low pressures where the atomic dynamics is ballistic. A possible resolution of this quandary (why EIA was not observed) may lie in the RF field. This field has a frequency which is much higher than Γ, thus the pump beam actually changes its magnetic axis causing a reduction in the effective coherence buildup between the EIA excited levels. This may cause a destruction of narrow EIA but not EIT, where only ground state coherence is needed. In any case, this should be part of further research.

We fitted our central transmission peak power broadening results using 5.1.1 under the assumption of VCC. This is not necessarily true in the metastable neon case where the ground state has a non zero orbital angular momentum. In this case spin exchange collisions may have a much higher cross section. Supporting evidence for this claim is that in our experiment we did not detect transmission peak at high pressures (>0.5 torr). This effect is very interesting as metastable neon is extensively being used in atomic traps where collisions are frequent [11]. Our system is well suited to explore the cross section of these collisions.

Another unique result is the linear broadening with $\delta = W_D$ even at the low power limit and with low pressure such that VCC does not affect the dynamics. We did not find any simple explanation for this effect and it should be a part of further research.

To conclude, we present here the first observation of sub-natural linewidth resonance in metastable neon. We measure linewidths as narrow as 200 kHz. We measure the

power broadening of the central transmission peak linewidth for different pressures and RF excitation powers and compare it to EIT. The peak width is inversely proportional to the Doppler width even for low pressures and intensities. By extrapolating the power broadening results we estimate the ground decoherence in our system to be 100 kHz. The dominant mechanism for this decoherence is the transit time, which was also verified by the hard sphere model.

Bibliography

[1] 'NIST Handbook of Basic Atomic Spectroscopic Data, http://physics.nist.gov/PhysRefData/Handbook/index.html'. Cited on page 133.

[2] Acosta, V., M. Ledbetter, S. Rochester, D. Budker, D. Jackson Kimball, D. Hovde, W. Gawlik, S. Pustelny, J. Zachorowski, and V. Yashchuk: 2006, 'Nonlinear magneto-optical rotation with frequency-modulated light in the geophysical field range'. *Phys. Rev. A* **73**(5), 053404. Cited on page 2.

[3] Afzelius, M., I. Usmani, A. Amari, B. Lauritzen, A. Walther, C. Simon, N. Sangouard, J. Minár, H. de Riedmatten, N. Gisin, and S. Kröll: 2010, 'Demonstration of Atomic Frequency Comb Memory for Light with Spin-Wave Storage'. *Phys. Rev. Lett.* **104**, 040503. Cited on page 21.

[4] Akopian, N., N. Lindner, E. Poem, Y. Berlatzky, J. Avron, D. Gershoni, B. Gerardot, and P. Petroff: 2006, 'Entangled Photon Pairs from Semiconductor Quantum Dots'. *Phys. Rev. Lett.* **96**(13), 130501. Cited on page 109.

[5] Akulshin, A. M., A. Lezama, a. I. Sidorov, R. J. McLean, and P. Hannaford: 2005, ''Storage of light' in an atomic medium using electromagnetically induced absorption'. *J. Phys. B At. Mol. Opt. Phys.* **38**(23), 365–374. Cited on page 21.

[6] Allen, L., M. Beijersbergen, R. Spreeuw, and J. Woerdman: 1992, 'Orbital angular momentum of light and the transformation of Laguerre-Gaussian laser modes'. *Phys. Rev. A* **45**(11), 8185–8189. Cited on page 36.

[7] Allred, J. C., R. N. Lyman, T. W. Kornack, and M. V. Romalis: 2002, 'High-Sensitivity Atomic Magnetometer Unaffected by Spin-Exchange Relaxation'. *Phys. Rev. Lett.* **89**, 130801. Cited on page 3.

[8] Arimondo, E.: 1996, 'Coherent Population Trapping in Laser Spectroscopy'. In: E. Wolf (ed.): *Progress in Optics*, Vol. 35. Elsevier, pp. 257 – 354. Cited on page 14.

[9] Arlt, J., K. Dholakia, L. Allen, and M. J. Padgett: 1998, 'The production of multiringed Laguerre-Gaussian modes by computer-generated holograms'. *J. Mod. Opt.* **45**(6), 1231–1237. Cited on pages 40 and 42.

[10] Artoni, M. and G. C. La Rocca: 2006, 'Optically Tunable Photonic Stop Bands in Homogeneous Absorbing Media'. *Phys. Rev. Lett.* **96**, 073905. Cited on pages 2 and 76.

[11] Ashmore, J. P.: 2005, 'Laser Cooling And Trapping Of Metastable Neon And Applications To Photoionziation'. Ph.D. thesis, Griffith University. Cited on pages 134 and 141.

[12] Aspect, A., P. Grangier, and G. Roger: 1981, 'Experimental Tests of Realistic Local Theories via Bell's Theorem'. *Phys. Rev. Lett.* **47**(7), 460–463. Cited on pages 26 and 108.

[13] Aspect, A., P. Grangier, and G. Roger: 1982, 'Experimental Realization of Einstein-Podolsky-Rosen-Bohm Gedankenexperiment: A New Violation of Bell's Inequalities'. *Phys. Rev. Lett.* **49**(2), 91–94. Cited on page 26.

[14] Autler, S. H. and C. H. Townes: 1955, 'Stark Effect in Rapidly Varying Fields'. *Phys. Rev.* **100**, 703–722. Cited on page 15.

[15] Bashkansky, M., F. K. Fatemi, and I. Vurgaftman: 2012, 'Quantum memory in warm rubidium vapor with buffer gas'. *Opt. Lett.* **37**(2), 142. Cited on pages 4, 31, 108, 116, 120, and 123.

[16] Bekshaev, A. Y., M. S. Soskin, and M. V. Vasnetsov: 2003, 'Optical vortex symmetry breakdown and decomposition of the orbital angular momentum of light beams'. *J. Opt. Soc. Am. A* **20**(8), 1635. Cited on page 74.

[17] Belfi, J., G. Bevilacqua, V. Biancalana, Y. Dancheva, and L. Moi: 2007, 'All optical sensor for automated magnetometry based on coherent population trapping'. *J. Opt. Soc. Am. B* **24**(7), 1482. Cited on pages 3, 94, 102, and 103.

[18] Bell, J. S.: 1964, 'On the Einstein-Podolsky-Rosen paradox'. *Physics* **1**, 195. Cited on page 26.

[19] Bennett, C. H., G. Brassard, C. Crépeau, R. Jozsa, A. Peres, and W. K. Wootters: 1993, 'Teleporting an unknown quantum state via dual classical and Einstein-Podolsky-Rosen channels'. *Phys. Rev. Lett.* **70**, 1895–1899. Cited on page 26.

[20] Bennett, C. H., G. Brassard, et al.: 1984, 'Quantum cryptography: Public key distribution and coin tossing'. In: *Proceedings of IEEE International Conference on Computers, Systems and Signal Processing*, Vol. 175. p. 8. Cited on page 28.

[21] Born, M., E. Wolf, and A. Bhatia: 1999, *Principles of Optics: Electromagnetic Theory of Propagation, Interference and Diffraction of Light*. Cambridge University Press. Cited on pages 1 and 76.

[22] Briegel, H.-J., W. Dür, J. I. Cirac, and P. Zoller: 1998, 'Quantum repeaters: The role of imperfect local operations in quantum communication'. *Phys. Rev. Lett.* **81**(26), 5932. Cited on pages 4 and 28.

[23] Brown, A. W. and M. Xiao: 2005, 'All-optical switching and routing based on an electromagnetically induced absorption grating'. *Opt. Lett.* **30**(7), 699–701. Cited on pages 2, 76, and 77.

[24] Budker, D., D. J. Orlando, and V. Yashchuk: 1999, 'Nonlinear laser spectroscopy and magneto-optics'. *Am. J. Phys.* **67**, 584. Cited on pages 2 and 77.

[25] Budker, D. and M. Romalis: 2007, 'Optical magnetometry'. *Nat. Phys.* **3**(4), 227–234. Cited on pages 3 and 103.

[26] Campbell, G., A. Ordog, and A. I. Lvovsky: 2009, 'Multimode electromagnetically induced transparency on a single atomic line'. *New J. Phys.* **11**(10), 103021. Cited on pages 3, 94, and 107.

[27] Carroll, C. E. and F. T. Hioe: 1986, 'Generalisation of the Landau-Zener calculation to three levels'. *J. Phys. A. Math. Gen.* **19**(7), 1151–1161. Cited on page 95.

[28] Carvalho, P., L. de Araujo, and J. Tabosa: 2004, 'Angular dependence of an electromagnetically induced transparency resonance in a Doppler-broadened atomic vapor'. *Phys. Rev. A* **70**(6), 1–5. Cited on page 23.

[29] Chen, M. and F. S. Roux: 2008, 'Accelerating the annihilation of an optical vortex dipole in a Gaussian beam.'. *J. Opt. Soc. Am. A. Opt. Image Sci. Vis.* **25**(6), 1279–86. Cited on page 70.

[30] Chen, Z., J. Pu, and D. Zhao: 2011, 'Tight focusing properties of linearly polarized Gaussian beam with a pair of vortices'. *Phys. Lett. A* **375**(32), 2958–2963. Cited on pages 63 and 71.

[31] Choi, K. S., H. Deng, J. Laurat, and H. J. Kimble: 2008, 'Mapping photonic entanglement into and out of a quantum memory.'. *Nature* **452**(7183), 67–71. Cited on pages 4, 31, and 108.

[32] Choi, K. S., a. Goban, S. B. Papp, S. J. van Enk, and H. J. Kimble: 2010, 'Entanglement of spin waves among four quantum memories'. *Nature* **468**(7322), 412–416. Cited on pages 4 and 31.

[33] Cox, K., V. I. Yudin, A. V. Taichenachev, I. Novikova, and E. E. Mikhailov: 2011, 'Measurements of the magnetic field vector using multiple electromagnetically induced transparency resonances in Rb vapor'. *Phys. Rev. A* **83**, 015801. Cited on pages 60 and 101.

[34] Dai, H.-N., H. Zhang, S.-J. Yang, T.-M. Zhao, J. Rui, Y.-J. Deng, L. Li, N.-L. Liu, S. Chen, X.-H. Bao, X.-M. Jin, B. Zhao, and J.-W. Pan: 2012, 'Holographic Storage of Biphoton Entanglement'. *Phys. Rev. Lett.* **108**(21), 210501. Cited on page 108.

[35] Demtröder, W.: 2008, *Laser Spectroscopy: Experimental Techniques*. Springer, Berlin, 4th ed. edition. Cited on pages 2, 52, 53, 54, and 135.

[36] Dicke, R. H.: 1954, 'Coherence in Spontaneous Radiation Processes'. *Phys. Rev.* **93**, 99–110. Cited on pages 24 and 111.

[37] Donley, E. a., T. P. Heavner, F. Levi, M. O. Tataw, and S. R. Jefferts: 2005, 'Double-pass acousto-optic modulator system'. *Rev. Sci. Instrum.* **76**(6), 063112. Cited on page 49.

[38] Dreischuh, A., S. Chervenkov, D. Neshev, G. G. Paulus, and H. Walther: 2002, 'Generation of lattice structures of optical vortices'. *J. Opt. Soc. Am. B* **19**(3), 550. Cited on page 66.

[39] Duan, L.-M., J. Cirac, and P. Zoller: 2002, 'Three-dimensional theory for interaction between atomic ensembles and free-space light'. *Phys. Rev. A* **66**(2), 023818. Cited on pages 30 and 111.

[40] Duan, L.-M., M. D. Lukin, J. Cirac, and P. Zoller: 2001, 'Long-distance quantum communication with atomic ensembles and linear optics.'. *Nature* **414**(6862), 413–8. Cited on pages 4, 28, 108, and 130.

[41] Dudin, Y. O., L. Li, and A. Kuzmich: 2013, 'Light storage on the time scale of a minute'. *Phys. Rev. A* **87**, 031801. Cited on pages 3 and 21.

[42] Dudley, D., W. M. Duncan, and J. Slaughter: 2003, 'Emerging digital micromirror device (DMD) applications'. *Proc. SPIE* **4985**, 14–25. Cited on page 40.

[43] Dutton, Z., M. Bashkansky, M. Steiner, and J. Reintjes: 2006, 'Analysis and optimization of channelization architecture for wideband slow light in atomic vapors.'. *Opt. Express* **14**(12), 4978–91. Cited on pages 3 and 94.

[44] Einstein, A., B. Podolsky, and N. Rosen: 1935, 'Can Quantum-Mechanical Description of Physical Reality Be Considered Complete?'. *Phys. Rev.* **47**, 777–780. Cited on page 26.

[45] Eisaman, M. D.: 2006, 'Generation , Storage , and Retrieval of Nonclassical States of Light using Atomic Ensembles'. Ph.D. thesis, Harvard. Cited on page 31.

[46] Eisaman, M. D., L. Childress, A. André, F. Massou, A. S. Zibrov, and M. D. Lukin: 2004, 'Shaping Quantum Pulses of Light Via Coherent Atomic Memory'. *Phys. Rev. Lett.* **93**, 233602. Cited on page 120.

[47] Eisaman, M. D., J. Fan, a. Migdall, and S. V. Polyakov: 2011, 'Invited Review Article: Single-photon sources and detectors'. *Rev. Sci. Instrum.* **82**(7), 071101. Cited on pages 108, 118, and 120.

[48] Erhard, M. and H. Helm: 2001, 'Buffer-gas effects on dark resonances: Theory and experiment'. *Phys. Rev. A* **63**, 043813. Cited on pages 24 and 52.

[49] Failache, H., P. Valente, G. Ban, V. Lorent, and A. Lezama: 2003, 'Inhibition of electromagnetically induced absorption due to excited-state decoherence in Rb vapor'. *Phys. Rev. A* **67**, 043810. Cited on page 141.

[50] Figueroa, E., F. Vewinger, J. Appel, and A. I. Lvovsky: 2006, 'Decoherence of electromagnetically induced transparency in atomic vapor'. *Opt. Lett.* **31**(17), 2625. Cited on pages 58 and 96.

[51] Firstenberg, O., P. London, M. Shuker, A. Ron, and N. Davidson: 2009a, 'Elimination, reversal and directional bias of optical diffraction'. *Nat. Phys.* **5**(9), 665–668. Cited on pages 2, 63, and 68.

[52] Firstenberg, O., P. London, D. Yankelev, R. Pugatch, M. Shuker, and N. Davidson: 2010, 'Self-Similar Modes of Coherent Diffusion'. *Phys. Rev. Lett.* **105**, 183602. Cited on page 73.

[53] Firstenberg, O., M. Shuker, A. Ben-Kish, D. R. Fredkin, N. Davidson, and A. Ron: 2007, 'Theory of Dicke narrowing in coherent population trapping'. *Phys. Rev. A* **76**, 013818. Cited on page 17.

[54] Firstenberg, O., M. Shuker, N. Davidson, and A. Ron: 2009b, 'Elimination of the Diffraction of Arbitrary Images Imprinted on Slow Light'. *Phys. Rev. Lett.* **102**, 043601. Cited on pages 2, 63, and 68.

[55] Firstenberg, O., M. Shuker, R. Pugatch, D. R. Fredkin, N. Davidson, and A. Ron: 2008, 'Theory of thermal motion in electromagnetically induced transparency: Effects of diffusion, Doppler broadening, and Dicke and Ramsey narrowing'. *Phys. Rev. A* **77**, 043830. Cited on page 67.

[56] Firstenberg, O., M. Shuker, A. Ron, and N. Davidson: 2013, 'Colloquium: Coherent diffusion of polaritons in atomic media'. *Rev. Mod. Phys.* **85**(3), 941–960. Cited on pages 22, 24, 67, and 68.

[57] Fleischhauer, M., A. Imamoglu, and J. Marangos: 2005, 'Electromagnetically induced transparency: Optics in coherent media'. *Rev. Mod. Phys.* **77**(2), 633–673. Cited on pages 2, 13, 17, 66, 96, and 140.

[58] Fleischhauer, M. and M. Lukin: 2002, 'Quantum memory for photons: Dark-state polaritons'. *Phys. Rev. A* **65**(2), 022314. Cited on pages 3 and 19.

[59] Fleischhauer, M. and M. D. Lukin: 2000, 'Dark-State Polaritons in Electromagnetically Induced Transparency'. *Phys. Rev. Lett.* **84**, 5094–5097. Cited on page 20.

[60] Franke-Arnold, S., L. Allen, and M. J. Padgett: 2008, 'Advances in optical angular momentum'. *Laser Photonics Rev.* **2**(4), 299–313. Cited on page 63.

[61] Frejlich, J.: 2007, *Photorefractive Materials: Fundamental Concepts, Holographic Recording and Materials Characterization*. Wiley. Cited on page 76.

[62] Gan, X., J. Zhao, S. Liu, and L. Fang: 2009, 'Generation and motion control of optical multi-vortex'. *Chinese Opt. Lett.* **7**(12), 1142–1145. Cited on page 64.

[63] Garraway, B. M. and N. V. Vitanov: 1997, 'Population dynamics and phase effects in periodic level crossings'. *Phys. Rev. A* **55**(6), 4418–4432. Cited on page 95.

[64] Gaudreau, L., G. Granger, A. Kam, G. C. Aers, S. A. Studenikin, P. Zawadzki, M. Pioro-Ladrière, Z. R. Wasilewski, and A. S. Sachrajda: 2011, 'Coherent control of three-spin states in a triple quantum dot'. *Nat. Phys.* **8**(1), 54–58. Cited on page 95.

[65] Gheri, K., C. Saavedra, P. Törmä, J. Cirac, and P. Zoller: 1998, 'Entanglement engineering of one-photon wave packets using a single-atom source'. *Phys. Rev. A* **58**(4), R2627–R2630. Cited on page 109.

[66] Ghosh, J., R. Ghosh, F. Goldfarb, J.-L. Le Gouët, and F. Bretenaker: 2009, 'Analysis of electromagnetically induced transparency and slow light in a hot vapor of atoms undergoing collisions'. *Phys. Rev. A* **80**, 023817. Cited on pages 23, 133, and 137.

[67] Goldfarb, F., J. Ghosh, M. David, J. Ruggiero, T. Chaneliere, J. L. Gouet, H. Gilles, R. Ghosh, and F. Bretenaker: 2008, 'Observation of ultra-narrow electromagnetically induced transparency and slow light using purely electronic spins in a hot atomic vapor'. *EPL- Europhys. Lett.* **82**(5), 54002. Cited on pages 133, 134, 137, and 139.

[68] Goodman, J.: 2005, *Introduction To Fourier Optics*, McGraw-Hill physical and quantum electronics series. Roberts & Co. Cited on page 86.

[69] Goren, C., A. D. Wilson-Gordon, M. Rosenbluh, and H. Friedmann: 2004, 'Atomic four-level N systems'. *Phys. Rev. A* **69**, 053818. Cited on pages 134, 136, and 140.

[70] Gray, H. R., R. M. Whitley, and C. R. Stroud: 1978, 'Coherent trapping of atomic populations'. *Opt. Lett.* **3**(6), 218–220. Cited on page 12.

[71] Greentree, A. D., T. Smith, S. de Echaniz, A. Durrant, J. Marangos, D. Segal, and J. Vaccaro: 2002, 'Resonant and off-resonant transients in electromagnetically induced transparency: Turn-on and turn-off dynamics'. *Phys. Rev. A* **65**(5), 053802. Cited on page 94.

[72] Hammerer, K.: 2010, 'Quantum interface between light and atomic ensembles'. *Rev. Mod. Phys.* **82**(2), 1041–1093. Cited on page 25.

[73] Harris, S.: 1993, 'Electromagnetically induced transparency with matched pulses'. *Phys. Rev. Lett.* **70**(5), 552–555. Cited on page 107.

[74] Harris, S. E., J. E. Field, and A. Imamoglu: 1990, 'Nonlinear optical processes using electromagnetically induced transparency'. *Phys. Rev. Lett.* **64**(10), 1107–1110. Cited on page 12.

[75] Harshawardhan, W. and G. S. Agarwal: 1997, 'Multiple Landau-Zener crossings and quantum interference in atoms driven by phase modulated fields'. *Phys. Rev. A* **55**(3), 2165–2171. Cited on page 95.

[76] Hau, L. V., S. E. Harris, Z. Dutton, and C. H. Behroozi: 1999, 'Light speed reduction to 17 metres per second in an ultracold atomic gas'. *Nature* **397**(February), 594–598. Cited on pages 3 and 19.

[77] Havermeyer, F., L. Ho, and C. Moser: 2011, 'Compact single mode tunable laser using a digital micromirror device'. *Opt. Express* **19**(15), 14642–14652. Cited on page 39.

[78] He, H., M. Friese, N. Heckenberg, and H. Rubinsztein-Dunlop: 1995, 'Direct Observation of Transfer of Angular Momentum to Absorptive Particles from a Laser Beam with a Phase Singularity'. *Phys. Rev. Lett.* **75**(5), 826–829. Cited on pages 63, 74, and 129.

[79] Heinze, G., C. Hubrich, and T. Halfmann: 2013, 'Stopped Light and Image Storage by Electromagnetically Induced Transparency up to the Regime of One Minute'. *Phys. Rev. Lett.* **111**, 033601. Cited on pages 21 and 67.

[80] Hemmer, P. R., D. P. Katz, J. Donoghue, M. Cronin-Golomb, M. S. Shahriar, and P. Kumar: 1995, 'Efficient low-intensity optical phase conjugation based on coherent population trapping in sodium'. *Opt. Lett.* **20**(9), 982–984. Cited on page 76.

[81] Horodecki, R., M. Horodecki, and K. Horodecki: 2009, 'Quantum entanglement'. *Rev. Mod. Phys.* **81**(2), 865–942. Cited on page 108.

[82] Indebetouw, G.: 1993, 'Optical Vortices and Their Propagation'. *J. Mod. Opt.* **40**(1), 73–87. Cited on pages 63, 64, and 70.

[83] Ivanov, S. and N. Vitanov: 2008, 'Steering quantum transitions between three crossing energy levels'. *Phys. Rev. A* **77**(2), 023406. Cited on page 95.

[84] Javan, A., O. Kocharovskaya, H. Lee, and M. O. Scully: 2002, 'Narrowing of electromagnetically induced transparency resonance in a Doppler-broadened medium'. *Phys. Rev. A* **66**, 013805. Cited on page 23.

[85] Julsgaard, B., A. Kozhekin, and E. S. Polzik: 2001, 'Experimental long-lived entanglement of two macroscopic objects.'. *Nature* **413**(6854), 400–403. Cited on page 25.

[86] Kash, M., V. Sautenkov, a. Zibrov, L. Hollberg, G. Welch, M. D. Lukin, Y. Rostovtsev, E. Fry, and M. Scully: 1999, 'Ultraslow Group Velocity and Enhanced Nonlinear Optical Effects in a Coherently Driven Hot Atomic Gas'. *Phys. Rev. Lett.* **82**(26), 5229–5232. Cited on page 3.

[87] Kelly, J. F. and A. Gallagher: 1987, 'Efficient electro-optic modulator for optical pumping of Na beams'. *Rev. Sci. Inst.* **58**(4), 563–566. Cited on page 46.

[88] Kenmoe, M. and S. Kenfack: 2013, 'Landau-Zener transitions between two and three decaying levels'. *arXiv:1307.3878* pp. 1–9. Cited on page 95.

[89] Kiffner, M. and T. N. Dey: 2009, 'Dynamical control of pulse propagation in electromagnetically induced transparency'. *Phys. Rev. A* **79**, 023829. Cited on pages 95, 96, and 98.

[90] Kim, K., M. Kwon, H. D. Park, H. S. Moon, H. S. Rawat, K. An, and J. B. Kim: 2001, 'Electromagnetically induced absorption spectra depending on intensities and detunings of the coupling field in Cs vapour'. *J Phys. B At. Mol. Opt. Phys.* **34**(23), 4801. Cited on pages 136 and 140.

[91] Klein, M., M. Hohensee, D. Phillips, and R. Walsworth: 2011, 'Electromagnetically induced transparency in paraffin-coated vapor cells'. *Phys. Rev. A* **83**(1), 013826. Cited on page 2.

[92] Kogelnik, H.: 1969, 'Coupled Wave Theory for Thick Hologram Gratings'. *Bell Syst. Tech. J.* **48**, 2909. Cited on pages 80 and 87.

[93] Korneev, N. and O. Benavides: 2008, 'Mechanisms of holographic recording in rubidium vapor close to resonance'. *J. Opt. Soc. Am. B* **25**(11), 1899–1906. Cited on pages 2 and 76.

[94] Korneev, N. and J. Soto: 2005, 'The nonlinear Faraday rotation-based dynamic holography in rubidium vapor'. *Opt. Commun.* **245**, 437 – 442. Cited on pages 2 and 77.

[95] Kuhn, A., M. Hennrich, and G. Rempe: 2002, 'Deterministic Single-Photon Source for Distributed Quantum Networking'. *Phys. Rev. Lett.* **89**(6), 067901. Cited on page 108.

[96] Kumar, S., T. Laupretre, R. Ghosh, F. Bretenaker, and F. Goldfarb: 2011, 'Interacting double dark resonances in a hot atomic vapor of helium'. *Phys. Rev. A* **84**, 023811. Cited on page 133.

[97] Kwiat, P. G., K. Mattle, H. Weinfurter, A. Zeilinger, A. Sergienko, and Y. Shih: 1995, 'New High-Intensity Source of Polarization-Entangled Photon Pairs'. *Phys. Rev. Lett.* **75**(24), 4337–4341. Cited on page 108.

[98] Kwiat, P. G., A. M. Steinberg, and R. Y. Chiao: 1993, 'High-visibility interference in a Bell-inequality experiment for energy and time'. *Phys. Rev. A* **47**(4), 2472–2475. Cited on page 108.

[99] Laurat, J., K. S. Choi, H. Deng, C. W. Chou, and H. J. Kimble: 2007, 'Heralded Entanglement between Atomic Ensembles: Preparation, Decoherence, and Scaling'. *Phys. Rev. Lett.* **99**, 180504. Cited on pages 4 and 31.

[100] Lee, H., M. Fleischhauer, and M. O. Scully: 1998, 'Sensitive detection of magnetic fields including their orientation with a magnetometer based on atomic phase coherence'. *Phys. Rev. A* **58**, 2587–2595. Cited on page 2.

[101] Lenci, L., S. Barreiro, P. Valente, H. Failache, and a. Lezama: 2012, 'A magnetometer suitable for measurement of the Earth's field based on transient atomic response'. *J. Phys. B At. Mol. Opt. Phys.* **45**(21), 215401. Cited on pages 3 and 95.

[102] Lerner, V., D. Shwa, Y. Drori, and N. Katz: 2012, 'Shaping Laguerre-Gaussian laser modes with binary gratings using a digital micromirror device'. *Opt. Lett.* **37**(23), 4826–4828. Cited on page 39.

[103] Lezama, A., S. Barreiro, and A. M. Akulshin: 1999, 'Electromagnetically induced absorption'. *Phys. Rev. A* **59**, 4732–4735. Cited on page 134.

[104] Li, Y.-Q. and M. Xiao: 1995a, 'Electromagnetically induced transparency in a three-level Λ-type system in rubidium atoms'. *Phys. Rev. A* **51**, 2703–2706. Cited on page 133.

[105] Li, Y. Q. and M. Xiao: 1995b, 'Transient properties of an electromagnetically induced transparency in three-level atoms.'. *Opt. Lett.* **20**(13), 1489–91. Cited on page 94.

[106] Lin, J. and N. A. Sinitsyn: 2014, 'Exact transition probabilities in the three-state Landau-Zener-Coulomb model'. *J. Phys. A Math. Theor.* **47**(1), 015301. Cited on page 95.

[107] Ling, H. Y., Y.-Q. Li, and M. Xiao: 1998, 'Electromagnetically induced grating: Homogeneously broadened medium'. *Phys. Rev. A* **57**, 1338–1344. Cited on pages 2, 76, and 77.

[108] Lipsich, A., S. Barreiro, A. M. Akulshin, and A. Lezama: 2000, 'Absorption spectra of driven degenerate two-level atomic systems'. *Phys. Rev. A* **61**, 053803. Cited on pages 134 and 140.

[109] Little, B., D. J. Starling, J. C. Howell, R. D. Cohen, D. Shwa, and N. Katz: 2013, 'Rapidly reconfigurable optically induced photonic crystals in hot rubidium vapor'. *Phys. Rev. A* **87**, 043815. Cited on pages 5, 77, 92, and 129.

[110] Lohmann, A. W. and D. P. Paris: 1967, 'Binary Fraunhofer Holograms, Generated by Computer'. *Appl. Opt.* **6**(10), 1739–1748. Cited on page 40.

[111] Lukin, M. D., M. Fleischhauer, a. Zibrov, H. Robinson, V. Velichansky, L. Hollberg, and M. Scully: 1997, 'Spectroscopy in Dense Coherent Media: Line Narrowing and Interference Effects'. *Phys. Rev. Lett.* **79**(16), 2959–2962. Cited on page 94.

[112] Lütkenhaus, N., J. Calsamiglia, and K.-A. Suominen: 1999, 'Bell measurements for teleportation'. *Phys. Rev. A* **59**, 3295–3300. Cited on page 27.

[113] Macalpine, W. and R. Schildknecht: 1959, 'Coaxial Resonators with Helical Inner Conductor'. *Proc. IRE* **47**(12), 2099 –2105. Cited on page 136.

[114] MacRae, A., T. Brannan, R. Achal, and A. I. Lvovsky: 2012, 'Tomography of a High-Purity Narrowband Photon from a Transient Atomic Collective Excitation'. *Phys. Rev. Lett.* **109**(3), 033601. Cited on page 109.

[115] Mair, A., A. Vaziri, G. Weihs, and A. Zeilinger: 2001, 'Entanglement of the orbital angular momentum states of photons.'. *Nature* **412**(6844), 313–6. Cited on page 63.

[116] Marangos, J. and T. Halfmann: 2010, 'Handbook of Optics, Third Edition Volume IV Optical Properties of Materials, Nonlinear Optics, Quantum Optics'. In: M. Bass (ed.): *Handb. Opt.*, No. Cm. New York, NY, USA: McGraw-Hill, third edition, Chapt. 14. Cited on pages 15 and 16.

[117] Margalit, L., M. Rosenbluh, and A. D. Wilson-Gordon: 2012, 'Coherence-population-trapping transients induced by an ac magnetic field'. *Phys. Rev. A* **85**(6), 063809. Cited on page 94.

[118] Matsukevich, D. N. and A. Kuzmich: 2004, 'Quantum State Transfer Between Matter and Light'. *Science* **306**(5696), 663–666. Cited on pages 4 and 31.

[119] Matsumoto, N., T. Ando, T. Inoue, Y. Ohtake, N. Fukuchi, and T. Hara: 2008, 'Generation of high-quality higher-order Laguerre-Gaussian beams using liquid-crystal-on-silicon spatial light modulators.'. *J. Opt. Soc. Am. A. Opt. Image Sci. Vis.* **25**(7), 1642–51. Cited on pages 42 and 43.

[120] Megidish, E., A. Halevy, T. Shacham, T. Dvir, L. Dovrat, and H. S. Eisenberg: 2013, 'Entanglement Swapping between Photons that have Never Coexisted'. *Phys. Rev. Lett.* **110**(21), 210403. Cited on page 28.

[121] Meinert, F., C. Basler, a. Lambrecht, S. Welte, and H. Helm: 2012, 'Quantitative analysis of the transient response of the refractive index to conditions of electromagnetically induced transparency'. *Phys. Rev. A* **85**(1), 013820. Cited on pages 94 and 99.

[122] Mikhailov, E. E., I. Novikova, M. D. Havey, and F. A. Narducci: 2009, 'Magnetic field imaging with atomic Rb vapor'. *Opt. Lett.* **34**(22), 3529. Cited on page 75.

[123] Mitsunaga, M. and N. Imoto: 1999, 'Observation of an electromagnetically induced grating in cold sodium atoms'. *Phys. Rev. A* **59**, 4773–4776. Cited on pages 2, 77, and 133.

[124] Moseley, R. R., S. Shepherd, D. J. Fulton, B. D. Sinclair, and M. H. Dunn: 1995, 'Spatial Consequences of Electromagnetically Induced Transparency: Observation of Electromagnetically Induced Focusing'. *Phys. Rev. Lett.* **74**, 670–673. Cited on pages 2 and 133.

[125] Mullen, K., E. Ben-Jacob, Y. Gefen, and Z. Schuss: 1989, 'Time of Zener tunneling'. *Phys. Rev. Lett.* **62**(21), 2543–2546. Cited on page 107.

[126] Neshev, D.: 1998, 'Motion control of ensembles of ordered optical vortices generated on finite extent background'. *Opt. Commun.* **151**(4-6), 413–421. Cited on pages 63, 64, and 66.

[127] Nielsen, A. E. B. and K. Mölmer: 2010, 'Deterministic multimode photonic device for quantum-information processing'. *Phys. Rev. A* **81**(4), 043822. Cited on page 109.

[128] Nielsen, M. A. and I. L. Chuang: 2004, *Quantum Computation and Quantum Information (Cambridge Series on Information and the Natural Sciences)*. Cambridge University Press. Cited on pages 26 and 28.

[129] Novikova, I., R. Walsworth, and Y. Xiao: 2012, 'Electromagnetically induced transparency-based slow and stored light in warm atoms'. *Laser Photonics Rev.* **6**(3), 333–353. Cited on pages 2 and 21.

[130] Novikova, I., Y. Xiao, D. F. Phillips, and R. L. Walsworth: 2005, 'EIT and diffusion of atomic coherence'. *J. Mod. Opt.* **52**(16), 2381–2390. Cited on page 22.

[131] Olivero, J. and R. Longbothum: 1977, 'Empirical fits to the Voigt line width: A brief review'. *J Quant. Spectrosc. Ra.* **17**(2), 233 – 236. Cited on page 52.

[132] Olson, A. J. and S. K. Mayer: 2009, 'Electromagnetically induced transparency in rubidium'. *Am. J Phys.* **77**(2), 116–121. Cited on page 133.

[133] Padgett, M. and L. Allen: 1995, 'The Poynting vector in Laguerre-Gaussian laser modes'. *Opt. Commun.* **121**, 36 – 40. Cited on page 65.

[134] Pampaloni, F. and J. Enderlein: 2004, 'Gaussian, Hermite-Gaussian, and Laguerre-Gaussian beams: A primer'. *arXiv:physics/0410021* p. 29. Cited on page 36.

[135] Pan, J.-W., Z.-B. Chen, C.-Y. Lu, H. Weinfurter, A. Zeilinger, and M. Zukowski: 2012, 'Multiphoton entanglement and interferometry'. *Rev. Mod. Phys.* **84**(2), 777–838. Cited on pages 26 and 108.

[136] Park, S., H. Cho, T. Kwon, and H. Lee: 2004, 'Transient coherence oscillation induced by a detuned Raman field in a rubidium Λ system'. *Phys. Rev. A* **69**(2), 023806. Cited on pages 94 and 98.

[137] Pearman, C. P., C. S. Adams, S. G. Cox, P. F. Griffin, D. A. Smith, and I. G. Hughes: 2002, 'Polarization spectroscopy of a closed atomic transition: applications to laser frequency locking'. *J. Phys. B At. Mol. Opt. Phys.* **35**(24), 5141–5151. Cited on page 54.

[138] Petrovic, J., I. Herrera, P. Lombardi, F. Schafer, and F. S. Cataliotti: 2013, 'A multi-state interferometer on an atom chip'. *N. J Phys.* **15**(4), 043002. Cited on page 103.

[139] Phillips, D. F., A. Fleischhauer, A. Mair, R. L. Walsworth, and M. D. Lukin: 2001, 'Storage of Light in Atomic Vapor'. *Phys. Rev. Lett.* **86**(5), 783–786. Cited on pages 20 and 21.

[140] Porras, D. and J. Cirac: 2008, 'Collective generation of quantum states of light by entangled atoms'. *Phys. Rev. A* **78**(5), 053816. Cited on page 109.

[141] Pugatch, R., M. Shuker, O. Firstenberg, A. Ron, and N. Davidson: 2007, 'Topological Stability of Stored Optical Vortices'. *Phys. Rev. Lett.* **98**, 203601. Cited on pages 63, 66, and 74.

[142] Ren, Y.-X., M. Li, K. Huang, J.-G. Wu, H.-F. Gao, Z.-Q. Wang, and Y.-M. Li: 2010, 'Experimental generation of Laguerre-Gaussian beam using digital micromirror device'. *Appl. Opt.* **49**(10), 1838–1844. Cited on page 40.

[143] Ricci, L., M. Weidemüller, T. Esslinger, A. Hemmerich, C. Zimmermann, V. Vuletic, W. König, and T. Hänsch: 1995, 'A compact grating-stabilized diode laser system for atomic physics'. *Opt. Comm.* **117**, 541 – 549. Cited on page 34.

[144] Rozas, D., C. T. Law, and G. A. Swartzlander: 1997a, 'Propagation dynamics of optical vortices'. *J. Opt. Soc. Am. B* **14**(11), 3054. Cited on pages 64, 66, and 74.

[145] Rozas, D., Z. S. Sacks, and G. a. Swartzlander, Jr.: 1997b, 'Experimental Observation of Fluidlike Motion of Optical Vortices'. *Phys. Rev. Lett.* **79**(18), 3399–3402. Cited on pages 64, 65, 66, and 70.

[146] Saleh, B. and M. Teich: 2007, *Fundamentals of Photonics*, Wiley Series in Pure and Applied Optics. Wiley. Cited on pages 2, 10, 44, 45, 48, 49, 52, and 87.

[147] Saloman, E. B. and C. J. Sansonetti: 2004, 'Wavelengths, Energy Level Classifications, and Energy Levels for the Spectrum of Neutral Neon'. *J Phys. Chem. Ref. Data* **33**(4), 1113–1158. Cited on page 134.

[148] Sangouard, N., C. Simon, H. de Riedmatten, and N. Gisin: 2011, 'Quantum repeaters based on atomic ensembles and linear optics'. *Rev. Mod. Phys.* **83**(1), 33–80. Cited on pages 4, 28, 31, 108, 109, 112, 116, and 123.

[149] Sapiens, N., A. Weissbrod, and A. J. Agranat: 2009, 'Fast electroholographic switching'. *Opt. Lett.* **34**(3), 353–355. Cited on page 76.

[150] Schnorrberger, U., J. D. Thompson, S. Trotzky, R. Pugatch, N. Davidson, S. Kuhr, and I. Bloch: 2009, 'Electromagnetically Induced Transparency and Light Storage in an Atomic Mott Insulator'. *Phys. Rev. Lett.* **103**, 033003. Cited on page 21.

[151] Shakhmuratov, R. and J. Odeurs: 2005, 'Pulse transformation and time-frequency filtering with electromagnetically induced transparency'. *Phys. Rev. A* **71**(1), 013819. Cited on page 94.

[152] Sherson, J. F., B. Julsgaard, and E. S. Polzik: 2007, 'Deterministic atom-light quantum interface'. *Adv. At. Mol. Opt. Phys.* **54**, 82. Cited on page 25.

[153] Shevchenko, S., S. Ashhab, and F. Nori: 2010, 'Landau-Zener-Stückelberg interferometry'. *Phys. Rep.* **492**(1), 1–30. Cited on page 100.

[154] Shiozaki, R. F., E. a. L. Henn, K. M. F. Magalhães, T. Amthor, and V. S. Bagnato: 2007, 'Tunable eletro-optical modulators based on a split-ring resonator.'. *Rev. Sci. Instrum.* **78**(1), 016103. Cited on page 46.

[155] Shore, B. W.: 2008, 'Coherent manipulations of atoms using laser light'. *Acta Phys. Slovaca* **58**(3), 243 – 486. Cited on pages 7, 10, 12, and 14.

[156] Shuker, M.: 2008, 'Decay Processes in EIT Medium'. Ph.D. thesis, Technion, Israel Institute of Technology, Haifa. Cited on pages 52 and 60.

[157] Shuker, M., O. Firstenberg, R. Pugatch, A. Ben-Kish, A. Ron, and N. Davidson: 2007, 'Angular dependence of Dicke-narrowed electromagnetically induced transparency resonances'. *Phys. Rev. A* **76**, 023813. Cited on page 23.

[158] Shuker, M., O. Firstenberg, R. Pugatch, A. Ron, and N. Davidson: 2008, 'Storing Images in Warm Atomic Vapor'. *Phys. Rev. Lett.* **100**, 223601. Cited on pages 21, 66, and 74.

[159] Shwa, D., R. D. Cohen, A. Retzker, and N. Katz: 2013, 'Heralded generation of Bell states using atomic ensembles'. *Phys. Rev. A* **88**, 063844. Cited on page 5.

[160] Shwa, D., E. Shtranvasser, Y. Shalibo, and N. Katz: 2012, 'Controllable motion of optical vortex arrays using electromagnetically induced transparency'. *Opt. Express* **20**(22), 24835–24842. Cited on page 5.

[161] Srivathsan, B., G. K. Gulati, B. Chng, G. Maslennikov, D. Matsukevich, and C. Kurtsiefer: 2013, 'Narrow Band Source of Transform-Limited Photon Pairs via Four-Wave Mixing in a Cold Atomic Ensemble'. *Phys. Rev. Lett.* **111**, 123602. Cited on page 109.

[162] Starling, D. J., S. M. Bloch, P. K. Vudyasetu, J. S. Choi, B. Little, and J. C. Howell: 2012, 'Double Lorentzian atomic prism'. *Phys. Rev. A* **86**, 023826. Cited on page 77.

[163] Steck, D. A., *Quantum and Atom Optics*. available online at http://steck.us/teaching (revision 0.8.3, 25 May 2012). Cited on pages 2, 7, 9, 14, and 104.

[164] Steck, D. A., 'Rubidium 85 D Line Data'. available online at http://steck.us/alkalidata (revision 2.1.6, 20 September 2013). Cited on pages 51 and 89.

[165] Steck, D. A., 'Rubidium 87 D Line Data'. available online at http://steck.us/alkalidata (revision 2.1.4, 23 December 2010). Cited on pages 51, 56, and 60.

[166] Stevenson, R. M., R. J. Young, P. Atkinson, K. Cooper, D. a. Ritchie, and a. J. Shields: 2006, 'A semiconductor source of triggered entangled photon pairs.'. *Nature* **439**(7073), 179–82. Cited on page 109.

[167] Taichenachev, A., V. Yudin, R. Wynands, M. Stähler, J. Kitching, and L. Hollberg: 2003, 'Theory of dark resonances for alkali-metal vapors in a buffer-gas cell'. *Phys. Rev. A* **67**(3), 033810. Cited on pages 101 and 105.

[168] Thomas, J. and W. Quivers: 1980, 'Transit-time effects in optically pumped coupled three-level systems'. *Phys. Rev. A* **22**(5), 2115–2121. Cited on page 22.

[169] Thomas, J. E. and R. A. Forber: 1984, 'Transverse atomic motion in transient polarization phenomena'. *Opt. Lett.* **9**(2), 56–58. Cited on page 137.

[170] Tidström, J., P. Jänes, and L. M. Andersson: 2007, 'Delay-bandwidth product of electromagnetically induced transparency media'. *Phys. Rev. A* **75**, 053803. Cited on pages 19 and 94.

[171] Tittel, W., M. Afzelius, T. Chanelière, R. Cone, S. Kröll, S. Moiseev, and M. Sellars: 2009, 'Photon-echo quantum memory in solid state systems'. *Laser Photon. Rev.* **4**(2), 244–267. Cited on page 21.

[172] Truscott, A. G., M. E. J. Friese, N. R. Heckenberg, and H. Rubinsztein-Dunlop: 1999, 'Optically Written Waveguide in an Atomic Vapor'. *Phys. Rev. Lett.* **82**, 1438–1441. Cited on pages 2 and 76.

[173] Tucker, R. S. and P. C. Ku: 2005, 'Delay-bandwidth product and storage density in slow-light optical buffers'. *Electron. Lett.* **41**(4), 11–12. Cited on page 19.

[174] van der Wal, C. H., M. D. Eisaman, A. André, R. L. Walsworth, D. F. Phillips, A. S. Zibrov, and M. D. Lukin: 2003, 'Atomic Memory for Correlated Photon States'. *Science* **301**(5630), 196–200. Cited on pages 4, 108, and 120.

[175] Vanier, J.: 2005, 'Atomic clocks based on coherent population trapping: a review'. *App. Phys. B* **81**(4), 421–442. Cited on pages 2 and 15.

[176] Vassen, W., C. Cohen-Tannoudji, M. Leduc, D. Boiron, C. I. Westbrook, A. Truscott, K. Baldwin, G. Birkl, P. Cancio, and M. Trippenbach: 2012, 'Cold and trapped metastable noble gases'. *Rev. Mod. Phys.* **84**, 175–210. Cited on page 134.

[177] Vitanov, N.: 1999, 'Transition times in the Landau-Zener model'. *Phys. Rev. A* **59**(2), 988–994. Cited on pages 105, 106, and 107.

[178] Vitanov, N. V. and S. Stenholm: 1997, 'Analytic properties and effective two-level problems in stimulated Raman adiabatic passage'. *Phys. Rev. A* **55**(1), 648–660. Cited on page 101.

[179] Vladimirova, Y. V., V. N. Zadkov, a. V. Akimov, a. Y. Samokotin, a. V. Sokolov, V. N. Sorokin, and N. N. Kolachevsky: 2009, 'Frequency-modulation spectroscopy of coherent dark resonances in 87Rb atoms'. *Appl. Phys. B* **97**(1), 35–46. Cited on pages 3 and 94.

[180] Vudyasetu, P. K., R. M. Camacho, and J. C. Howell: 2008, 'Storage and Retrieval of Multimode Transverse Images in Hot Atomic Rubidium Vapor'. *Phys. Rev. Lett.* **100**, 123903. Cited on pages 21, 66, and 74.

[181] Vudyasetu, P. K., D. J. Starling, and J. C. Howell: 2009, 'All Optical Waveguiding in a Coherent Atomic Rubidium Vapor'. *Phys. Rev. Lett.* **102**, 123602. Cited on pages 2, 63, 76, and 77.

[182] Vurgaftman, I. and M. Bashkansky: 2013, 'Suppressing four-wave mixing in warm-atomic-vapor quantum memory'. *Phys. Rev. A* **87**(6), 063836. Cited on page 110.

[183] Walther, P., M. D. Eisaman, A. André, F. Massou, M. Fleischhauer, A. S. Zibrov, and M. D. Lukin: 2007, 'generation of narrow-bandwidth single photons using electromagnetically induced transparency in atomic ensembles'. *Int. J. Quantum Inf.* **5**, 51–62. Cited on page 109.

[184] Wootters, W. K. and W. H. Zurek: 1982, 'A single quantum cannot be cloned'. *Nature* **299**, 802. Cited on pages 4, 26, and 28.

[185] Wu, Y.: 1996, 'Effective Raman theory for a three-level atom in the Lambda configuration.'. *Phys. Rev. A* **54**(2), 1586–1592. Cited on page 101.

[186] Xiao, Y.: 2009, 'Spectral line narrowing in electromagnetically induced transparency'. *Mod. Phys. Lett. B* **23**(5), 661. Cited on page 24.

[187] Xiao, Y., I. Novikova, D. F. Phillips, and R. L. Walsworth: 2006, 'Diffusion-Induced Ramsey Narrowing'. *Phys. Rev. Lett.* **96**, 043601. Cited on pages 24 and 58.

[188] Yao, A. M. and M. J. Padgett: 2011, 'Orbital angular momentum: origins, behavior and applications'. *Adv. Opt. Photonics* **3**(2), 161. Cited on pages 38 and 129.

[189] Yariv, A. and P. Yeh: 2007, *Photonics: Optical Electronics in Modern Communications*, The Oxford Series in Electrical and Computer Engineering. Oxford University Press, Incorporated. Cited on pages 1, 45, 46, and 76.

[190] Yavuz, D. D.: 2007, 'Electromagnetically induced transparency with broadband laser pulses'. *Phys. Rev. A* **75**, 031801. Cited on pages 3 and 94.

[191] Ye, C. Y. and A. S. Zibrov: 2002, 'Width of the electromagnetically induced transparency resonance in atomic vapor'. *Phys. Rev. A* **65**, 023806. Cited on page 23.

[192] Yelin, S. F., V. A. Sautenkov, M. M. Kash, G. R. Welch, and M. D. Lukin: 2003, 'Nonlinear optics via double dark resonances'. *Phys. Rev. A* **68**, 063801. Cited on page 133.

[193] Yudin, V. I., A. V. Taichenachev, Y. O. Dudin, V. L. Velichansky, A. S. Zibrov, and S. A. Zibrov: 2010, 'Vector magnetometry based on electromagnetically induced transparency in linearly polarized light'. *Phys. Rev. A* **82**(3), 033807. Cited on pages 2, 60, and 101.

[194] Zhao, B., Y.-A. Chen, X.-H. Bao, T. Strassel, C.-S. Chuu, X.-M. Jin, J. Schmiedmayer, Z.-S. Yuan, S. Chen, and J.-W. Pan: 2008a, 'A millisecond quantum memory for scalable quantum networks'. *Nat. Phys.* **5**(2), 95–99. Cited on pages 4, 31, 108, and 116.

[195] Zhao, L., T. Wang, Y. Xiao, and S. Yelin: 2008b, 'Image storage in hot vapors'. *Phys. Rev. A* **77**(4), 1–4. Cited on page 66.

[196] Zhao, R., Y. O. Dudin, S. D. Jenkins, C. J. Campbell, D. N. Matsukevich, T. a. B. Kennedy, and a. Kuzmich: 2008c, 'Long-lived quantum memory'. *Nat. Phys.* **5**(2), 100–104. Cited on page 108.

[197] Zhu, Y. and T. N. Wasserlauf: 1996, 'Sub-Doppler linewidth with electromagnetically induced transparency in rubidium atoms'. *Phys. Rev. A* **54**, 3653–3656. Cited on page 133.

[198] Zibrov, S. A., I. Novikova, D. F. Phillips, R. L. Walsworth, A. S. Zibrov, V. L. Velichansky, A. V. Taichenachev, and V. I. Yudin: 2010, 'Coherent-population-trapping resonances with linearly polarized light for all-optical miniature atomic clocks'. *Phys. Rev. A* **81**(1), 013833. Cited on pages 60 and 101.

[199] Zinner, M., P. Spoden, T. Kraemer, G. Birkl, and W. Ertmer: 2003, 'Precision measurement of the metastable $^3P_2$ lifetime of neon'. *Phys. Rev. A* **67**, 010501. Cited on page 135.

[200] Zorabedian, P.: 1995, *Tunable Lasers*, Chapt. Tunable external-cavity semiconductor lasers, p. 349. Academic Press, London. Cited on page 33.

[201] Zukowski, M., A. Zeilinger, M. A. Horne, and A. K. Ekert: 1993, '"Event-ready-detectors" Bell experiment via entanglement swapping'. *Phys. Rev. Lett.* **71**, 4287–4290. Cited on page 27.